IMPACTS OF NEGLECTING LONGWAVE SCATTERING AND THE METHODS OF REDUCING THESE UNCERTAINTIES IN MODEL SIMULATIONS CONTAINING CLOUDS

A Dissertation

by

CHIA-PANG KUO

Submitted to the Office of Graduate and Professional Studies
of Texas A&M University
in partial fulfillment of the requirements for the degree of

DOCTOR OF PHILOSOPHY

Chair of Committee,	Ping Yang
Committee Members,	Andrew Klein
	Anita Rapp
	Kenneth P. Bowman
Head of Department,	Ping Yang

August 2018

Major Subject: Atmospheric Sciences

ABSTRACT

Since clouds are spread widely around the world and heavily influence the Earth's energy budget, people extensively use general circulation models (GCMs) to investigate the effect of clouds on the future climate. Since in the longwave spectrum, absorption leads the radiative transfer processes, to reduce computing time, radiative schemes in most GCMs only take absorption properties of clouds into account.

This study investigates the issues of neglecting longwave scattering induced by clouds using satellite observations in 2010. Global simulations show that excluding longwave scattering overestimates upward flux at the top-of-atmosphere (TOA) by about 2.63 W/m^2, which is about 10% of the TOA longwave (LW) cloud radiative effect, and underestimates downward flux at the surface by about 1.15 W/m^2, corresponding to about 5% of the surface LW cloud radiative effect. Longwave scattering cools the atmosphere by about 0.018 K/day at the tropopause and heats about 0.028 K/day at the surface. The magnitude of the cloud radiative effect from neglecting longwave scattering is similar to the clear-sky radiative effect of doubling CO_2. Spectral analysis shows that longwave scattering by ice clouds contributes over 40% of simulation biases in the 350-500 cm^{-1} band.

For simpler calculations, the optical properties of ice clouds used in the Moderate Resolution Imaging Spectrometer (MODIS) Collection 6 cloud retrieval products are appropriately parameterized as a function of effective particle size. The overall coefficients of determination (R^2) of the corresponding fitting processes are larger than

0.9. By using these parameterized highly scattered ice cloud optical properties in an isothermal homogeneous cloud layer, the performance of various radiative transfer models is examined. The results show that 2-/4-stream approximations are relatively more efficient and are relatively more accurate than other approximation methods in comparisons of simulated cloud emissivity.

ACKNOWLEDGEMENTS

I would like to thank my committee chair, Professor Ping Yang, and my committee members, Professor Klein, Professor Rapp, and Professor Bowman, for their guidance and support throughout the course of this research.

Thanks also go to my friends and colleagues and the department faculty and staff for making my time at Texas A&M University a great experience. In addition, I would like to thank all group members for their assistance. Especially for Dr. Bingqi Yi, Dr. Guanglang Xu and Dr. Souichiro Hioki, I appreciate their insightful suggestion and discussion when I faced difficulties in my research.

In addition, special thanks to my mother and father for their encouragement and to my girl friend Wei-Ching for her accompany, support and love.

CONTRIBUTORS AND FUNDING SOURCES

This work was supported by a dissertation committee consisting of Professor Ping Yang, Professor Anita Rapp and Professor Kenneth P. Bowman of the Department of Atmospheric Sciences and Professor Andrew Klein of the Department of Geography.

Furthermore, this work was supported by the U.S. Department of Energy (Grant DE-SC0013080), the National Science Foundation (AGS-1632209), and the endowment funds related to the David Bullock Harris Chair in Geosciences at the College of Geosciences, Texas A&M University. The computational resources in simulations were provided by the Texas A&M Supercomputing Facility (http://sc.tamu.edu).

TABLE OF CONTENTS

Page

LIST OF FIGURES

Page

LIST OF TABLES

Page

1. INTRODUCTION

1.1 Radiative effect of clouds

Clouds act as an important modulator, adjusting global energy distribution and interacting with circulation through phase changes, radiative transfer and turbulent transport of air parcels (Bony et al., 2015). In this study, we focus on the radiative effects of clouds (Liou, 2002), which absorb longwave radiation (heating effect) and reflect shortwave radiation (cooling effect). Since clouds cover about 70% of Earth's surface (Stubenrauch et al., 2013) and have different microphysical and optical properties, considering net radiative effects (longwave and shortave), clouds may cause heating or cooling (Allan, 2011) of the atmosphere depending on the cloud type and location. For example, by using the Earth's Radiant Energy System (CERES) observations, clouds reflect more shortwave than longwave radiation at the top of the atmosphere (TOA) in some regions, such as the midlatitude storm-track area and the ocean stratocumulus area (off the coast of Peru, California and Namibia), and the cooling and heating effects of clouds are almost equal at the TOA in the West Pacific and Indian ocean. Overall, global net cloud radiative effects are negative, leading to cooling the TOA (Allan, 2011; Ramanathan et al., 1989).

Given detailed information of cloud properties, like cloud optical thickness (τ) and cloud top pressure (CTP), radiative effects of clouds are classified into several groups. For example, by using the International Satellite Cloud Climatology Project dataset (ISCCP; Rossow & Schiffer 1991, 1999; Schiffer & Rossow 1983, 1985),

Hartmann et al. (1992) characterized clouds into high (CTP < 440 hPa), middle (CTP > 440 and < 680 hPa), low (CTP > 680 hPa), thin ($\tau < 9.38$), and thick ($\tau > 9.38$) clouds, and found that high and middle thin clouds have a positive net radiative effect, and thick and low clouds have negative net radiative effect. Additionally, these classifications can be used to investigate the cloudy conditions simulated in global circulation models (GCMs) (Jin et al., 2017).

The microphysical and radiative properties of clouds may affect the climate (Ritter & Geleyn, 1992; Yang et al., 2015). Stephens et al. (1990) show that a decrease in the asymmetry factor of ice particles reduces warming effects of ice clouds. Greenwald et al. (1995), using Earth Radiation Budget Satellite (ERBS) measurements, find that net forcing from low clouds decreases 25 W/m^2 with an increase of 0.05 kg/m^2 in liquid water path (LWP) when the LWP is less than 0.2 kg/m^2 and the solar zenith angle is 75°. Zhang et al. (1999) indicate that ice cloud particle habits significantly affect cloud radiative forcing in the solar band. Furthermore, for a given amount of ice water content (IWC), smaller ice crystals lead to a cooling effect, whereas larger ice particles give rise to a warming effect. Choi and Ho (2006) analyzed observations from the Moderate Resolution Imaging Spectroradiometer (MODIS) and CERES over the Tropics (25°S to 25°N) during 2000-2005, and mention that ice clouds tend to warm (cool) the climate with optical thickness of ice cloud less (more) than 10. Fu (2007) states that the change in aspect ratio of ice particles from 1.0 to 0.5 or to 0.1 reduces the reflected solar flux about 30 or 70 W/m^2, respectively, when the solar zenith angle is 60° and the optical thickness of the ice cloud is 4.

Incorrect cloud fields in GCMs may cause biases in future projections. For instance, overestimations of cloud cover in the Tropics cause sea surface temperature to be biased low in GCM simulations (Li & Xie, 2012). Mauritsen and Stevens (2015) pointed out that the climate sensitivity is lower in inferences from observations than in simulations by climate models, and mentioned a possible negative feedback, called the iris effect, that can be used to make simulations close to observations. The iris effect was first proposed by Lindzen et al. (2001), who hypothesized that in the Tropics cirrus clouds would decrease in a warmer climate to increase the outgoing longwave radiation (OLR). Although the existence of the iris effect is debated (Lin et al., 2002, 2004, 2006; Rapp et al., 2005; Su et al., 2008), Choi et al. (2017) observed a negative cirrus clouds feedback by analyzing Tropical Rainfall Measuring Mission (TRMM) and A-Train (Afternoon Train) data.

1.2 Radiative transfer schemes

In a large-scale simulation, accurate and fast radiative transfer models (RTMs) and appropriate optical properties of clouds are needed to correctly evaluate the radiative effect of clouds. Table 1.1 lists longwave RTMs used in various GCMs. Since absorption dominates over scattering in the longwave spectrum, to increase global simulation efficiency, most GCMs only consider absorption properties of clouds in the radiative schemes, except for CanCM4 (von Salzen et al., 2013), HadCM3 (Pope et al., 2000), and GISS ModelE and ModelE2 (Schmidt et al., 2006, 2014).

Among those schemes only considering absorption, the most frequently used RTM is the GCM version of the rapid radiative transfer model in the longwave

(RRTMG_LW; Clough et al., 2005; Iacono et al., 2008; Mlawer et al., 1997, 2016), which uses the k-distribution method to calculate absorption properties of gases and applies the 2-stream approximation that sets the diffusivity factor to 1.66 to calculate one upward and one downward flux. To make flux calculations more accurate, RRTMG_LW slightly adjusts the diffusivity factor as a function of total column water vapor in specific spectral bands. By comparing with the most accurate results from a line-by-line radiative transfer model (LBLRTM; Clough et al., 2005), under clear sky, flux errors are within 1 W/m2, and cooling rate errors are within 0.1 K/day in the troposphere and 0.3 K/day in the stratosphere (Mlawer et al., 1997, 2016). For the code and performance of RRTMG_LW, the website (http://rtweb.aer.com/rrtm_frame.html) contains more detailed information.

Although radiative transfer processes only consider absorption of clouds to approximate fluxes due to relative stronger absorption properties in the longwave spectrum, the following studies analyzed the importance of longwave scattering by clouds. Ritter and Geleyn (1992) report a 16.2 W/m^2 decrease in OLR because of considering scattering from a cloud between 12 and 13 km altitude with liquid water content of 0.01 g/m^2. Edwards and Slingo (1996) show the importance of scattering as a function of ice water path. Chou et al. (1999), Fu et al. (1997), O'Brien et al. (1997), and Tang et al. (2018) tested longwave cloud scattering in various RTMs and tried to parameterize cloud longwave scattering. Using GCMs, 8 W/m^2 reductions on the global mean OLR by considering longwave scattering was estimated by Stephens et al. (2001). Joseph and Min (2003), Costa and Shine (2006), and Schmidt et al. (2006) state that

neglecting LW scattering overestimates TOA upward flux by 1.5 to 8 W/m^2 depending on the examined regions and sources of cloud information.

Since longwave scattering is neglected in most GCMs listed in Table 1.1, but clouds significantly affect the global energy budget, the potential influence of excluding longwave scattering by clouds has to be investigated. Therefore, we first use high spatial resolution satellite measurements to analyze the influence of longwave scattering by clouds in Chapter 2, and then Chapter 3 will present the efficiency and accuracy of various RTMs and also propose a new parameterization scheme of ice cloud optical properties. Finally, conclusions and possible future work are summarized in Chapter 4.

Table 1.1 Longwave radiative transfer in the selected GCMs

Model	Longwave radiation scheme	Scattering
CanCM4 (von Salzen et al., 2013)	2-stream approximation (Li, 2002)	yes
CAM4 (Neale et al., 2010)	Absorptivity/emissivity approximation (Ramanathan & Downey, 1986)	no
CAM5 (Neale et al., 2012)	RRTMG_LW (2-stream approximation) (Clough et al., 2005; Iacono et al., 2008; Mlawer et al., 1997, 2016)	no
CFSR (Saha et al., 2010) CFSv2 (Saha et al., 2014)	RRTMG_LW (2-stream approximation) (Clough et al., 2005; Iacono et al., 2008; Mlawer et al., 1997, 2016)	no
ECHAM5 (Roeckner et al., 2003)	RRTMG_LW (2-stream approximation) (Clough et al., 2005; Iacono et al., 2008; Mlawer et al., 1997, 2016)	no
ECHAM6 (Stevens et al., 2013)	RRTMG_LW (2-stream approximation) (Clough et al., 2005; Iacono et al., 2008; Mlawer et al., 1997, 2016)	no
HadCM3 (Pope et al., 2000)	2-stream approximation (PIFM) (Cusack et al., 1999; Edwards & Slingo, 1996; Goody & Yung, 1989; Zdunkowski et al., 1982)	yes
LMDZ4 (Hourdin et al., 2006)	Absorptivity/emissivity approximation (Morcrette, J.-J., 1991)	no
LMDZ-B (Fita , 2013; Hourdin et al., 2013)	RRTMG_LW (2-stream approximation) (Clough et al., 2005; Iacono et al., 2008; Mlawer et al., 1997, 2016)	no
GFDL Global Atmosphere Model AM2 (Anderson et al., 2004) GFDL Global Atmosphere Model AM3 (Donner et al., 2011)	Absorptivity/emissivity approximation (Ramachandran et al., 2000; Schwarzkopf & Ramaswamy, 1999)	no
GISS ModelE (Schmidt et al., 2006) GISS ModelE2 (Schmidt et al., 2014)	Absorptivity/emissivity approximation with scattering effect correction (Hansen et al., 1983)	yes

References

Allan, R. P. (2011). Combining satellite data and models to estimate cloud radiative effect at the surface and in the atmosphere. *Meteorological Applications*, *18*(3), 324–333. https://doi.org/10.1002/met.285

Anderson, J. L., Balaji, V., Broccoli, A. J., Cooke, W. F., Delworth, T. L., Dixon, K. W., … Wyman, B. L. (2004). The new GFDL Global Atmosphere and Land Model AM2–LM2: Evaluation with prescribed SST simulations. *Journal of Climate*, *17*(24), 4641–4673. https://doi.org/10.1175/JCLI-3223.1

Bony, S., Stevens, B., Frierson, D. M. W., Jakob, C., Kageyama, M., Pincus, R., … Webb, M. J. (2015). Clouds, circulation and climate sensitivity. *Nature Geoscience*, *8*(4), 261–268. https://doi.org/10.1038/ngeo2398

Clough, S. A., Shephard, M. W., Mlawer, E. J., Delamere, J. S., Iacono, M. J., Cady-Pereira, K., … Brown, P. D. (2005). Atmospheric radiative transfer modeling: A summary of the AER codes. *Journal of Quantitative Spectroscopy and Radiative Transfer*, *91*(2), 233–244. https://doi.org/10.1016/j.jqsrt.2004.05.058

Choi, Y.-S., & Ho, C.-H. (2006). Radiative effect of cirrus with different optical properties over the tropics in MODIS and CERES observations. *Geophysical Research Letters*, *33*(21), L21811. https://doi.org/10.1029/2006GL027403

Choi, Y.-S., Kim, W., Yeh, S.-W., Masunaga, H., Kwon, M.-J., Jo, H.-S., & Huang, L. (2017). Revisiting the iris effect of tropical cirrus clouds with TRMM and A-Train satellite data. *Journal of Geophysical Research: Atmospheres*, *122*(11), 5917–5931. https://doi.org/10.1002/2016JD025827

Chou, M.-D., Lee, K.-T., Tsay, S.-C., & Fu, Q. (1999). Parameterization for cloud longwave scattering for use in atmospheric models. *Journal of Climate*, *12*(1), 159–169. https://doi.org/10.1175/1520-0442-12.1.159

Costa, S. M. S., & Shine, K. P. (2006). An estimate of the global impact of multiple scattering by clouds on outgoing long-wave radiation. *Quarterly Journal of the Royal Meteorological Society*, *132*(616), 885–895. https://doi.org/10.1256/qj.05.169

Cusack, S., Edwards, J. M., & Crowther, J. M. (1999). Investigating k distribution methods for parameterizing gaseous absorption in the Hadley Centre Climate Model. *Journal of Geophysical Research: Atmospheres*, *104*(D2), 2051–2057. https://doi.org/10.1029/1998JD200063

Donner, L. J., Wyman, B. L., Hemler, R. S., Horowitz, L. W., Ming, Y., Zhao, M., … Zeng, F. (2011). The dynamical ccore, physical parameterizations, and basic

simulation characteristics of the atmospheric component AM3 of the GFDL global coupled model CM3. *Journal of Climate*, *24*(13), 3484–3519. https://doi.org/10.1175/2011JCLI3955.1

Edwards, J. M., & Slingo, A. (1996). Studies with a flexible new radiation code. I: Choosing a configuration for a large-scale model. *Quarterly Journal of the Royal Meteorological Society*, *122*(531), 689–719. https://doi.org/10.1002/qj.49712253107

Fita, L. (2013). LMDZ physical schemes. A brief description for the LMDZ-B configuration. Retrieved from http://lmdz.lmd.jussieu.fr/developpeurs/notes-techniques/ressources/LMDZphys.pdf

Fu, Q., Liou, K. N., Cribb, M. C., Charlock, T. P., & Grossman, A. (1997). Multiple scattering parameterization in thermal infrared radiative transfer. *Journal of the Atmospheric Sciences*, *54*(24), 2799–2812. https://doi.org/10.1175/1520-0469(1997)054<2799:MSPITI>2.0.CO;2

Fu, Q. (2007). A new parameterization of an asymmetry factor of cirrus clouds for climate models. *Journal of the Atmospheric Sciences*, *64*(11), 4140–4150. https://doi.org/10.1175/2007JAS2289.1

Goody, R. M., & Yung, Y. L. (1989). *Atmospheric Radiation: Theoretical Basis* (2nd ed.). New York: Oxford University Press.

Greenwald, T. J., Stephens, G. L., Christopher, S. A., & Vonder Haar, T. H. (1995). Observations of the global characteristics and regional radiative effects of marine cloud liquid water. *Journal of Climate*, *8*(12), 2928–2946. https://doi.org/10.1175/1520-0442(1995)008<2928:OOTGCA>2.0.CO;2

Hansen, J., Russell, G., Rind, D., Stone, P., Lacis, A., Lebedeff, S., … Travis, L. (1983). Efficient three-dimensional global models for climate studies: Models I and II. *Monthly Weather Review*, *111*(4), 609–662. https://doi.org/10.1175/1520-0493(1983)111<0609:ETDGMF>2.0.CO;2

Hartmann, D. L., Ockert-Bell, M. E., & Michelsen, M. L. (1992). The effect of cloud type on Earth's energy balance: Global analysis. *Journal of Climate*, *5*(11), 1281–1304. https://doi.org/10.1175/1520-0442(1992)005<1281:TEOCTO>2.0.CO;2

Hourdin, F., Musat, I., Bony, S., Braconnot, P., Codron, F., Dufresne, J.-L., … Lott, F. (2006). The LMDZ4 general circulation model: Climate performance and sensitivity to parametrized physics with emphasis on tropical convection. *Climate Dynamics*, *27*(7–8), 787–813. https://doi.org/10.1007/s00382-006-0158-0

Hourdin, F., Foujols, M.-A., Codron, F., Guemas, V., Dufresne, J.-L., Bony, S., … Bopp, L. (2013). Impact of the LMDZ atmospheric grid configuration on the climate and sensitivity of the IPSL-CM5A coupled model. *Climate Dynamics*, *40*(9–10), 2167–2192. https://doi.org/10.1007/s00382-012-1411-3

Iacono, M. J., Delamere, J. S., Mlawer, E. J., Shephard, M. W., Clough, S. A., & Collins, W. D. (2008). Radiative forcing by long-lived greenhouse gases: Calculations with the AER radiative transfer models. *Journal of Geophysical Research*, *113*(13), D13103. https://doi.org/10.1029/2008JD009944

Jin, D., Oreopoulos, L., & Lee, D. (2017). Regime-based evaluation of cloudiness in CMIP5 models. *Climate Dynamics*, *48*(1–2), 89–112. https://doi.org/10.1007/s00382-016-3064-0

Joseph, E., & Min, Q. (2003). Assessment of multiple scattering and horizontal inhomogeneity in IR radiative transfer calculations of observed thin cirrus clouds. *Journal of Geophysical Research*, *108*(D13), 4380. https://doi.org/10.1029/2002JD002831

Li, G., & Xie, S.-P. (2012). Origins of tropical-wide SST biases in CMIP multi-model ensembles. *Geophysical Research Letters*, *39*(22), L22703. https://doi.org/10.1029/2012GL053777

Li, J. (2002). Accounting for unresolved clouds in a 1D infrared radiative transfer model. Part I: Solution for radiative transfer, including cloud scattering and overlap. *Journal of the Atmospheric Sciences*, *59*(23), 3302–3320. https://doi.org/10.1175/1520-0469(2002)059<3302:AFUCIA>2.0.CO;2

Lin, B., Wielicki, B. A., Chambers, L. H., Hu, Y., & Xu, K.-M. (2002). The iris hypothesis: A negative or positive cloud feedback? *Journal of Climate*, *15*(1), 3–7. https://doi.org/10.1175/1520-0442(2002)015<0003:TIHANO>2.0.CO;2

Lin, B., Wong, T., Wielicki, B. A., & Hu, Y. (2004). Examination of the decadal tropical mean ERBS nonscanner radiation data for the iris hypothesis. *Journal of Climate*, *17*(6), 1239–1246. https://doi.org/10.1175/1520-0442(2004)017<1239:EOTDTM>2.0.CO;2

Lin, B., Wielicki, B. A., Minnis, P., Chambers, L., Xu, K.-M., Hu, Y., & Fan, A. (2006). The Effect of environmental conditions on tropical deep convective systems observed from the TRMM satellite. *Journal of Climate*, *19*(22), 5745–5761. https://doi.org/10.1175/JCLI3940.1

Lindzen, R. S., Chou, M.-D., & Hou, A. Y. (2001). Does the Earth have an adaptive infrared iris? *Bulletin of the American Meteorological Society*, *82*(3), 417–432. https://doi.org/10.1175/1520-0477(2001)082<0417:DTEHAA>2.3.CO;2

Liou, K.-N. (2002). *An Introduction to Atmospheric Radiation* (2nd ed.). Amsterdam, the Netherlands: Academic Press.

Mauritsen, T., & Stevens, B. (2015). Missing iris effect as a possible cause of muted hydrological change and high climate sensitivity in models. *Nature Geoscience*, *8*(5), 346–351. https://doi.org/10.1038/ngeo2414

Mlawer, E. J., Taubman, S. J., Brown, P. D., Iacono, M. J., & Clough, S. A. (1997). Radiative transfer for inhomogeneous atmospheres: RRTM, a validated correlated-k model for the longwave. *Journal of Geophysical Research*, *102*(D14), 16663–16682. https://doi.org/10.1029/97JD00237

Mlawer, E. J., Iacono, M. J., Pincus, R., Barker, H. W., Oreopoulos, L., & Mitchell, D. L. (2016). Contributions of the ARM program to radiative transfer modeling for climate and weather applications. *Meteorological Monographs*, *57*, 15.1-15.19. https://doi.org/10.1175/AMSMONOGRAPHS-D-15-0041.1

Morcrette, J.-J. (1991). Radiation and cloud radiative properties in the European Centre for Medium Range Weather Forecasts forecasting system. *Journal of Geophysical Research*, *96*(D5), 9121–9132. https://doi.org/10.1029/89JD01597

Neale, R. B., Richter, J. H., Conley, A. J., Park, S., Lauritzen, P. H., Gettelman, A., … Lin, S.-J. (2010). Description of the NCAR Community Atmosphere Model (CAM 4.0). NCAR Technical Note NCAR/TN-485+STR. Retrieved from http://www.cesm.ucar.edu/models/ccsm4.0/cam/docs/description/cam4_desc.pdf

Neale, R. B., Gettelman, A., Park, S., Chen, C., Lauritzen, P. H., Williamson, D. L., … Taylor, M. A. (2012). Description of the NCAR Community Atmosphere Model (CAM 5.0). NCAR Technical Note NCAR/TN-486+STR. Retrieved from http://www.cesm.ucar.edu/models/cesm1.0/cam/docs/description/cam5_desc.pdf

O'Brien, D. M., Rikus, L. J., Dilley, A. C., & Edwards, M. (1997). Spectral analysis of infrared heating in clouds computed with two-stream radiation codes. *Journal of Quantitative Spectroscopy and Radiative Transfer*, *57*(6), 725–737. https://doi.org/10.1016/S0022-4073(97)00044-7

Pope, V. D., Gallani, M. L., Rowntree, P. R., & Stratton, R. A. (2000). The impact of new physical parametrizations in the Hadley Centre climate model: HadAM3. *Climate Dynamics*, *16*(2–3), 123–146. https://doi.org/10.1007/s003820050009

Ramachandran, S., Ramaswamy, V., Stenchikov, G. L., & Robock, A. (2000). Radiative impact of the Mount Pinatubo volcanic eruption: Lower stratospheric response. *Journal of Geophysical Research: Atmospheres*, *105*(D19), 24409–24429. https://doi.org/10.1029/2000JD900355

Ramanathan, V., & Downey, P. (1986). A nonisothermal emissivity and absorptivity formulation for water vapor. *Journal of Geophysical Research*, *91*(D8), 8649–8666. https://doi.org/10.1029/JD091iD08p08649

Ramanathan, V., Cess, R. D., Harrison, E. F., Minnis, P., Barkstrom, B. R., Ahmad, E., & Hartmann, D. (1989). Cloud-radiative forcing and climate: Results from the Earth radiation budget experiment. *Science*, *243*(4887), 57–63. https://doi.org/10.1126/science.243.4887.57

Rapp, A. D., Kummerow, C., Berg, W., & Griffith, B. (2005). An evaluation of the proposed mechanism of the adaptive infrared iris hypothesis using TRMM VIRS and PR measurements. *Journal of Climate*, *18*(20), 4185–4194. https://doi.org/10.1175/JCLI3528.1

Ritter, B., & Geleyn, J.-F. (1992). A comprehensive radiation scheme for numerical weather prediction models with potential applications in climate simulations. *Monthly Weather Review*, *120*(2), 303–325. https://doi.org/10.1175/1520-0493(1992)120<0303:ACRSFN>2.0.CO;2

Roeckner, E., Bäuml, G., Bonaventura, L., Brokopf, R., Esch, M., Giorgetta, M., … Tompkins, A. (2003). The atmospheric general circulation model ECHAM 5. PART I: Model description. MPI-Report No. 349. Retrieved from http://www.mpimet.mpg.de/fileadmin/publikationen/Reports/max_scirep_349.pdf

Rossow, W. B., & Schiffer, R. A. (1991). ISCCP cloud data products. *Bulletin of the American Meteorological Society*, *72*(1), 2–20. https://doi.org/10.1175/1520-0477(1991)072<0002:ICDP>2.0.CO;2

Rossow, W. B., & Schiffer, R. A. (1999). Advances in understanding clouds from ISCCP. *Bulletin of the American Meteorological Society*, *80*(11), 2261–2288. https://doi.org/10.1175/1520-0477(1999)080<2261:AIUCFI>2.0.CO;2

Saha, S., Moorthi, S., Pan, H.-L., Wu, X., Wang, J., Nadiga, S., … Goldberg, M. (2010). The NCEP Climate Forecast System Reanalysis. *Bulletin of the American Meteorological Society*, *91*(8), 1015–1058. https://doi.org/10.1175/2010BAMS3001.1

Saha, S., Moorthi, S., Wu, X., Wang, J., Nadiga, S., Tripp, P., … Becker, E. (2014). The NCEP Climate Forecast System Version 2. *Journal of Climate*, *27*(6), 2185–2208. https://doi.org/10.1175/JCLI-D-12-00823.1

Schiffer, R. A., & Rossow, W. B. (1983). The International Satellite Cloud Climatology Project (ISCCP): The first project of the world climate research programme.

Bulletin of the American Meteorological Society, *64*(7), 779–784. https://doi.org/10.1175/1520-0477-64.7.779

Schiffer, R. A., & Rossow, W. B. (1985). ISCCP global radiance data set: A new resource for climate research. *Bulletin of the American Meteorological Society*, *66*(12), 1498–1505. https://doi.org/10.1175/1520-0477(1985)066<1498:IGRDSA>2.0.CO;2

Schmidt, G. A., Ruedy, R., Hansen, J. E., Aleinov, I., Bell, N., Bauer, M., … Yao, M.-S. (2006). Present-day atmospheric simulations using GISS ModelE: Comparison to in situ, satellite, and reanalysis data. *Journal of Climate*, *19*(2), 153–192. https://doi.org/10.1175/JCLI3612.1

Schmidt, G. A., Kelley, M., Nazarenko, L., Ruedy, R., Russell, G. L., Aleinov, I., … Zhang, J. (2014). Configuration and assessment of the GISS ModelE2 contributions to the CMIP5 archive. *Journal of Advances in Modeling Earth Systems*, *6*(1), 141–184. https://doi.org/10.1002/2013MS000265

Schwarzkopf, M. D., & Ramaswamy, V. (1999). Radiative effects of CH4 , N2O, halocarbons and the foreign-broadened H2O continuum: A GCM experiment. *Journal of Geophysical Research: Atmospheres*, *104*(D8), 9467–9488. https://doi.org/10.1029/1999JD900003

Stephens, G. L., Tsay, S.-C., Stackhouse, P. W., & Flatau, P. J. (1990). The relevance of the microphysical and radiative properties of cirrus clouds to climate and climatic feedback. *Journal of the Atmospheric Sciences*, *47*(14), 1742–1754. https://doi.org/10.1175/1520-0469(1990)047<1742:TROTMA>2.0.CO;2

Stephens, G. L., Gabriel, P. M., & Partain, P. T. (2001). Parameterization of atmospheric radiative transfer. Part I: Validity of simple models. *Journal of the Atmospheric Sciences*, *58*(22), 3391–3409. https://doi.org/10.1175/1520-0469(2001)058<3391:POARTP>2.0.CO;2

Stevens, B., Giorgetta, M., Esch, M., Mauritsen, T., Crueger, T., Rast, S., … Roeckner, E. (2013). Atmospheric component of the MPI-M Earth System Model: ECHAM6. *Journal of Advances in Modeling Earth Systems*, *5*(2), 146–172. https://doi.org/10.1002/jame.20015

Stubenrauch, C. J., Rossow, W. B., Kinne, S., Ackerman, S., Cesana, G., Chepfer, H., … Zhao, G. (2013). Assessment of global cloud datasets from satellites: Project and database initiated by the GEWEX radiation panel. *Bulletin of the American Meteorological Society*, *94*(7), 1031–1049. https://doi.org/10.1175/BAMS-D-12-00117.1

Su, H., Jiang, J. H., Gu, Y., Neelin, J. D., Kahn, B. H., Feldman, D., … Read, W. G. (2008). Variations of tropical upper tropospheric clouds with sea surface temperature and implications for radiative effects. *Journal of Geophysical Research*, *113*(D10), D10211. https://doi.org/10.1029/2007JD009624

Tang, G., Yang, P., Kattawar, G. W., Huang, X., Mlawer, E. J., Baum, B. A., & King, M. D. (2018). Improvement of the simulation of cloud longwave scattering in broadband radiative transfer models. *Journal of the Atmospheric Sciences*, *75*(7), 2217–2233. doi:10.1175/JAS-D-18-0014.1

von Salzen, K., Scinocca, J. F., McFarlane, N. A., Li, J., Cole, J. N. S., Plummer, D., … Solheim, L. (2013). The Canadian Fourth Generation Atmospheric Global Climate Model (CanAM4). Part I: Representation of physical processes. *Atmosphere-Ocean*, *51*(1), 104–125. https://doi.org/10.1080/07055900.2012.755610

Yang, P., Liou, K., Bi, L., Liu, C., Yi, B., & Baum, B. A. (2015). On the radiative properties of ice clouds: Light scattering, remote sensing, and radiation parameterization. *Advances in Atmospheric Sciences*, *32*(1), 32–63. https://doi.org/10.1007/s00376-014-0011-z

Zdunkowski, W. G., Panhans, W.-G., Welch, R. M., & Korb, G. J. (1982). A radiation scheme for circulation and climate models. *Contributions to Atmospheric Physics*, *55*, 215–238.

Zhang, Y., Macke, A., & Albers, F. (1999). Effect of crystal size spectrum and crystal shape on stratiform cirrus radiative forcing. *Atmospheric Research*, *52*(1–2), 59–75. https://doi.org/10.1016/S0169-8095(99)00026-5

2. IMPACT OF MULTIPLE SCATTERING ON LONGWAVE RADIATIVE TRANSFER INVOLVING CLOUDS*

2.1 Introduction

Clouds cover approximately 67% of the globe according to observations made by the Moderate Resolution Imaging Spectrometer (MODIS) (King et al., 2013), and significantly affect the global energy budget (Baran, 2012; Hansen et al., 1997; Liou, 1986; Stephens, 2005; Stephens et al., 1990, 2001; Yang et al., 2015; Yi et al., 2013). If clouds absorb more longwave (LW) radiation from the surface and the lower part of the atmosphere than the LW energy they emit and the solar radiation they reflect to space, clouds retain energy in the atmosphere and warm the surface and the atmosphere. Conversely, clouds cool the earth-atmosphere system if they emit more LW radiation and reflect more solar radiation than the LW radiation they absorb.

Model approximations of radiative processes cause uncertainties in climate simulations. In the LW spectral bands, since cloud absorption dominates the extinction of radiation, fluxes are usually calculated by approximations that account for absorption only. However, several studies documented significant influences of scattering in LW radiative transfer. From GCM simulations, when LW scattering is included, Stephens et al. (2001) estimate that the global mean OLR decreases by 8 W/m^2, and Schmidt et al.

---

* Reprinted with permission from "Impact of multiple scattering on longwave radiative transfer involving clouds" by Kuo, C.-P., Yang, P., Huang, X.L., Feldman, D., Flanner, M., Kuo, C., & Mlawer, E. J., 2017. *Journal of Advances in Modeling Earth Systems*, 9(8), 3082–3098, Copyright 2017 by John Wiley and Sons.

(2006) state that OLR decreases by approximately 1.5 W/m^2 and increases surface downward flux by about 0.4 W/m^2. Using surface observations, Joseph and Min (2003) suggest that OLR is overestimated by as much as 6-8 W/m^2 due to neglecting LW scattering by thin cirrus clouds. By using the International Satellite Cloud Climatology Project (ISCCP) version D2 (Rossow & Schiffer, 1991) data, Costa and Shine (2006) estimate a 3 W/m^2 reduction in OLR from 60°S to 60°N due to light scattering.

According to those studies, estimates of the influence of LW light scattering by clouds on the global mean OLR range from 1.5 to 8 W/m^2. To estimate the effect of excluding LW scattering contributions, Costa and Shine (2006) suggest setting the scattering cross section to zero, whereas Schmidt et al. (2006) recommend setting the asymmetry factor to unity. Although their approaches differ because they use different theories to account for LW scattering, both non-scattering simulations are performed by using cloud absorption rather than extinction optical thickness. Therefore, their estimated influences on the global mean OLR are similar. However, a 8 W/m^2 reduction on the global mean OLR estimated by Stephens et al. (2001) is larger than the estimates by Costa and Shine (2006) and Schmidt et al. (2006), and is similar to the largest evaluations in Joseph and Min (2003) by using ground observations when thin cirrus clouds are present. As mentioned by Costa and Shine (2006), the assessments in Stephens et al. (2001) are overestimated and the large overestimate is possibly caused by not considering cloud fractions in the simulations, because such a large influence occurs only under overcast conditions when high clouds exist.

Cloud information in the previous studies was from single ground observation site for ice clouds (Joseph & Min, 2003), GCM simulations (Schmidt et al., 2006; Stephens et al., 2001) or a climatological summary (Costa & Shine, 2006). These datasets are spatially coarse or may not provide realistic cloud top and base heights. With high spatial resolution cloud top and base heights now available from Cloud-Aerosol Lidar and Infrared Pathfinder Satellite Observation (CALIPSO) and CloudSat observations, we characterize the uncertainties of flux and heating rate simulations by using rigorous radiative transfer calculations combined with state-of-the-art cloud optics models to give an evaluation of climate effects based on the current level of understanding of cloud radiative properties. The remaining portion of this paper is organized as follows. The microphysical and bulk optical properties of clouds are described in section 2.2. In section 2.3, we outline the settings of the radiative transfer model (RTM) and the satellite data used in the simulations. Results and a discussion are given in section 2.4. Section 2.5 gives the conclusions of this study.

2.2 Cloud microphysical and optical properties

This study uses the MODIS Collection 6 (MC6) cloud optics models (Platnick et al., 2015, 2017), which assume an ensemble of aggregates composed of 8 severely roughened columns for ice cloud particles and spheres for water cloud droplets. For the MC6 ice cloud model (Platnick et al., 2015, 2017), the single-scattering properties of individual ice particles are provided by an ice crystal library (Bi & Yang, 2017; Yang et al., 2013), including the extinction efficiency, single-scattering albedo, asymmetry parameter, phase function, and particle volume and projected area. The refractive index

of ice applied in the library is from Warren and Brandt (2008). The library provides the optical properties of ice crystals for three degrees of roughness, namely, smooth, moderately rough, and severely rough. Roughened ice crystals are demonstrated from in-situ observations and satellite measurements, although the physical processes that cause the observed roughening are not well understood (Baum et al., 2011, 2014; Cole et al., 2013; Ding et al., 2016; Hioki et al., 2016a; Holz et al., 2016; Ulanowski et al., 2006, 2012). Furthermore, the treatment of forward scattering is improved to explicitly overcome the inadequacies of delta-transmission (Bi et al., 2009). Yang et al. (2008a,b) discuss the treatment of surface roughness of an ice particle and the resulting uncertainties in ice cloud property retrievals. The features of the ice cloud model include spectral consistency between MODIS-based solar and thermal retrievals (Baum et al., 2014) and better agreement of ice cloud optical thickness retrievals between the MODIS-based thermal method and CALIOP (Cloud Aerosol Lidar with Orthogonal Polarization) lidar ratios (Holz et al., 2016). For the MC6 water cloud model (Platnick et al., 2015, 2017), the Lorenz-Mie theory (Bohren & Huffman, 1998; van de Hulst, 1957) provides the single-scattering properties using the refractive index of water from compilations by Hale and Querry (1973) at wavelengths between 0.25 and 0.69 μm, Palmer and Williams (1974) at wavelengths between 0.69 and 2.0 μm, and Downing and Williams (1975) at wavelengths longer than 2.0 μm.

The effective diameter D_e (Baum et al., 2005a; Baum et al., 2011, 2014; Foot, 1988) is defined to quantify the ensemble-averaged size of a population of irregular ice crystals as follows:

$$D_e = \frac{3\int_{D_{min}}^{D_{max}} V(D)N(D)dD}{2\int_{D_{min}}^{D_{max}} A(D)N(D)dD}, \tag{2.1}$$

where D is the maximum dimension of a particle, D_{max} and D_{max} are the largest and smallest particle maximum dimensions, $N(D)$ is the particle number concentration specified with respect to the maximum dimension D (cm^{-3} cm^{-1}), and V and A are the volume and the projected area of a particle. In the case of spherical particles, D_e reduces to the definition of the effective size in Hansen and Travis (1974). Therefore, we use D_e to consistently define the effective size of both water droplets and ice particles.

Given the optical properties and the particle size distributions (PSDs) of clouds, we average the single-scattering properties of the cloud model by the Planck function (B) at 233 K (Fu et al., 1998; Hong et al., 2009; Yi et al., 2013) in a specific spectral region to get band-averaged bulk-scattering properties (Baum et al., 2005b; Baum et al., 2011, 2014), such as

$$\bar{\sigma}_{ext/sca} = \frac{\int_{\lambda_1}^{\lambda_2}\int_{D_{min}}^{D_{max}} \sigma_{ext/sca}(D,\lambda)B(\lambda)N(D)dDd\lambda}{\int_{\lambda_1}^{\lambda_2}\int_{D_{min}}^{D_{max}} B(\lambda)N(D)dDd\lambda}, \tag{2.2}$$

$$\bar{Q}_{ext} = \frac{\int_{\lambda_1}^{\lambda_2}\int_{D_{min}}^{D_{max}} Q_{ext}(D,\lambda)A(D)B(\lambda)N(D)dDd\lambda}{\int_{\lambda_1}^{\lambda_2}\int_{D_{min}}^{D_{max}} A(D)B(\lambda)N(D)dDd\lambda}, \text{ and} \tag{2.3}$$

$$\bar{g} = \frac{\int_{\lambda_1}^{\lambda_2}\int_{D_{min}}^{D_{max}} g(D,\lambda)\sigma_{sca}(D,\lambda)B(\lambda)N(D)dDd\lambda}{\int_{\lambda_1}^{\lambda_2}\int_{D_{min}}^{D_{max}} \sigma_{sca}(D,\lambda)B(\lambda)N(D)dDd\lambda}, \tag{2.4}$$

where $\bar{\sigma}_{ext/sca}$, $\bar{Q}_{ext}$ and $\bar{g}$ are the band-averaged bulk extinction or scattering cross section, extinction efficiency and asymmetry factor, $\sigma_{ext/sca}$, Q_{ext} and g are the extinction or scattering cross section, the extinction efficiency and the asymmetry factor, and λ_1 and λ_2 are the lower and upper wavelength boundaries of a spectral band among

those of the GCM version of the Longwave Rapid Radiative Transfer Model (RRTMG_LW, Clough et al., 2005; Iacono et al., 2008) listed in Table 2.1. The band-averaged bulk single-scattering albedo ($\bar{\omega}$) is defined as the ratio of the band-averaged bulk scattering and extinction cross section as follows:

$$\bar{\omega} = \frac{\bar{\sigma}_{sca}}{\bar{\sigma}_{ext}}. \tag{2.5}$$

For the MC6 cloud model, PSDs are modified gamma size distributions with an effective variance (Hansen & Travis, 1974) of 0.1 for both water and ice clouds (Platnick et al., 2015).

Table 2.1 RRTMG_LW spectral band intervals.

Band	Wavenumber (cm^{-1})	Band	Wavenumber (cm^{-1})
1	10-350	9	1180-1390
2	350-500	10	1390-1480
3	500-630	11	1480-1800
4	630-700	12	1800-2080
5	700-820	13	2080-2250
6	820-980	14	2250-2380
7	980-1080	15	2380-2600
8	1080-1180	16	2600-3250

Figure 2.1 shows band-averaged $\bar{Q}_{ext}$, $\bar{\omega}$, and $\bar{g}$ from 10 to 3250 cm^{-1} for ice cloud particles with selected D_e values of 20 and 60 μm, and for water clouds with a selected droplet D_e of 20 μm. In general, $\bar{Q}_{ext}$ increases at first and then oscillates to

approach the asymptotic value, 2, for large particles as the wavenumber increases, and water cloud droplets usually have larger values when compared to ice cloud particles with a similar size. For $\bar{g}$, ice clouds have more forward scattering than water clouds when particle sizes are about the same, and larger ice particles have larger values than smaller particles. Since the imaginary part of the refractive index of ice is smaller than that of water between 250 and 750 cm^{-1}, and has a local minimum near 430 cm^{-1}, as shown in Figure 2.2, $\bar{\omega}$ for ice clouds is larger than for water clouds in bands 1 to 5 (10-820 cm^{-1}), and has the largest value in band 2 (350-500 cm^{-1}). However, the imaginary part of the refractive index of water is smaller than that of ice between 1700 and 3000 cm^{-1}, leading to larger water clouds $\bar{\omega}$ values in bands 12 to 16 (1800-3250 cm^{-1}).

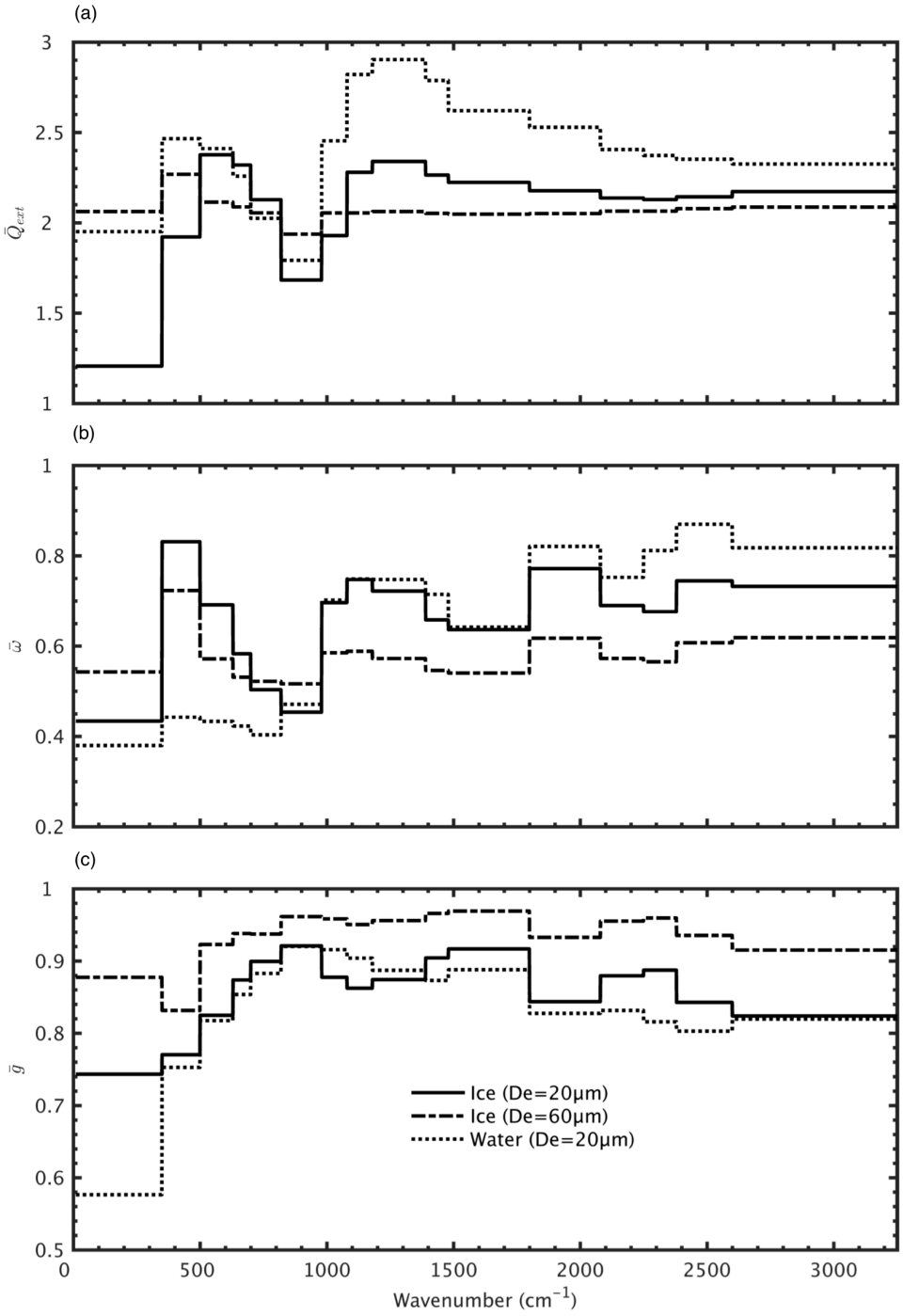

Figure 2.1 Band-averaged (a) bulk extinction efficiency, (b) single-scattering albedo, and (c) asymmetry factor from 10 to 3250 cm^{-1}. Solid and dash-dotted lines are for ice particles with 20 and 60 μm D_e, respectively; dotted lines are for water cloud droplets with 20 μm D_e.

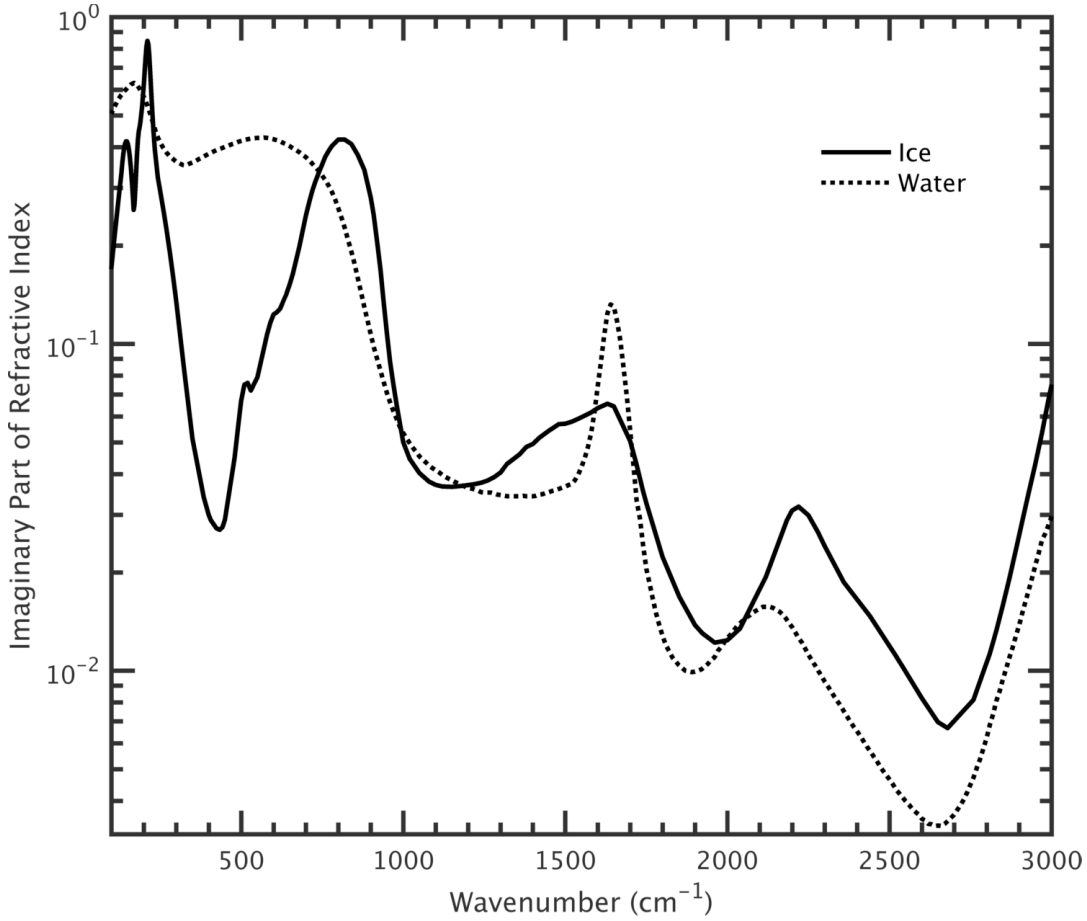

Figure 2.2 Imaginary part of refractive index of (solid line) ice and (dotted line) water cloud from 100 to 3000 cm^{-1}. The refractive index of ice are from Warren and Brandt (2008), and the refractive index of water are combined from Hale and Querry (1973), Palmer and Williams (1974), and Downing and Williams (1975).

2.3 Radiative transfer model settings and satellite observations

Fluxes and heating rates are simulated by RRTMG_LW (Clough et al., 2005; Iacono et al., 2008) and the Discrete Ordinates Radiative Transfer (DISORT) Program for a Multi-Layered Plane-Parallel Medium (Stamnes et al., 1988). RRTMG_LW, which is a frequently used RTM in GCMs and numerical prediction models (Clough et al.,

2005; Iacono et al., 2008), applies the correlated-k-distribution method (Lacis & Oinas, 1991) to account for atmospheric gas absorption, and divides the LW spectrum into the 16 intervals listed in Table 2.1, ranging from wavenumber 10 to 3250 cm^{-1}, in order to balance radiometric accuracy and computational efficiency (Clough et al., 2005; Iacono et al., 2000; Mlawer et al., 1997). In radiative transfer calculations, RRTMG_LW uses a 2-stream model that angular resolution is low and only considers absorption. To rigorously investigate the possible influences of light scattering on flux and heating rate simulations containing clouds, we utilize the 16-stream DISORT (high angular resolution) as a radiative transfer solver, and implant the solver into RRTMG_LW. The optical thicknesses of the atmospheric profiles generated by RRTMG_LW, cloud profiles, and cloud optical properties are input into DISORT to simulate vertical distributions of fluxes and heating rates. The 16-stream DISORT computes fluxes with < 1% differences from an accurate 128-stream DISORT. All of the simulations in this study are offline, and computational time using the 16-stream DISORT takes about 25 times longer than the original RRTMG_LW radiative transfer solver. To overcome the challenge associated with the strong forward peak of the cloud phase functions for radiative transfer simulation, we use the delta-M method (Hioki et al., 2016b; Wiscombe, 1977), which has been developed to ensure accurate flux computations by truncating the phase function and adjusting the optical thickness, single-scattering albedo, and Legendre polynomial expansion coefficients of the phase function based on the similarity principle (Liou, 2002; van de Hulst, 1974; Wiscombe, 1977).

The following satellite observation datasets are analyzed for 2010. The cloud conditions are provided by CCCM Edition B1 products (Kato et al., 2010, 2011, 2014), containing measurements derived from CALIPSO (resolution 333 m), CloudSat (resolution 1.4 km), CERES (resolution 20 km at the near-nadir view), and MODIS (resolution 1 km) observations. To merge cloud top and base heights in a 1 km grid box, three CALIPSO and one CloudSat observations are combined following Kato et al. (2010, Table 1). The merged cloud heights are then collocated with 1 km MODIS observations, and are used as input in the enhanced cloud algorithm (Kato et al., 2011) to improve retrieved cloud optical and microphysical properties from MODIS observations. Then 1 km combined CALIPSO, CloudSat and MODIS data are collocated with CERES footprints to make the grid sizes of the CCCM products approximately 20 km (Kato et al., 2014). In a CCCM grid box, up to 16 unique cloud horizontal boundaries (groups) and up to 6 independent cloud vertical layers are sorted by a grouping process (Kato et al., 2010). Kato et al. (2011) show improvements of flux simulations by using these products, compared with CERES and surface measurements. In this study, we focus on single-layer water and ice clouds (water and ice cloud groups with a single cloud top and base) in 2010, and analyze the contribution of light scattering from different thermodynamic phases of clouds. From the products, the cloud vertical boundaries are defined by the CALIPSO- and CloudSat-derived cloud top and base heights, and the cloud optical and microphysical properties are provided by the MODIS-retrieved cloud optical thickness, effective diameter, fraction and phase. Figure 2.3 presents histograms of the frequency of visible optical thickness and particle size for water and ice clouds. In

2010, both single-layer water and ice clouds most frequently have small optical thicknesses (< 5), and the most abundant particle sizes (D_e) are about 20 μm for water clouds and about 20 to 60 μm for ice clouds. With cloud top and base heights provided from CCCM products, we set the physical thickness of clouds and assume clouds are vertically homogeneous in the model simulations.

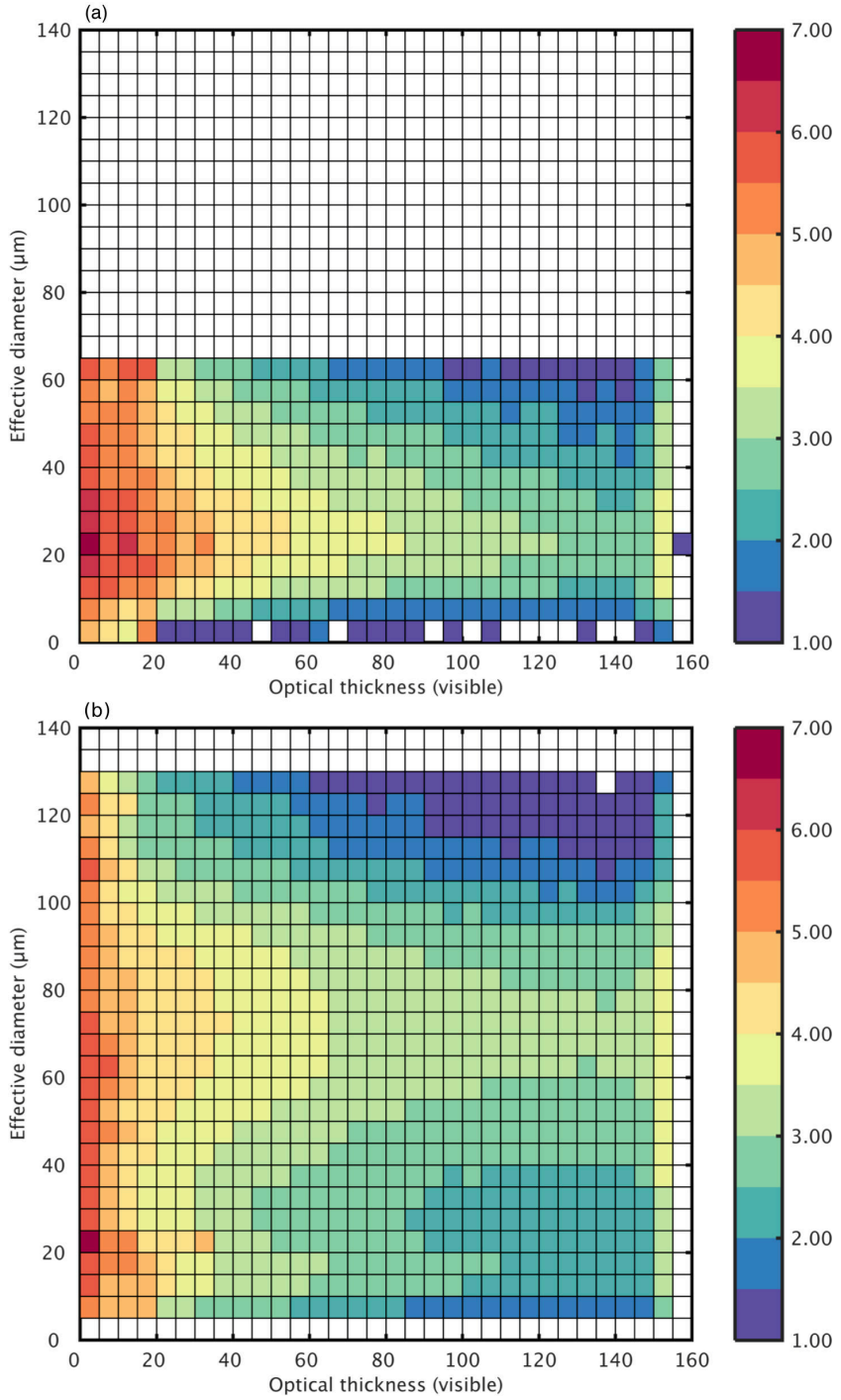

Figure 2.3 Two-dimensional histograms of the number of CCCM merged observations in 2010 in visible optical thickness and particle size bins for single-layer (a) water and (b) ice clouds (water and ice cloud groups with a single cloud top and base). Color bar shows the number of counts in a log scale (10^x).

Atmospheric information, including temperature, humidity and ozone profiles, is provided by the CCCM products, based on the Goddard Earth Observing System (GEOS-5) Data Assimilation System reanalysis (Kato et al., 2014). The vertical range of atmospheric profiles in the simulations is from the surface to 65 km height. In order to simulate more realistic conditions, we follow the Fifth Assessment Report of the Intergovernmental Panel on Climate Change (IPCC, 2014) and set the volume mixing ratios of carbon dioxide (CO_2), nitrous oxide (N_2O), and methane (CH_4) to 390.5, 0.3242, and 1.803 ppmv, respectively.

2.4 Results and discussion

To evaluate the consequences of ignoring light scattering in the LW spectrum by single-layer water and ice clouds, we compare fluxes and heating rates between absorption only and rigorous radiative transfer calculations including light scattering processes. Simulation biases are defined as the difference between calculations where only absorption is considered and more rigorous results that include scattering. Both calculations use the same RTM, which is a customized combination of RRTMG_LW and DISORT. In absorption-only simulations, as suggested by Costa and Shine (2006), we use the absorption optical thicknesses of clouds and set the single-scattering albedo to zero, but the extinction optical thicknesses (i.e., scattering plus absorption optical thicknesses) and complete scattering properties are used in the rigorous calculations considering LW scattering. The absorption optical thicknesses of clouds are the same in these two sets of simulations.

2.4.1 Sensitivity tests

Based on the most abundant observed effective cloud particle sizes from the CCCM products in Figure 2.3, we perform idealized flux simulations for three cloud conditions: Water clouds with 20 μm D_e and ice clouds with 20 and 60 μm D_e. We assume cloud physical thicknesses are 2 km and are divided into 8 layers for computation, and set cloud top heights at 700 hPa for water clouds and 200 hPa for ice clouds. For each cloud condition, we conduct simulations for visible optical thickness up to 25 with three atmospheric profiles: Midlatitude summer (MLS), subarctic winter (SAW), and tropics (TRP) (Anderson et al., 1986). Upward fluxes at the TOA decrease and downward fluxes at the surface increase when clouds become optically opaque, and high clouds have lower TOA upward and surface downward fluxes than low clouds, since temperature decreases with height in the troposphere.

TOA upward flux and surface downward flux biases due to neglecting LW scattering as a function of visible optical thickness for water and ice clouds are shown in Figure 2.4. Compared with pure absorption processes in radiative transfer, scattering changes radiation fields in two ways: 1) scattering the upward fluxes from below and backscattering part of the scattered upward fluxes to the surface, and 2) scattering the downward fluxes from above and backscattering part of the scattered downward fluxes to the TOA. Because the surface is an extra LW radiation source, the upward flux is larger than the downward flux, and upward backscattered fluxes are less than downward backscattered fluxes. Therefore, when scattering is neglected, TOA upward fluxes are overestimated and surface downward fluxes are underestimated. In general, absolute

biases are larger for TOA upward fluxes than for surface downward fluxes, as layers above clouds are more transparent than layers under clouds, and upward scattered fluxes can reach the TOA with little absorption. As shown in Figure 2.4, the magnitudes of biases increase with optical thickness to a maximum when optical thickness is about 2, where the outgoing scattered flux is largest, and then decreases to nearly a constant value when optical thickness is large (about 20). The scattering effects tend to be saturated and the radiation emitted by the cloud that would transmit through the atmosphere if there is no scattering is actually scattered back into the cloud and is partly absorbed.

Due to reduced gas absorption above ice cloud layers, in Figure 2.4 the higher ice clouds have larger TOA upward flux biases than the lower water clouds. In addition, as the atmospheric opacity is relatively smaller for layers under water than ice clouds, downward flux biases at the surface are larger for low water clouds if the optical thickness is small. However, since downward scattered fluxes become saturated when the optical thickness is large and water clouds are more absorptive than ice clouds in RRTMG_LW bands 1 to 5 (Figure 2.1b), which provide major LW emission energy, backscattering within ice clouds becomes significant such that surface downward flux biases for ice clouds are larger than for water clouds. This is especially true in the SAW profile (Figure 2.4b), where the atmosphere is relatively transparent and downward scattered fluxes can reach the surface. In addition, small ice particles have larger $\bar{\omega}$ in all bands except for bands 1, 5 and 6, and smaller $\bar{g}$ in all bands than larger particles (Figure 2.1b,c), so ice clouds with small particles generate more backscattered radiation and have larger surface downward flux biases than with larger particles. Due to the optical

properties (as in Figure 2.1) and altitudes of clouds, absolute biases are larger for ice clouds compared with water clouds with a similar particle size, and are largest for ice clouds with smaller crystal sizes. Comparing the three atmospheric conditions, the largest TOA upward flux bias is approximately 15 W/m^2 in the TRP profile, corresponding to approximately 9.5% of TOA upward flux. For the surface downward flux, the largest absolute bias is approximately 3 W/m^2, which is approximately 1.5% of surface downward flux in the MLS profile.

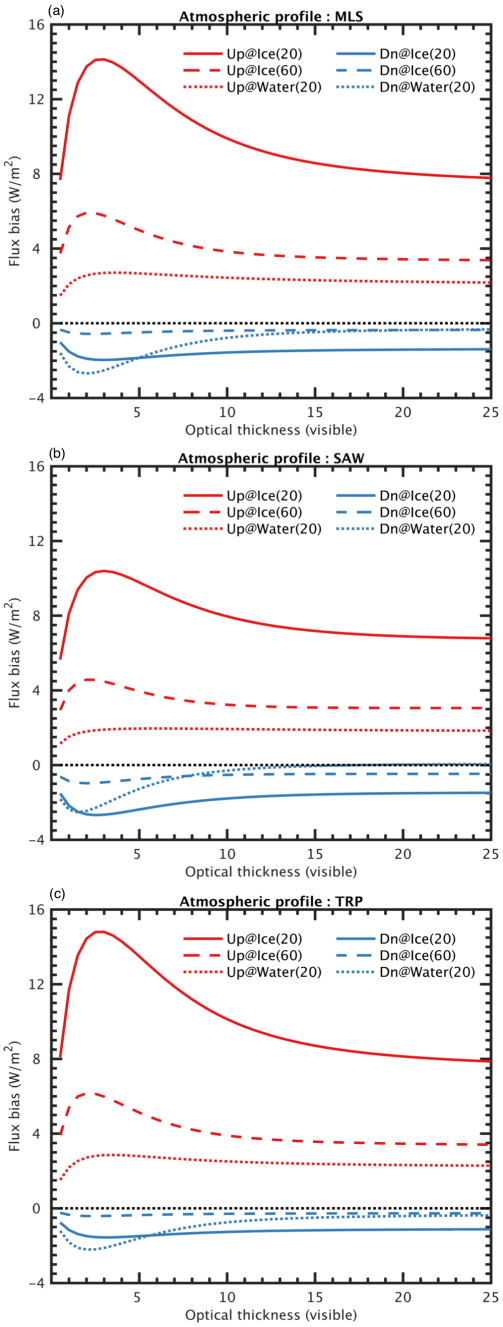

Figure 2.4 Flux biases due to neglecting LW scattering by assuming 2 km thick water cloud (cloud top height at 700 hPa) and ice cloud (cloud top height at 200 hPa) as a function of visible optical thickness under conditions of (a) midlatitude summer (MLS), (b) subarctic winter (SAW), and (c) tropics (TRP). Red lines show upward flux biases at the TOA, and blue lines show downward flux biases at the surface. Solid, dashed, and dotted lines are ice clouds with 20 μm D_e, ice clouds with 60 μm D_e, and water clouds with 20 μm D_e, respectively.

According to the heating rate profiles, the cloud top is being cooled and the base is warmed, and the magnitudes of cooling and warming increase with cloud optical thickness. The heating rate biases in the MLS profile at the cloud top and base layers (0.25 km thickness), the tropopause (179 hPa) (Clough et al., 1992), and the surface are shown in Figure 2.5. Because LW scattering decreases the upward fluxes above the cloud top, heating rate biases are then positive at the cloud top and the tropopause. On the other hand, negative heating rate biases are at the cloud base and the surface, since LW scattering increases the downward fluxes and warms below the cloud base layers. In Figure 2.5a, the absolute cloud top and base heating rate biases increase with optical thickness and then decrease, because the influence of scattering is saturated when optical thickness is large. In addition, similar to Figure 2.4, since ice clouds located at the higher altitude have less gas absorption and larger $\overline{\omega}$ than water clouds in the major LW emission bands (RRTMG_LW bands 1 to 5) as depicted in Figure 2.1b, the magnitudes of heating rate biases are larger for ice than water clouds. Moreover, $\overline{\omega}$ is somewhat larger for ice crystals with smaller than bigger particle size in Figure 2.1b, so absolute heating rate biases are larger for ice clouds with smaller particle size.

We also evaluate heating rate biases at the tropopause and the surface, shown in Figure 2.5b, and the patterns are similar to Figure 2.4a, where biases reach a maximum when the optical thickness is about 2 and then decrease toward a constant value. Since the atmosphere is absorptive in LW spectral bands, the magnitudes of biases at the tropopause and the surface are 2 orders smaller than at the cloud top and base. Although the absolute values are small, for ice clouds with 20 μm D_e from small to large optical

thickness, the tropopause heating rate biases are about 7-16 % of the heating rates at this level and the surface heating rate biases are about 2% of heating rates at the surface. For water clouds with the same D_e, the absolute biases at the tropopause are approximately 5-7% of the tropopause heating rates and at the surface are approximately 2-7% of surface heating rates when optical thickness changes from small to large. Therefore, in idealized simulations, such as in Figure 2.4 and Figure 2.5, the influence of LW scattering is significant not only in the cloud layers but also along the whole atmospheric column.

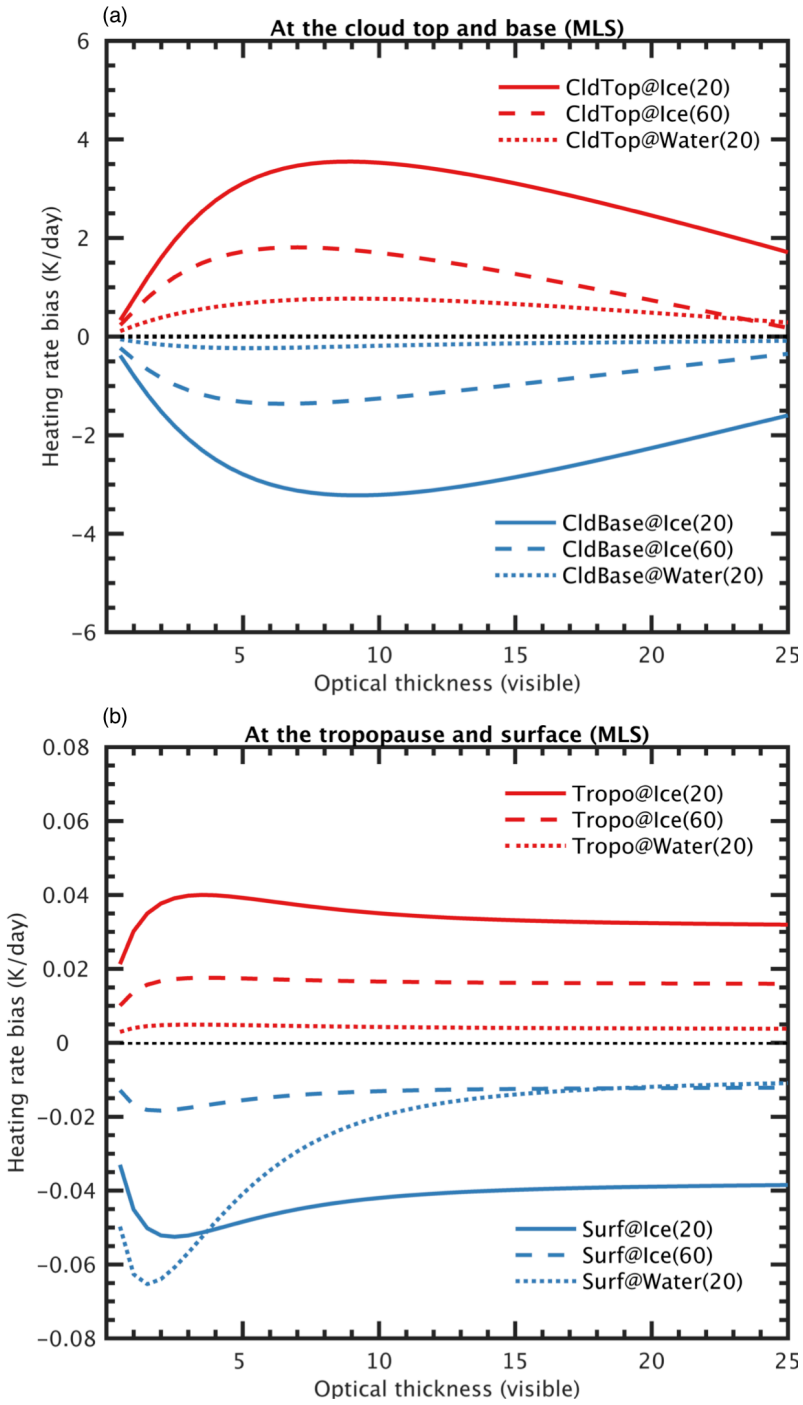

Figure 2.5 Heating rate biases at the (a) cloud top (red) and base (blue), and the (b) tropopause (red) and surface (blue) by assuming 2 km thick water cloud (cloud top height at 700 hPa) and ice cloud (cloud top height at 200 hPa) as a function of visible optical thickness in a MLS atmosphere. Solid, dashed, and dotted lines are ice clouds with 20 μm D_e, ice clouds with 60 μm D_e, and water clouds with 20 μm D_e, respectively.

2.4.2 Global simulations

The global impacts of ignoring LW scattering on flux and heating rate simulations are estimated by using cloud and atmosphere information from CCCM products covering 2010. To spatially represent the flux simulation biases, we average the biases into 1° × 1° resolution. Figure 2.6 shows the global annual mean bias distributions of upward flux at the TOA and of downward flux at the surface. The pattern of TOA upward flux biases is similar to that in Costa and Shine (2006, Figure 6). In general, large biases can be found along the Intertropical Convergence Zone (ITCZ), particularly in the Pacific warm pool, and in the Tibetan Plateau region, since there are many ice clouds. In these regions, OLR is overestimated by up to about 12 W/m^2, because ice clouds locate at higher altitudes with more transparent above-cloud atmospheric layers and have larger scatter properties as in Figure 2.1 than water clouds. In contrast, negative biases of downward flux at the surface are significant (about -3.6 W/m^2) in broad midlatitude regions and mountain areas, especially in the Tibetan Plateau, the Antarctic, and Greenland, because altitudes of these regions are higher and more scattered LW fluxes can reach the surface in a shorter path length without being absorbed by the atmosphere. Since water vapor absorbs most of the downward scattered fluxes, downward flux biases have smaller magnitudes than the upward flux biases. However, in a dry and high elevation area under clouds, the downward scattered fluxes can reach the ground.

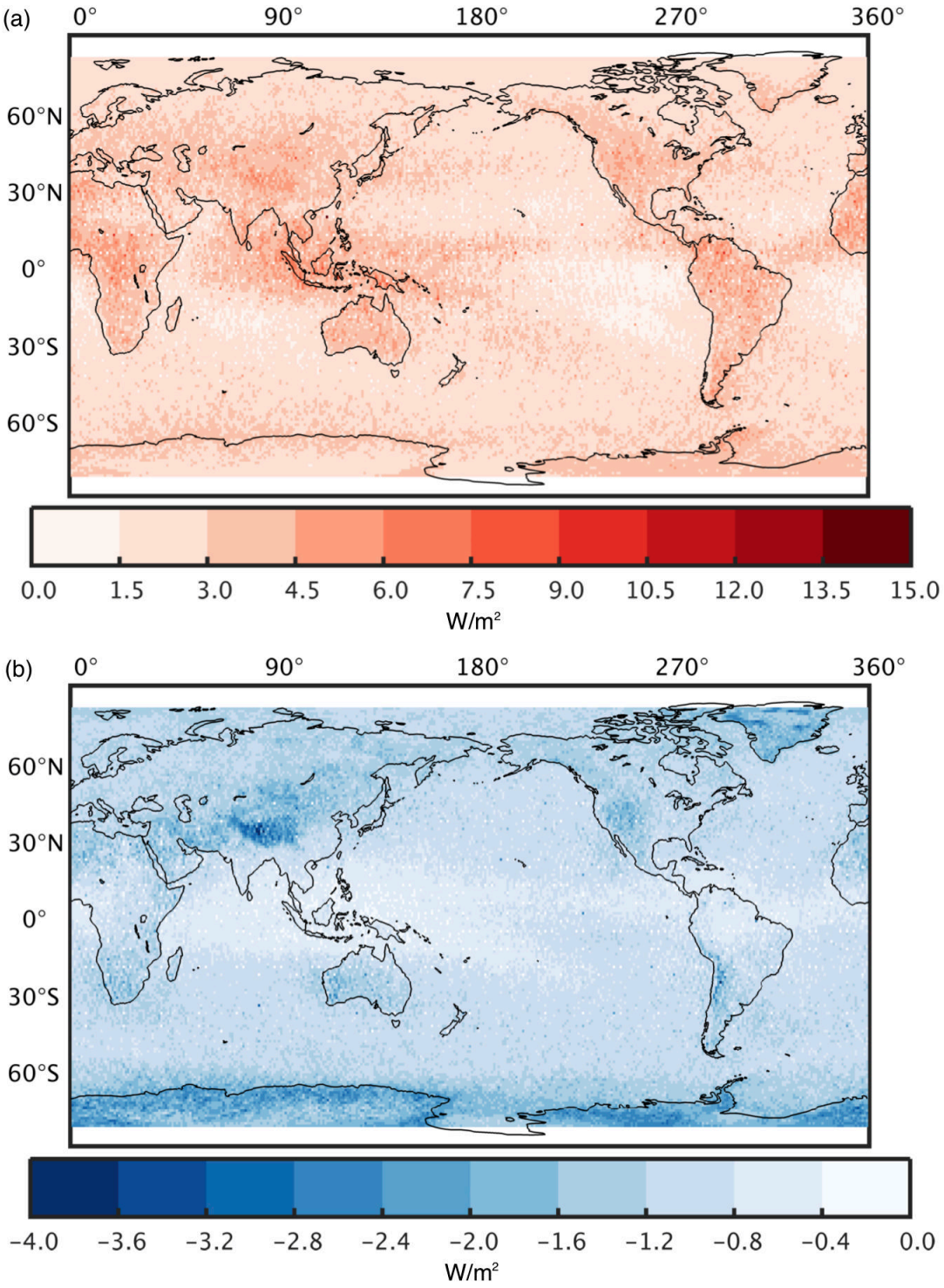

Figure 2.6 Global distributions (1° × 1°) of the annual mean LW biases in 2010 for (a) the upward flux at the TOA and (b) the downward flux at the surface. Blank regions indicate no satellite observations.

Zonal averaged flux and heating rate biases in each month of 2010 are shown in Figure 2.7. In Figure 2.7a, the peak TOA upward flux bias followed the ITCZ shifts from the southern to the northern hemisphere from January to June and shifts back again from July to December. From June to September, the contrast of biases between northern and southern hemispheres is largest. On the other hand, Figure 2.7b presents surface downward flux biases, which are mainly in the midlatitude region, as shown in Figure 2.6b. The surface downward flux biases are close to zero in the tropical regions due to absorption by abundant water vapor. Generally, as previously discussed, the absolute biases are larger for TOA upward flux than surface downward flux.

Figure 2.7c describes the net flux into the atmosphere (NF_A) (Zhang et al., 1995), which is defined as

$$NF_A = F_T^{\downarrow} - F_T^{\uparrow} - (F_S^{\downarrow} - F_S^{\uparrow}), \tag{2.6}$$

where $F_T^{\downarrow}$ and $F_T^{\uparrow}$ are downward and upward flux at the TOA, respectively, and $F_S^{\downarrow}$ and $F_S^{\uparrow}$ are downward and upward flux at the surface, respectively. When the simulations include LW scattering, clouds mainly scatter LW radiation from below and scatter back part of the energy to the ground, giving radiation more chance to be absorbed by the atmosphere, so the biases of net flux into the atmosphere are negative and extreme values vary with the positions of the ITCZ, such as in Figure 2.7a. In Figure 2.7d and Figure 2.7e, heating rate biases are at the tropopause and at the surface, respectively. To evaluate simulation biases at the tropopause, we follow the method mentioned by Reichler et al. (2003) to determine the height of the tropopause. Since LW scattering decreases the amount of radiation reaching higher altitudes above the cloud layers,

heating rate biases at the tropopause have similar monthly variations as in Figure 2.7a such that the locations of the largest absolute bias are in the southern hemisphere from January to March, in the northern hemisphere from April to November, and in the southern hemisphere again in December. In Figure 2.7e, the largest surface heating rate biases are in the midlatitude areas, as anticipated from Figure 2.7b. Although the ITCZ is persistently cloudy, absolute heating rate biases at the surface are relatively small in this region, because downward scattered radiation is absorbed by water vapor before transferring to the surface.

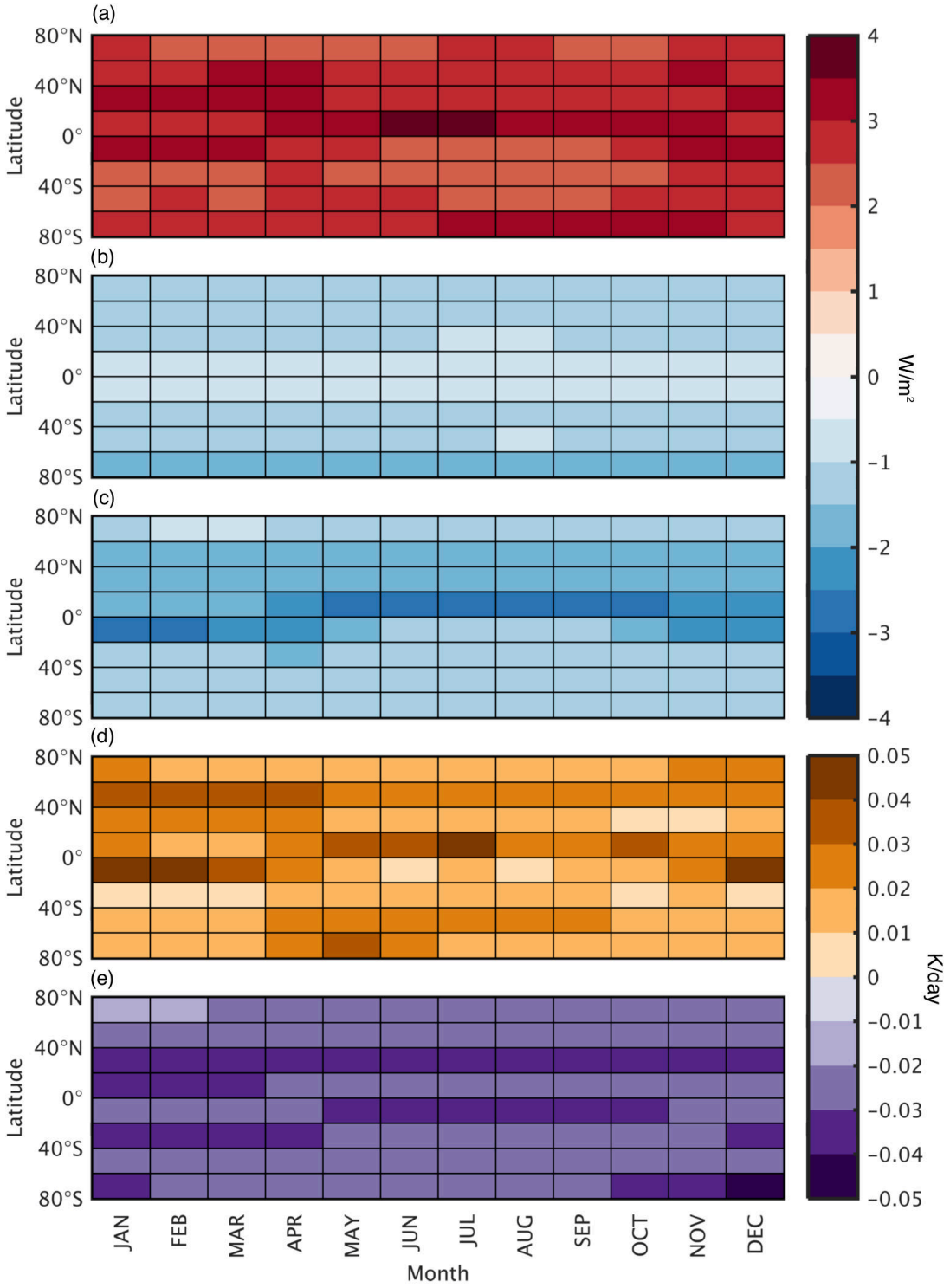

Figure 2.7 Monthly zonal mean LW biases in 2010 of (a) the upward flux at the TOA, (b) the downward flux at the surface, (c) the net flux into the atmosphere, (d) the heating rate at the tropopause, and (e) the heating rate at the surface.

Global annual averaged flux biases are depicted in Figure 2.8a and summarized in Table 2.2 with corresponding root mean square errors (RMSEs). Due to the optical properties (as in Figure 2.1) and altitudes of clouds, the global annual mean TOA upward flux bias for ice clouds (4.4 W/m^2) is larger than for water clouds (1.6 W/m^2). The annual mean downward flux bias at the surface is similar for ice (-1.3 W/m^2) and water (-1.1 W/m^2) clouds, since the atmosphere is opaque under cloud layers. In Figure 2.8a, the upward flux biases at the TOA are slightly smaller than at the tropopause for both water and ice clouds, because a fraction of the upward scattered fluxes are absorbed by the atmosphere above the tropopause. However, the downward flux biases at the tropopause are mainly from ice clouds, since most of water cloud layers are lower than the tropopause. When LW light scattering is considered, about 3.1 W/m^2 remains in the atmosphere when ice clouds exist, and for the existence of water clouds approximately 0.5 W/m^2 remains in the atmosphere.

Averaging globally over water and ice clouds and neglecting LW scattering, upward flux at the TOA is overestimated by 2.6 W/m^2 and downward flux at the surface is underestimated by 1.2 W/m^2. The results are similar to the estimates in Costa and Shine (2006), which are 3 W/m^2 overestimation for TOA upward flux and 1.1 W/m^2 underestimation for surface downward flux from 60°S to 60°N. Globally, about 1.4 W/m^2 is absorbed in the atmosphere involving single-layer clouds and considering LW scattering. While the global mean flux biases are relatively small compared to the total TOA upward flux (233.8 W/m^2) and surface downward flux (351.9 W/m^2) from multi-sensor observations (Henderson et al., 2013), simulated biases are larger in some regions

(Figure 2.6a), up to 9-12 W/m^2 over the ITCZ, or as much as 5% of total TOA upward flux. Compared to the LW cloud radiative effect of 27.2 W/m^2 at the TOA or 25.6 W/m^2 at the surface (Henderson et al., 2013), biases of TOA upward flux are about 10% and biases of surface downward flux are about 5% of LW cloud radiative effect.

Table 2.2 2010 global and annual mean biases and respective RMSEs for upward flux at the TOA and at the tropopause, downward flux at the tropopause and at the surface, and net flux into the atmosphere for total clouds, ice clouds, and water clouds.

	Unit (W/m^2)	Total Clouds	Ice Clouds	Water Clouds
Upward Flux (TOA)	Bias	2.6	4.4	1.6
	RMSE	3.6	5.3	1.8
Upward Flux (Tropopause)	Bias	2.7	4.4	1.6
	RMSE	3.6	5.4	1.9
Downward Flux (Tropopause)	Bias	-0.1	-0.2	-0.004
	RMSE	0.5	0.8	0.1
Downward Flux (Surface)	Bias	-1.2	-1.3	-1.1
	RMSE	1.6	1.8	1.4
NF_A	Bias	-1.4	-3.1	-0.5
	RMSE	2.7	4.1	1.0

Figure 2.8b shows global annual mean heating rate biases, and Table 2.3 lists the values and their respective RMSEs. Annual averaged biases are about -0.005 (< 1%), -0.042 (< 1%), 0.006 (< 1%), -0.034 (about 6.3%), 0.018 (about -3%), and -0.028 (about 2.3%) K/day, for the whole atmosphere column, in cloud layers, above cloud layers, under cloud layers, at the tropopause and at the surface, respectively. The values in the parentheses are percentage errors relative to heating rates for each layer. Since clouds mostly scatter back a fraction of upward radiation illuminating clouds from below to the ground, heating rate biases in and under cloud layers are negative, and above cloud layers are positive. Therefore, the global averaged magnitudes of column mean biases have relatively small values. Overall, scattered LW radiation is eventually absorbed in clouds, so the largest absolute heating rate biases are in the cloud layers. Although the absolute biases are large in the cloud layers, LW scattering causes relatively larger biases under cloud layers, at the tropopause and at the surface. In general, the magnitudes of heating rate biases are larger for ice clouds than for water clouds, especially at the tropopause where the RMSE is also largest.

Table 2.3 2010 global annual mean biases and respective RMSEs of column mean, cloud layer mean, above cloud layer mean, under cloud layer mean, tropopause, and surface heating rate biases for total clouds, ice clouds, and water clouds. Column, cloud, above cloud, and under cloud heating rate biases indicate averaged heating rate biases over the whole atmospheric profile, in cloud layers, in layers above clouds, and in layers under clouds, respectively.

	Unit (K/day)	Total Clouds	Ice Clouds	Water Clouds
Column	Bias	-0.005	-0.010	-0.001
	RMSE	0.010	0.014	0.005
Cloud	Bias	-0.042	-0.034	-0.047
	RMSE	0.102	0.074	0.116
Above Cloud	Bias	0.006	0.008	0.005
	RMSE	0.008	0.010	0.006
Under Cloud	Bias	-0.034	-0.041	-0.030
	RMSE	0.044	0.053	0.037
Tropopause	Bias	0.018	0.044	0.002
	RMSE	0.126	0.200	0.033
Surface	Bias	-0.028	-0.026	-0.029
	RMSE	0.046	0.041	0.048

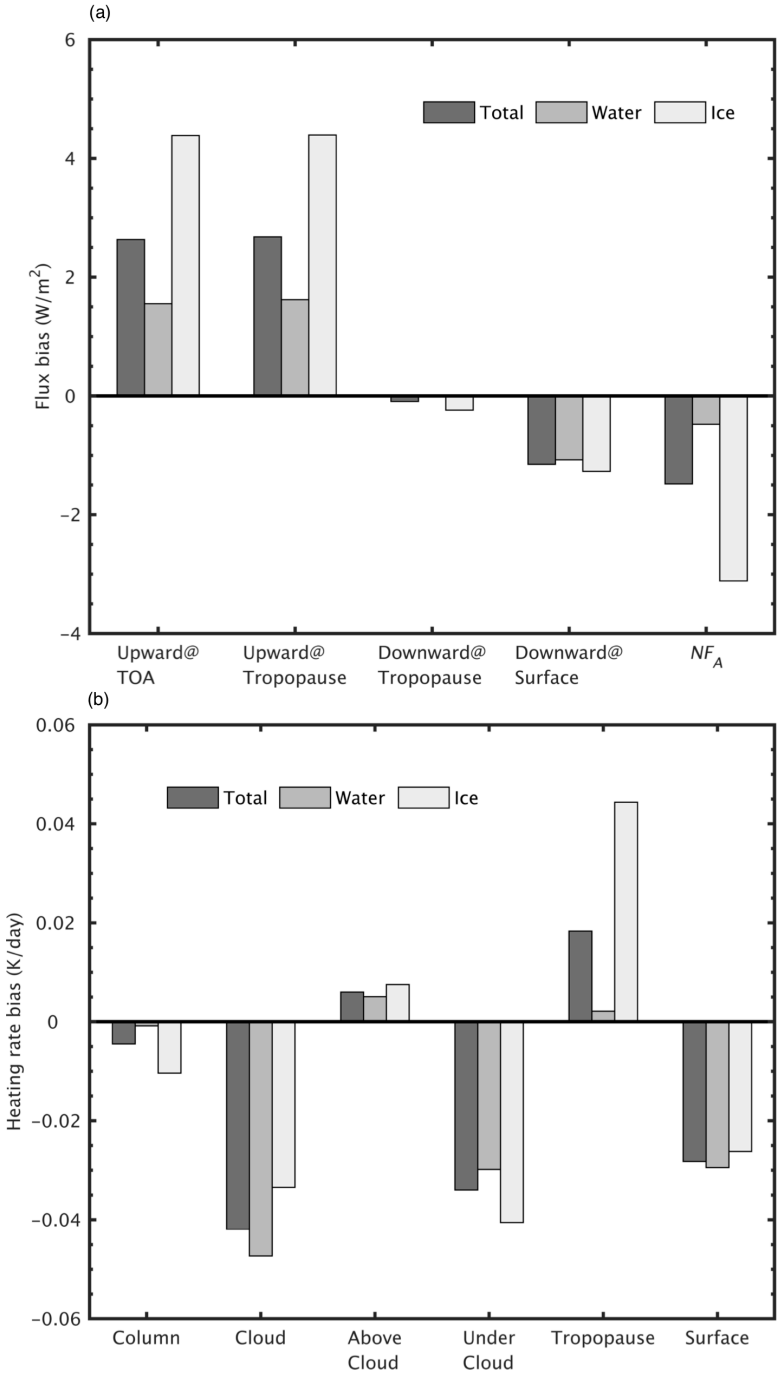

Figure 2.8 Annual global mean LW biases in 2010 of (a) the upward flux at the TOA and the tropopause, the downward flux at the tropopause and the surface, and the net flux into the atmosphere, and (b) the mean heating rate biases through the whole atmosphere column, in cloud layers, above cloud layers, under cloud layers, at the tropopause, and at the surface. “Total”, “water”, and “ice” mean total clouds, water clouds only, and ice clouds only, respectively.

To further demonstrate the importance of LW scattering, we compare the effect of neglecting LW scattering with the clear-sky radiative effect of doubling CO_2. As listed in Table 1, in Clough and Iacono (1995), when the concentration of CO_2 doubles from 355 to 710 ppmv under midlatitude summer conditions, upward fluxes at the TOA and tropopause decrease about 2.8 (2.6) and 3.9 (2.7) W/m^2, respectively, and downward fluxes at the surface and tropopause increase approximately 1.8 (1.2) and 1.7 (0.1) W/m^2, respectively, and cause heating about 0.069 (0.028) K/day at the surface and about 0.00002 (-0.018) K/day at the tropopause. The values in the parentheses are equivalent simulation biases listed in Table 2.2 and Table 2.3. Overall, the simulation biases are comparable to the radiative effects of doubling CO_2.

Due to varying optical properties of clouds in each RRTMG_LW spectral band (Figure 2.1), the contributions of light scattering vary by bands, and the cumulative flux biases from 10 to 3250 cm^{-1} are shown in Figure 2.9. Since ice clouds have larger ϖ in the main LW emission bands (10-820 cm^{-1}, shown in Figure 2.1b) at Earth surface temperatures, flux biases of ice clouds are larger than for water clouds in those bands. Especially, as mentioned in section 2.2, ϖ is largest in band 2 (350-500 cm^{-1}) for ice clouds compared to water clouds, because the imaginary part of refractive index is relatively small for ice in that spectral range (Figure 2.2). Therefore, at the TOA, band 2 contributes over 40% of ice clouds flux biases, whereas band 2 only accounts for about 3% of water clouds flux biases. This confirms the implication in Chen et al. (2014) that ice clouds have a stronger scattering effect in far-infrared than in middle-infrared spectral regions. Although the ice cloud model is different, the simulations made by

Edwards and Slingo (1996) also support the results that LW scattering is most important around 400 cm^{-1}.

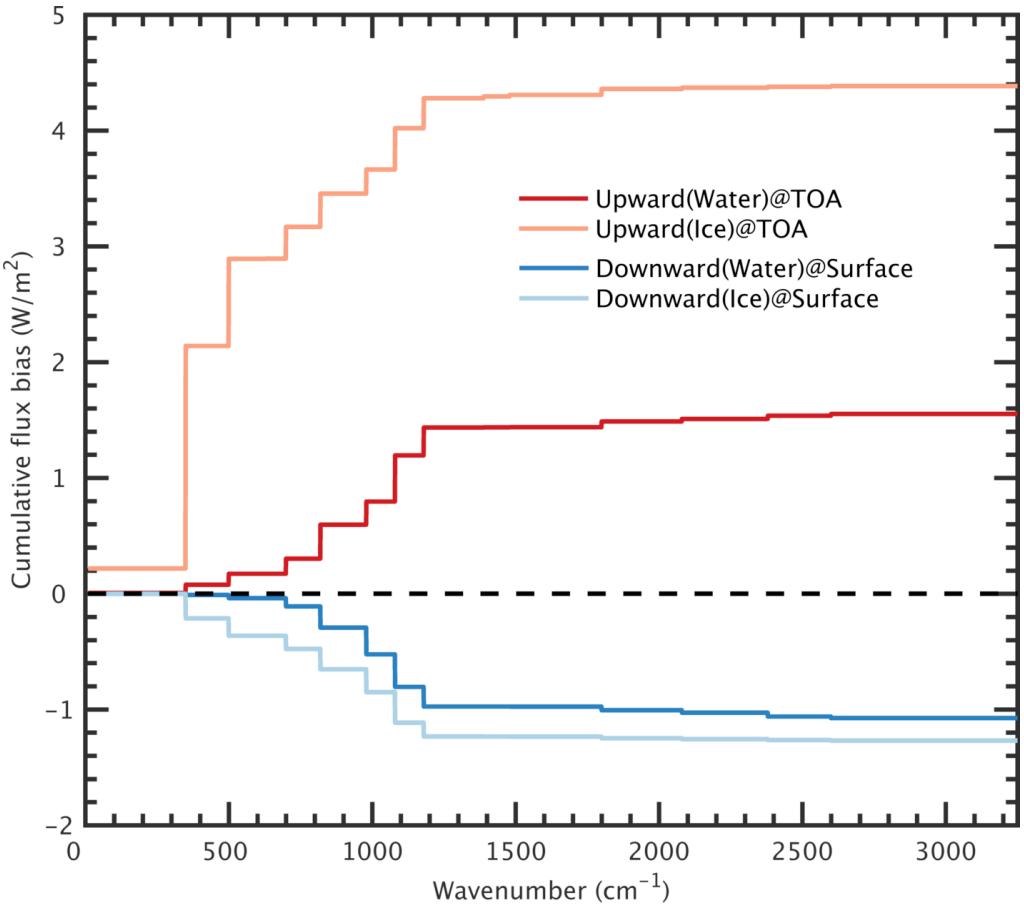

Figure 2.9 Cumulative biases of upward flux at the TOA (red or orange) and downward flux at the surface (blue or light blue) from 10 to 3250 cm^{-1} for water and ice clouds in 2010. Water (ice) means flux biases contributed by water (ice) clouds only.

In addition to the optical properties of clouds, gas absorption also plays an important role in spectral flux biases (Figure 2.9). Since the atmosphere is relatively

transparent above clouds, the scattered upward fluxes can reach the TOA without being absorbed by gas, particularly by water vapor. As a result, the magnitudes of upward flux biases at the TOA are larger than the downward flux biases at the surface. However, for both water and ice clouds, the magnitudes of biases for upward flux at the TOA or downward flux at the surface are similar in bands 5 to 9 (700-1390 cm^{-1}). As those spectral regions are in the atmospheric window, scattered fluxes transfer through the spectrally transparent part of the atmosphere. In bands 10 to 16 (1390-3250 cm^{-1}), the intensities of scattered fluxes are small because of gas absorption, and a lack of LW emitted fluxes. Therefore, spectral flux biases are mainly contributed by far-infrared and the atmospheric window regions (10-1390 cm^{-1}).

As mentioned by Tselioudis et al. (2013), using CALIPSO and CloudSat, the cloud top and base height are detected and can be used to distinguish different cloud regimes. In this study, with the CALIPSO- and CloudSat-derived cloud top and base heights in the CCCM products, we separate 6 cloud regimes for cloud groups with a single cloud top and base, including HxMxL, HxM, MxL, 1H, 1M, and 1L, where 440 hPa separates high (H) and middle (M) clouds, and 680 hPa separates middle (M) and low (L) clouds. 1H, 1M, and 1L refer to single-layer high, middle, and low clouds, respectively; and HxMxL, HxM, and MxL denote continuous cloud layers from high to low, high to middle, and middle to low clouds, respectively.

Figure 2.10 presents flux and heating rate biases in the 6 cloud regimes. As the atmosphere above cloud layers is comparatively transparent, when LW scattering is neglected, TOA upward fluxes are overestimated by as much as 5 W/m^2 when high

clouds (HxMxL, HxM, and 1H) exist, or up to 2.9 W/m^2 when the highest clouds are middle clouds (MxL and 1M), or 1.4 W/m^2 when only low clouds (1L) exist. Scattering effects are especially important for high clouds, since they account for approximately 58% of LW cloud radiative forcing at the TOA, as estimated by Hartmann et al. (1992). Due to gas absorptions below clouds, LW scattering adds about 1.4 W/m^2 to surface downward fluxes when clouds are present, except for 1H clouds (0.7 W/m^2). Overall, when light scattering is considered, high clouds absorb more LW radiation than low clouds. Particularly, HxMxL and 1H clouds accumulate about 4 W/m^2 in the atmosphere. Similarly, the resulting heating rate biases are larger for high than low clouds, ranging from -0.014 K/day for 1H clouds to nearly zero for 1L clouds. In general, higher clouds have larger flux and heating rate biases.

Throughout the analyses, we notice that the values of RMSEs listed in Table 2.2 and Table 2.3 are larger than the respective average biases. Since not only cloud microphysical and optical properties, as in Figure 2.1 and Figure 2.3, but also cloud physical thicknesses and atmospheric conditions, vary around the globe, large biases can be found locally as in Figure 2.6. As a result, all RMSEs are considerably larger than the magnitudes of global mean biases.

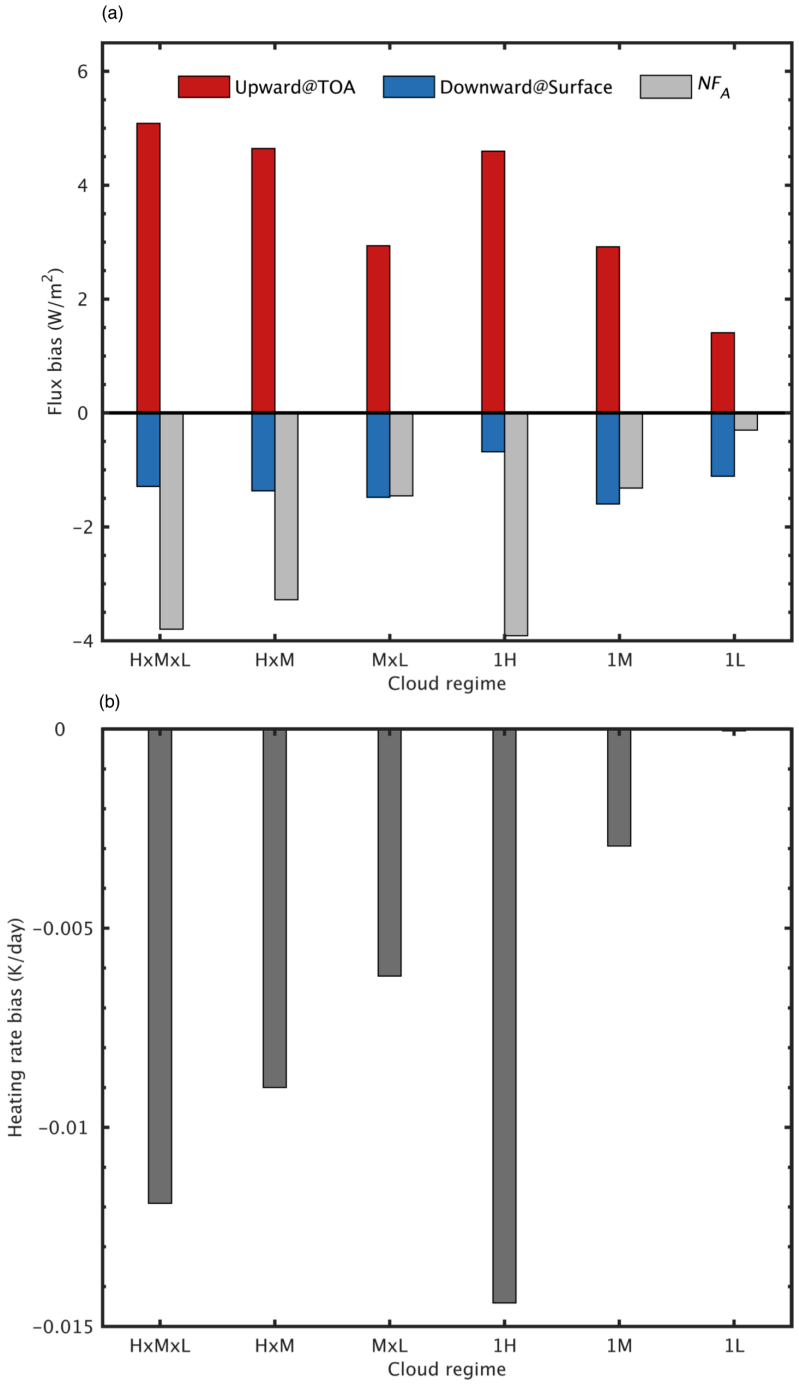

Figure 2.10 Annual global mean biases for 6 cloud regimes in 2010 of (a) upward flux at the TOA (red), downward flux at the surface (blue), and net flux into the atmosphere (grey), and (b) mean heating rate through the whole atmosphere column. 1H, 1M, and 1L indicate single-layer high, middle, and low cloud, respectively. HxMxL, HxM, and MxL mean cloud layers are continuous from high to low, high to middle, and middle to low regions, respectively.

2.5 Conclusions

To reduce the computational burden, an absorption approximation without considering scattering is a widely used method to deal with LW radiative transfer by clouds in GCMs and numerical weather prediction models. This study quantifies the flux and heating rate simulation biases caused by neglecting LW scattering.

We first evaluate flux biases under standard atmospheric conditions in idealized sensitivity tests. In general, upward flux biases at the TOA are larger for high ice clouds, and when optical thickness is less than 5, downward flux biases at the surface for low water clouds are significant. Neglecting LW scattering, OLR can be overestimated by 15 W/m^2, and downward fluxes at the surface can be underestimated by 3 W/m^2. Heating rate biases for ice clouds with 20 μm D_e at the tropopause and the surface are about 7-16% and 2%, respectively, and for water clouds with the same particle size the biases are about 5-7% and 2-7% at the tropopause and the surface, respectively, when cloud optical thickness ranges from small to large values. Chou et al. (1999), Joseph and Min (2003), and Costa and Shine (2006) also show similar results, although their microphysical and optical properties of clouds differ from this study.

To estimate the global average bias, we simulate global fluxes and heating rates in 2010 based on the CCCM merged satellite product. The previous study by Costa and Shine (2006) assumed a constant cloud physical thickness as a function of the cloud top height. Since the CCCM product contains cloud top and base heights from CALIPSO and CloudSat observations (Kato et al., 2014), the cloud thickness is adjusted based on the satellite observations. Because ice clouds are most abundant over the ITCZ,

significant overestimation of TOA upward flux (~12 W/m^2) can occur by neglecting scattering, especially in the Pacific warm pool. However, surface downward flux biases are largest mainly in midlatitude, polar, and mountain areas, with regional peak underestimation by neglecting scattering about 3.6 W/m^2 in Tibetan Plateau, Antarctic, and Greenland areas.

In the temporal domain, the locations of extreme zonally averaged biases vary with the ITCZ over 12 months. The peak value shifts from the southern to the northern hemisphere from January to June and then shifts back to southern hemisphere from July to December. As a global average, when neglecting LW scattering in clouds, OLR is overestimated by 2.6 W/m^2, and downward flux at the surface is underestimated by 1.2 W/m^2. Therefore, when we include the scattering effect of clouds in simulations based on the atmosphere and cloud conditions in a specific moment of a satellite observation, 1.4 W/m^2 is retained in the atmosphere. The TOA upward and surface downward flux biases are about 10% and 5%, respectively, of the global LW cloud radiative effect, which are approximately 27.2 W/m^2 at the TOA and 25.6 W/m^2 at the surface (Henderson et al., 2013). Although compared to global annual averaged OLR about 233.8 W/m^2 (Henderson et al., 2013), the flux bias of 2.6 W/m^2 at the TOA is not large, the regional biases are more significant, up to 9 to 12 W/m^2 at the TOA over the ITCZ, or about 5% of global averaged OLR at most. By neglecting scattering, annual tropopause heating rate biases are about 0.018 K/day, which is -3% of the annually averaged heating rate at that level, and annual heating rate biases at the surface are approximately -0.028 K/day or 2.3% of the surface annual mean heating rate. After

comparing with flux and heating rate simulations, we find that the influence of doubling CO_2 (Clough & Iacono, 1995) and LW scattering are similar. Consequently, scattering in the LW spectrum is important and has to be considered in model simulations.

Due to distinct optical properties of clouds in the RRTMG_LW 16 spectral bands, ice clouds have larger flux biases than water clouds in 10-820 cm^{-1}. The biases of TOA upward flux and surface downward flux are similar in 700-1390 cm^{-1}, because they are in the atmospheric window region. Overall, nearly all of the flux biases are in far-infrared and the atmospheric window regions (10-1390 cm^{-1}). Among them, the upward flux bias at the TOA for ice clouds in band 2 (350-500 cm^{-1}) is largest, contributing over 40% of the total ice cloud bias, because there is a local minimum near 430 cm^{-1} in the imaginary part of the ice refractive index.

Generally, biases are larger for ice clouds than water clouds, and are larger for higher and thicker clouds. For ice clouds, the annual mean TOA upward flux bias and the annual mean surface downward flux bias are about 4.4 and -1.3 W/m^2, respectively, and for water clouds are about 1.6 and -1.1 W/m^2, respectively. The thickest high-top clouds (denoted HxMxL and HxM) have the largest biases, where OLR can be overestimated by up to 5 W/m^2 and downward flux at the surface can be underestimated by up to 1.4 W/m^2.

In conclusion, when LW scattering is neglected, an annual global averaged overestimation of 2.6 W/m^2 in OLR in this study is between 3 W/m^2 estimated by Costa and Shine (2006) and 1.5 W/m^2 by Schmidt et al. (2006), and is much less than 8 W/m^2 by Stephens et al. (2001). The present study uses rigorous radiative transfer calculations

in flux and heating rate simulations, including the advanced MC6 cloud optics models, high spatial resolution CCCM merged satellite products, and observed physical cloud thicknesses. Consequently, global and regional circulation models have to take LW scattering of clouds into account to simulate realistic radiation fields, especially in the far-infrared spectral region with ice clouds.

References

Anderson, G. P., Clough, S. A., Kneizys, F. X., Chetwynd, J. H., & Shettle, E. P. (1986). AFGL atmospheric constituent profiles (0.120 km) (No. AFGL-TR-86-0110). Air Force Geophysics Lab, Hanscom, AFB, MA. Retrieved from http://www.dtic.mil/docs/citations/ADA175173

Baran, A. J. (2012). From the single-scattering properties of ice crystals to climate prediction: A way forward. *Atmospheric Research*, *112*, 45–69. https://doi.org/10.1016/j.atmosres.2012.04.010

Baum, B. A., Heymsfield, A. J., Yang, P., & Bedka, S. T. (2005a). Bulk scattering properties for the remote sensing of ice clouds. Part I: Microphysical data and models. *Journal of Applied Meteorology*, *44*(12), 1885–1895. https://doi.org/10.1175/JAM2308.1

Baum, B. A., Yang, P., Heymsfield, A. J., Platnick, S., King, M. D., Hu, Y.-X., & Bedka, S. T. (2005b). Bulk scattering properties for the remote sensing of ice clouds. Part II: Narrowband models. *Journal of Applied Meteorology*, *44*(12), 1896–1911. https://doi.org/10.1175/JAM2309.1

Baum, B. A., Yang, P., Heymsfield, A. J., Schmitt, C. G., Xie, Y., Bansemer, A., … Zhang, Z. (2011). Improvements in shortwave bulk scattering and absorption models for the remote sensing of ice clouds. *Journal of Applied Meteorology and Climatology*, *50*(5), 1037–1056. https://doi.org/10.1175/2010JAMC2608.1

Baum, B. A., Yang, P., Heymsfield, A. J., Bansemer, A., Cole, B. H., Merrelli, A., … Wang, C. (2014). Ice cloud single-scattering property models with the full phase matrix at wavelengths from 0.2 to 100 μm. *Journal of Quantitative Spectroscopy and Radiative Transfer*, *146*, 123–139. https://doi.org/10.1016/j.jqsrt.2014.02.029

Bi, L., Yang, P., Kattawar, G. W., Baum, B. A., Hu, Y. X., Winker, D. M., … Lu, J. Q. (2009). Simulation of the color ratio associated with the backscattering of radiation by ice particles at the wavelengths of 0.532 and 1.064 μm. *Journal of*

Geophysical Research, *114*(D4), D00H08. https://doi.org/10.1029/2009JD011759

Bi, L., & Yang, P. (2017). Improved ice particle optical property simulations in the ultraviolet to far-infrared regime. *Journal of Quantitative Spectroscopy and Radiative Transfer*, *189*, 228–237. https://doi.org/10.1016/j.jqsrt.2016.12.007

Bohren, C. F., & Huffman, D. R. (1998). *Absorption and Scattering of Light by Small Particles*. New York: Wiley. https://doi.org/10.1002/9783527618156

Chen, X.H., Huang, X.L., & Flanner, M. G. (2014). Sensitivity of modeled far-IR radiation budgets in polar continents to treatments of snow surface and ice cloud radiative properties. *Geophysical Research Letters*, *41*(18), 799–804. https://doi.org/10.1002/2014GL061216

Clough, S. A., Iacono, M. J., & Moncet, J. (1992). Line-by-line calculations of atmospheric fluxes and cooling rates: Application to water vapor. *Journal of Geophysical Research*, *97*(D14), 15761–15785. https://doi.org/10.1029/92JD01419

Clough, S. A., & Iacono, M. J. (1995). Line-by-line calculation of atmospheric fluxes and cooling rates: 2. Application to carbon dioxide, ozone, methane, nitrous oxide and the halocarbons. *Journal of Geophysical Research*, *100*(D8), 16519–16535. https://doi.org/10.1029/95JD01386

Clough, S. A., Shephard, M. W., Mlawer, E. J., Delamere, J. S., Iacono, M. J., Cady-Pereira, K., … Brown, P. D. (2005). Atmospheric radiative transfer modeling: A summary of the AER codes. *Journal of Quantitative Spectroscopy and Radiative Transfer*, *91*(2), 233–244. https://doi.org/10.1016/j.jqsrt.2004.05.058

Cole, B. H., Yang, P., Baum, B. A., Riedi, J., C.-Labonnote, L., Thieuleux, F., & Platnick, S. (2013). Comparison of PARASOL observations with polarized reflectances simulated using different ice habit mixtures. *Journal of Applied Meteorology and Climatology*, *52*(1), 186–196. https://doi.org/10.1175/JAMC-D-12-097.1

Costa, S. M. S., & Shine, K. P. (2006). An estimate of the global impact of multiple scattering by clouds on outgoing long-wave radiation. *Quarterly Journal of the Royal Meteorological Society*, *132*(616), 885–895. https://doi.org/10.1256/qj.05.169

Ding, J., Yang, P., Holz, R. E., Platnick, S., Meyer, K. G., Vaughan, M. A., … King, M. D. (2016). Ice cloud backscatter study and comparison with CALIPSO and MODIS satellite data. *Optics Express*, *24*(1), 620–636. https://doi.org/10.1364/OE.24.000620

Downing, H. D., & Williams, D. (1975). Optical constants of water in the infrared. *Journal of Geophysical Research*, *80*(12), 1656–1661. https://doi.org/10.1029/JC080i012p01656

Edwards, J. M., & Slingo, A. (1996). Studies with a flexible new radiation code. I: Choosing a configuration for a large-scale model. *Quarterly Journal of the Royal Meteorological Society*, *122*(531), 689–719. https://doi.org/10.1002/qj.49712253107

Foot, J. S. (1988). Some observations of the optical properties of clouds. II: Cirrus. *Quarterly Journal of the Royal Meteorological Society*, *114*(479), 145–164. https://doi.org/10.1002/qj.49711447908

Fu, Q., Yang, P., & Sun, W. B. (1998). An accurate parameterization of the infrared radiative properties of cirrus clouds for climate models. *Journal of Climate*, *11*(9), 2223–2237. https://doi.org/10.1175/1520-0442(1998)011<2223:AAPOTI>2.0.CO;2

Hale, G. M., & Querry, M. R. (1973). Optical constants of water in the 200-nm to 200-μm wavelength region. *Applied Optics*, *12*(3), 555–563. https://doi.org/10.1364/AO.12.000555

Hansen, J. E., & Travis, L. D. (1974). Light scattering in planetary atmospheres. *Space Science Reviews*, *16*(4), 527–610. https://doi.org/10.1007/BF00168069

Hansen, J., Sato, M., & Ruedy, R. (1997). Radiative forcing and climate response. *Journal of Geophysical Research: Atmospheres*, *102*(D6), 6831–6864. https://doi.org/10.1029/96JD03436

Hartmann, D. L., Ockert-Bell, M. E., & Michelsen, M. L. (1992). The effect of cloud type on Earth's energy balance: Global analysis. *Journal of Climate*, *5*(11), 1281–1304. https://doi.org/10.1175/1520-0442(1992)005<1281:TEOCTO>2.0.CO;2

Henderson, D. S., L'Ecuyer, T., Stephens, G., Partain, P., & Sekiguchi, M. (2013). A multisensor perspective on the radiative impacts of clouds and aerosols. *Journal of Applied Meteorology and Climatology*, *52*(4), 853–871. https://doi.org/10.1175/JAMC-D-12-025.1

Hioki, S., Yang, P., Baum, B. A., Platnick, S., Meyer, K. G., King, M. D., & Riedi, J. (2016a). Degree of ice particle surface roughness inferred from polarimetric observations. *Atmospheric Chemistry and Physics*, *16*(12), 7545–7558. https://doi.org/10.5194/acp-16-7545-2016

Hioki, S., Yang, P., Kattawar, G. W., & Hu, Y. (2016b). Truncation of the scattering phase matrix for vector radiative transfer simulation. *Journal of Quantitative Spectroscopy and Radiative Transfer*, *183*, 70–77. https://doi.org/10.1016/j.jqsrt.2016.06.011

Holz, R. E., Platnick, S., Meyer, K., Vaughan, M., Heidinger, A., Yang, P., … Wang, C. (2016). Resolving ice cloud optical thickness biases between CALIOP and MODIS using infrared retrievals. *Atmospheric Chemistry and Physics*, *16*(8), 5075–5090. https://doi.org/10.5194/acp-16-5075-2016

Hong, G., Yang, P., Baum, B. A., Heymsfield, A. J., & Xu, K.-M. (2009). Parameterization of shortwave and longwave radiative properties of ice clouds for use in climate models. *Journal of Climate*, *22*(23), 6287–6312. https://doi.org/10.1175/2009JCLI2844.1

Iacono, M. J., Mlawer, E. J., Clough, S. A., & Morcrette, J.-J. (2000). Impact of an improved longwave radiation model, RRTM, on the energy budget and thermodynamic properties of the NCAR community climate model, CCM3. *Journal of Geophysical Research: Atmospheres*, *105*(D11), 14873–14890. https://doi.org/10.1029/2000JD900091

Iacono, M. J., Delamere, J. S., Mlawer, E. J., Shephard, M. W., Clough, S. A., & Collins, W. D. (2008). Radiative forcing by long-lived greenhouse gases: Calculations with the AER radiative transfer models. *Journal of Geophysical Research: Atmospheres*, *113*(13), 2–9. https://doi.org/10.1029/2008JD009944

IPCC (2014). *Climate Change 2013: The Physical Science Basis. Contribution of Working Group I to the Fifth Assessment Report of the Intergovernmental Panel on Climate Change*. (T. F. Stocker, D. Qin, G.-K. Plattner, M. Tignor, S. K. Allen, J. Boschung, … P. M. Midgley, Eds.). Cambridge, NY: Cambridge University Press. https://doi.org/10.1017/CBO9781107415324

Joseph, E., & Min, Q. (2003). Assessment of multiple scattering and horizontal inhomogeneity in IR radiative transfer calculations of observed thin cirrus clouds. *Journal of Geophysical Research: Atmospheres*, *108*(D13), 4380. https://doi.org/10.1029/2002JD002831

Kato, S., Sun-Mack, S., Miller, W. F., Rose, F. G., Chen, Y., Minnis, P., & Wielicki, B. A. (2010). Relationships among cloud occurrence frequency, overlap, and effective thickness derived from CALIPSO and CloudSat merged cloud vertical profiles. *Journal of Geophysical Research*, *115*(D4), D00H28. https://doi.org/10.1029/2009JD012277

Kato, S., Rose, F. G., Sun-Mack, S., Miller, W. F., Chen, Y., Rutan, D. A., … Collins, W. D. (2011). Improvements of top-of-atmosphere and surface irradiance

computations with CALIPSO-, CloudSat-, and MODIS-derived cloud and aerosol properties. *Journal of Geophysical Research*, *116*(D19), D19209. https://doi.org/10.1029/2011JD016050

Kato, S., Miller, W. F., Sun-Mack, S., Rose, F. G., Chen, Y., & Mlynczak, P. E. (2014). Variable descriptions of the A-train integrated CALIPSO, CloudSat, CERES, and MODIS merged product (CCCM or C3M), Version RelB1.v2. Retrieved from https://eosweb.larc.nasa.gov/project/ceres/readme/c3m_variables_B1_v2.pdf

King, M. D., Platnick, S., Menzel, W. P., Ackerman, S. A., & Hubanks, P. A. (2013). Spatial and temporal distribution of clouds observed by MODIS onboard the Terra and Aqua satellites. *IEEE Transactions on Geoscience and Remote Sensing*, *51*(7), 3826–3852. https://doi.org/10.1109/TGRS.2012.2227333

Lacis, A. A., & Oinas, V. (1991). A description of the correlated k distribution method for modeling nongray gaseous absorption, thermal emission, and multiple scattering in vertically inhomogeneous atmospheres. *Journal of Geophysical Research*, *96*(D5), 9027–9063. https://doi.org/10.1029/90JD01945

Liou, K.-N. (1986). Influence of cirrus clouds on weather and climate processes: A global perspective. *Monthly Weather Review*, *114*(6), 1167–1199. https://doi.org/10.1175/1520-0493(1986)114<1167:IOCCOW>2.0.CO;2

Liou, K.-N. (2002). *An Introduction to Atmospheric Radiation* (2nd ed.). Amsterdam, the Netherlands: Academic Press.

Mlawer, E. J., Taubman, S. J., Brown, P. D., Iacono, M. J., & Clough, S. A. (1997). Radiative transfer for inhomogeneous atmospheres: RRTM, a validated correlated-k model for the longwave. *Journal of Geophysical Research*, *102*(D14), 16663–16682. https://doi.org/10.1029/97JD00237

Palmer, K. F., & Williams, D. (1974). Optical properties of water in the near infrared. *Journal of the Optical Society of America*, *64*(8), 1107–1110. https://doi.org/10.1364/JOSA.64.001107

Platnick, S., King, M. D., Meyer, K. G., Wind, G., Amarasinghe, N., Marchant, B., … Riedi, J. (2015). MODIS cloud optical properties: User guide for the Collection 6 Level-2 MOD06/MYD06 product and associated Level-3 Datasets, Version 1.0. Retrieved from http://modis-atmos.gsfc.nasa.gov/_docs/C6MOD06OPUserGuide.pdf

Platnick, S., Meyer, K. G., King, M. D., Wind, G., Amarasinghe, N., Marchant, B., … Riedi, J. (2017). The MODIS cloud optical and microphysical products: Collection 6 updates and examples from Terra and Aqua. *IEEE Transactions on*

Geoscience and Remote Sensing, *55*(1), 502–525. https://doi.org/10.1109/TGRS.2016.2610522

Reichler, T., Dameris, M., & Sausen, R. (2003). Determining the tropopause height from gridded data. *Geophysical Research Letters*, *30*(20). https://doi.org/10.1029/2003GL018240

Rossow, W. B., & Schiffer, R. A. (1991). ISCCP cloud data products. *Bulletin of the American Meteorological Society*, *72*(1), 2–20. https://doi.org/10.1175/1520-0477(1991)072<0002:ICDP>2.0.CO;2

Schmidt, G. A., Ruedy, R., Hansen, J. E., Aleinov, I., Bell, N., Bauer, M., … Yao, M.-S. (2006). Present-day atmospheric simulations using GISS ModelE: Comparison to in situ, satellite, and reanalysis data. *Journal of Climate*, *19*(2), 153–192. https://doi.org/10.1175/JCLI3612.1

Stamnes, K., Tsay, S.-C., Wiscombe, W., & Jayaweera, K. (1988). Numerically stable algorithm for discrete-ordinate-method radiative transfer in multiple scattering and emitting layered media. *Applied Optics*, *27*(12), 2502–2509. https://doi.org/10.1364/AO.27.002502

Stephens, G. L., Tsay, S.-C., Stackhouse, P. W., & Flatau, P. J. (1990). The relevance of the microphysical and radiative properties of cirrus clouds to climate and climatic feedback. *Journal of the Atmospheric Science*s, *47*(14), 1742–1754. https://doi.org/10.1175/1520-0469(1990)047<1742:TROTMA>2.0.CO;2

Stephens, G. L., Gabriel, P. M., & Partain, P. T. (2001). Parameterization of atmospheric radiative transfer. Part I: Validity of simple models. *Journal of the Atmospheric Sciences*, *58*(22), 3391–3409. https://doi.org/10.1175/1520-0469(2001)058<3391:POARTP>2.0.CO;2

Stephens, G. L. (2005). Cloud feedbacks in the climate system: A critical review. *Journal of Climate*, *18*(2), 237–273. https://doi.org/10.1175/JCLI-3243.1

Tselioudis, G., Rossow, W., Zhang, Y., & Konsta, D. (2013). Global weather states and their properties from passive and active satellite cloud retrievals. *Journal of Climate*, *26*(19), 7734–7746. https://doi.org/10.1175/JCLI-D-13-00024.1

Ulanowski, Z., Hesse, E., Kaye, P. H., & Baran, A. J. (2006). Light scattering by complex ice-analogue crystals. *Journal of Quantitative Spectroscopy and Radiative Transfer*, *100*(1–3), 382–392. https://doi.org/10.1016/j.jqsrt.2005.11.052

Ulanowski, Z., Hirst, E., Kaye, P. H., & Greenaway, R. (2012). Retrieving the size of particles with rough and complex surfaces from two-dimensional scattering

patterns. *Journal of Quantitative Spectroscopy and Radiative Transfer*, *113*(18), 2457–2464. https://doi.org/10.1016/j.jqsrt.2012.06.019

van de Hulst, H. C. (1957). *Light Scattering by Small Particles*. New York: Wiley.

van de Hulst, H. C. (1974). The spherical albedo of a planet covered with a homogeneous cloud layer. *Astronomy and Astrophysics*, *35*(2), 209–214.

Warren, S. G., & Brandt, R. E. (2008). Optical constants of ice from the ultraviolet to the microwave: A revised compilation. *Journal of Geophysical Research: Atmospheres*, *113*(14), 1–10. https://doi.org/10.1029/2007JD009744

Wiscombe, W. J. (1977). The delta–M method: Rapid yet accurate radiative flux calculations for strongly asymmetric phase functions. *Journal of the Atmospheric Sciences*, *34*(9), 1408–1422. https://doi.org/10.1175/1520-0469(1977)034<1408:TDMRYA>2.0.CO;2

Yang, P., Kattawar, G. W., Hong, G., Minnis, P., & Hu, Y. (2008a). Uncertainties associated with the surface texture of ice particles in satellite-based retrieval of cirrus clouds—Part I: Single-scattering properties of ice crystals with surface roughness. *IEEE Transactions on Geoscience and Remote Sensing*, *46*(7), 1940–1947. https://doi.org/10.1109/TGRS.2008.916471

Yang, P., Hong, G., Kattawar, G. W., Minnis, P., & Hu, Y. (2008b). Uncertainties associated with the surface texture of ice particles in satellite-based retrieval of cirrus clouds: Part II—Effect of particle surface roughness on retrieved cloud optical thickness and effective particle size. *IEEE Transactions on Geoscience and Remote Sensing*, *46*(7), 1948–1957. https://doi.org/10.1109/TGRS.2008.916472

Yang, P., Bi, L., Baum, B. A., Liou, K.-N., Kattawar, G. W., Mishchenko, M. I., & Cole, B. (2013). Spectrally consistent scattering, absorption, and polarization properties of atmospheric ice crystals at wavelengths from 0.2 to 100 μm. *Journal of the Atmospheric Sciences*, *70*(1), 330–347. https://doi.org/10.1175/JAS-D-12-039.1

Yang, P., Liou, K., Bi, L., Liu, C., Yi, B., & Baum, B. A. (2015). On the radiative properties of ice clouds: Light scattering, remote sensing, and radiation parameterization. *Advances in Atmospheric Sciences*, *32*(1), 32–63. https://doi.org/10.1007/s00376-014-0011-z

Yi, B., Yang, P., Baum, B. A., L'Ecuyer, T., Oreopoulos, L., Mlawer, E. J., … Liou, K.-N. (2013). Influence of ice particle surface roughening on the global cloud radiative effect. *Journal of the Atmospheric Sciences*, *70*(9), 2794–2807. https://doi.org/10.1175/JAS-D-13-020.1

Zhang, Y.-C., Rossow, W. B., & Lacis, A. A. (1995). Calculation of surface and top of atmosphere radiative fluxes from physical quantities based on ISCCP data sets: 1. Method and sensitivity to input data uncertainties. *Journal of Geophysical Research: Atmospheres*, *100*(D1), 1149–1165. https://doi.org/10.1029/94JD02747

3. PARAMETERIZATIONS OF ICE CLOUD BULK SINGLE-SCATTERING PROPERTIES AND INHERENT UNCERTAINTIES IN THE RADIATIVE TRANSFER MODELS IN THE LONGWAVE SPECTRUM

3.1 Introduction

When investigating the global energy budget, the treatment of radiative properties of clouds is an important issue, since clouds significantly affect the energy distribution in the atmospheric system (Liou, 2002). Especially, due to the complex shapes of ice crystals, ice clouds have very distinct radiative properties that cause a highly variable greenhouse effect (Allan, 2011; Ebert & Curry, 1992).

In the longwave spectral bands, since gas absorption dominates over longwave light scattering, early studies (Curry & Herman, 1985; Ebert & Curry, 1992; Stephens, 1984) only used absorption properties of ice clouds in numerical experiments to reduce computational cost. At that time, people found that the absorption coefficient of ice clouds is very well approximated as a function of cloud particle size. As computing power has grown, it has become desirable to use the full optical properties of ice clouds (extinction coefficient, single-scattering albedo, and asymmetry factor) in recent model simulations to include the influence of light scattering. For example, Edwards et al. (2007), Fu et al. (1998), Hong et al. (2009) and Yi et al. (2013) investigated the radiative effect of ice clouds by using the extinction coefficient, single-scattering albedo, and asymmetry factor of ice clouds, which were parameterized by the effective size of cloud

particles. Furthermore, Fu (1996) gave physical explanations of parameterizations of ice cloud single-scattering properties in terms of cloud particle size.

Limited aircraft observations show that ice cloud particles have very complex crystal shapes (Baran, 2009, 2012; Baum et al., 2011), and it is important to have realistic particle shapes to compute correct ice cloud optical properties. Due to the difficulty of deriving the optical properties of non-spherical ice crystals, in early parameterizations (Ebert & Curry, 1992; Fu et al., 1996, 1998), the ice crystal shapes were usually assumed to be simple hexagonal columns. With improvements in calculating scattering properties of ice particles (Yang et al., 2013, 2015), Edwards et al. (2007), Hong et al. (2009) and Yi et al. (2013) proposed ice cloud parameterization schemes based on ice aggregates, a mixture of 6 ice crystal shapes, and a general habit mixture of 9 shapes, respectively. Currently, the MODIS science team (Platnick et al., 2015, 2017) uses an ice cloud model, called MODIS Collection 6 (MC6), which is composed of aggregates of 8 severely roughened hexagonal columns, to improve ice cloud property retrievals in MODIS Collection 6 cloud retrieval products.

Besides issues concerning parameterization techniques and ice crystal shapes, the following radiative transfer calculations also contain several additional difficulties. In large-scale climate simulations, fast and accurate radiative transfer models (RTMs) are needed to reduce computational costs. Several studies (e.g., Fu et al., 1997; Liou, 2002; Meador & Weaver, 1980; O'Brien et al., 1997; Toon et al., 1989; Zdunkowski et al., 1982) have evaluated the accuracy and efficiency of various RTMs. Here, since evaluation results depend on specific radiative properties of ice clouds, the

parameterizations of the MC6 ice cloud model, described in section 3.2, are used in evaluating the performance of RTMs. The theories of approximations of longwave radiative transfer are introduced in section 3.3. The evaluations of RTMs are discussed in section 3.4, and conclusions are given in section 3.5.

3.2 Parameterizations of band-averaged bulk ice cloud optical properties

This study uses the MC6 ice cloud model (Platnick et al., 2015, 2017), which describes ice cloud particles as severely roughened aggregates of 8 hexagonal columns. The single scattering properties of the ice cloud model are provided by the optical property library (Yang et al., 2013), which uses the refractive index of ice from Warren and Brandt (2008) and improves forward scattering by removing delta-transmission terms in ray-tracing processes (Bi et al., 2009). The dataset in this study includes in-situ observations from 11 field campaigns listed in Table 3.1 (Baum et al., 2011; Heymsfield et al., 2010, 2013) with a total of 14,406 particle size distributions (PSDs) of ice clouds (downloaded from http://www.ssec.wisc.edu/ice_models/microphysical_data.html). Only PSDs with observed cloud temperatures less than -40°C are included and the PSDs have been processed to minimize the influence of ice shattering issues when measuring ice particle sizes (Baum et al., 2011; Heymsfield et al., 2013). In the dataset, PSDs are fitted to the following gamma distribution (Baum et al., 2005a; Heymsfield et al., 2013; Kosarev & Mazin, 1991; Mitchell, 1991; Wendisch & Yang, 2012):

$$N(D) = N_0 D^{\upsilon} e^{-\lambda^* D}, \tag{3.1}$$

where D is the particle maximum dimension (cm), N is the particle number concentration between particle maximum dimension D and $D + \Delta D$ (cm^{-3} cm^{-1}), N_0 is the intercept, υ is the dispersion and λ^* is the slope (cm^{-1}).

Table 3.1 Field campaigns and corresponding number of PSDs.

Field Campaign	Year	Number of PSDs	Field Campaign	Year	Number of PSDs
TRMM KWAJEX	1999	201	SCOUT	2005	358
ARM-IOP	2000	1420	ACTIVE-Monsoon	2005	4268
CRYSTAL-FACE	2004	221	ACTIVE-Squall Line	2005	740
MidCiX	2004	2968	ACTIVE-Hector	2005	2583
Pre-AVE	2004	99	TC-4	2006	877
MPACE	2004	671			

In practice, GCMs, to increase calculation efficiency, need band-averaged bulk optical properties of ice clouds to perform broadband radiative transfer calculations rapidly, while avoiding sophisticated and time-consuming spectral line-by-line calculations. The ice cloud spectral band bulk optical properties are derived as spectrally weighted optical properties using the Planck function (B) at 233 K for a given PSD (Baum et al., 2005b, 2011, 2014; Fu et al., 1998; Hong et al., 2009; Yi et al., 2013; Wendisch & Yang, 2012), as follows:

$$\bar{\kappa}_{ext} = \frac{\int_{\lambda_1}^{\lambda_2}\int_{D_{min}}^{D_{max}} \sigma_{ext}(D,\lambda)B(\lambda)N(D)dDd\lambda}{\rho_{ice}\int_{\lambda_1}^{\lambda_2}\int_{D_{min}}^{D_{max}} V(D)B(\lambda)N(D)dDd\lambda}, \tag{3.2}$$

$$\bar{\sigma}_{ext/sca} = \frac{\int_{\lambda_1}^{\lambda_2}\int_{D_{min}}^{D_{max}} \sigma_{ext/sca}(D,\lambda)B(\lambda)N(D)dDd\lambda}{\int_{\lambda_1}^{\lambda_2}\int_{D_{min}}^{D_{max}} B(\lambda)N(D)dDd\lambda}, \tag{3.3}$$

$$\bar{g} = \frac{\int_{\lambda_1}^{\lambda_2}\int_{D_{min}}^{D_{max}} g(D,\lambda)\sigma_{sca}(D,\lambda)B(\lambda)N(D)dDd\lambda}{\int_{\lambda_1}^{\lambda_2}\int_{D_{min}}^{D\max} \sigma_{sca}(D,\lambda)B(\lambda)N(D)dDd\lambda}, \text{ and} \tag{3.4}$$

$$\bar{\omega} = \frac{\bar{\sigma}_{sca}}{\bar{\sigma}_{ext}}, \tag{3.5}$$

where λ is the wavelength, ρ_{ice} is the bulk density of ice (0.917 g/cm^3), $\bar{\kappa}_{ext}$, $\bar{\sigma}_{ext/sca}$, $\bar{g}$ and $\bar{\omega}$ are the band-averaged bulk mass extinction coefficient, extinction/scattering cross section, asymmetry factor and single-scattering albedo, $\sigma_{ext/sca}$ and g are the extinction/scattering cross section and the asymmetry factor, λ_2 and λ_1 define the spectral ranges, and D_{max} and D_{min} are the upper and lower limits of particle maximum dimensions for a given PSD. In this study, the 16 spectral bands in the RRTMG_LW program (Clough et al., 2005; Iacono et al., 2008) listed in Table 3.2 are used to define the spectral boundaries. To describe the bulk particle size of a given ice cloud, the effective diameter (D_e) is defined as 1.5 times the ratio of the total volume and the total projected area (Baum et al., 2005a, 2011, 2014; Foot, 1988; Wendisch & Yang, 2012):

$$D_e = \frac{3\int_{D_{min}}^{D_{max}} V(D)N(D)dD}{2\int_{D_{min}}^{D_{max}} A(D)N(D)dD}, \tag{3.6}$$

where V and A are the volume and the projected area for a particle.

Table 3.2 Spectral ranges of 16 RRTMG_LW bands.

Band	Wavenumber (cm^{-1})	Wavelength (μm)	Band	Wavenumber (cm^{-1})	Wavelength (μm)
1	10 - 350	1000.0 - 28.57	9	1180 - 1390	8.47 - 7.19
2	350 - 500	28.57 - 20.00	10	1390 - 1480	7.19 - 6.76
3	500 - 630	20.00 - 15.87	11	1480 - 1800	6.76 - 5.56
4	630 - 700	15.87 - 14.29	12	1800 - 2080	5.56 - 4.81
5	700 - 820	14.29 - 12.20	13	2080 - 2250	4.81 - 4.44
6	820 - 980	12.20 - 10.20	14	2250 - 2380	4.44 - 4.20
7	980 - 1080	10.20 - 9.26	15	2380 - 2600	4.20 - 3.85
8	1080 - 1180	9.26 - 8.47	16	2600 - 3250	3.85 - 3.08

Following previous studies (Fu et al., 1996, 1998; Hong et al., 2009; Yi et al., 2013), to appropriately represent optical properties for both small and large D_e, after testing we parameterize band-averaged bulk optical properties of MC6 ice cloud by a 4th-order polynomial for $D_e \geq 25$ μm and a 8th-order polynomial for $D_e < 25$ μm as a function of D_{inv}, the offset inverse effective diameter, as follows:

$$D_{inv} = \frac{1}{D_e} - \frac{1}{25}, \tag{3.7}$$

$$\bar{\kappa}_{ext} = \begin{cases} \sum_{j=1}^{4} a_j (D_{inv})^{4-j}, \text{ for } D_e \geq 25 \text{ μm} \\ \sum_{j=1}^{8} a_j (D_{inv})^{8-j}, \text{ for } D_e < 25 \text{ μm} \end{cases}, \tag{3.8}$$

$$\bar{\omega} = \begin{cases} \sum_{j=1}^{4} b_j (D_{inv})^{4-j}, \text{ for } D_e \geq 25 \text{ μm} \\ \sum_{j=1}^{8} b_j (D_{inv})^{8-j}, \text{ for } D_e < 25 \text{ μm} \end{cases}, \text{ and} \tag{3.9}$$

$$\bar{g} = \begin{cases} \sum_{j=1}^{4} c_j (D_{inv})^{4-j}, \text{ for } D_e \geq 25 \text{ μm} \\ \sum_{j=1}^{8} c_j (D_{inv})^{8-j}, \text{ for } D_e < 25 \text{ μm} \end{cases}, \tag{3.10}$$

where j is the index of the power of the polynomial, and a_j, b_j, and c_j are polynomial fitting coefficients for $\bar{\kappa}_{ext}$, $\bar{\omega}$ and $\bar{g}$, respectively. Figure 3.1, Figure 3.2 and Figure 3.3 show polynomial fittings of $\bar{\kappa}_{ext}$, $\bar{\omega}$ and $\bar{g}$, respectively, for all RRTMG_LW spectral bands based on PSDs from the 11 field campaigns. The corresponding coefficients of determination (R^2) in Table 3.3 are all greater than 0.9 for both $D_e \geq 25$ μm and $D_e < 25$ μm. As a result, parameterizations of band-averaged bulk optical properties using the MC6 ice cloud model are shown in Figure 3.4.

Table 3.3 R^2 values of fitting MC6 ice cloud band-averaged bulk optical properties in 16 RRTMG_LW bands.

Band	R^2 for $\bar{\kappa}_{ext}$		R^2 for $\bar{\omega}$		R^2 for $\bar{g}$	
	$D_e \geq 25$ μm	$D_e < 25$ μm	$D_e \geq 25$ μm	$D_e < 25$ μm	$D_e \geq 25$ μm	$D_e < 25$ μm
1	0.9902	0.9520	0.9218	0.9984	0.9898	0.9931
2	0.9897	0.9879	0.9864	0.9922	0.9772	0.9876
3	0.9986	0.9915	0.9616	0.9932	0.9495	0.9938
4	0.9992	0.9969	0.9073	0.9958	0.9306	0.9970
5	0.9995	0.9982	0.9649	0.9987	0.9333	0.9982
6	0.9989	0.9988	0.9400	0.9994	0.9637	0.9982
7	0.9966	0.9884	0.9731	0.9957	0.9594	0.9928
8	0.9990	0.9944	0.9679	0.9922	0.9511	0.9915
9	0.9992	0.9966	0.9581	0.9966	0.9438	0.9950
10	0.9983	0.9972	0.9367	0.9967	0.9313	0.9981
11	0.9981	0.9973	0.9283	0.9965	0.9292	0.9984
12	0.9959	0.9969	0.9675	0.9984	0.9568	0.9688
13	0.9983	0.9971	0.9487	0.9977	0.9389	0.9963

Table 3.3 Continued

Band	R^2 for $\bar{\kappa}_{ext}$		R^2 for $\bar{\omega}$		R^2 for $\bar{g}$	
	$D_e \geq 25$ μm	$D_e < 25$ μm	$D_e \geq 25$ μm	$D_e < 25$ μm	$D_e \geq 25$ μm	$D_e < 25$ μm
14	0.9990	0.9973	0.9439	0.9977	0.9323	0.9968
15	0.9998	0.9974	0.9641	0.9984	0.9497	0.9920
16	0.9998	0.9983	0.9708	0.9983	0.9585	0.9927

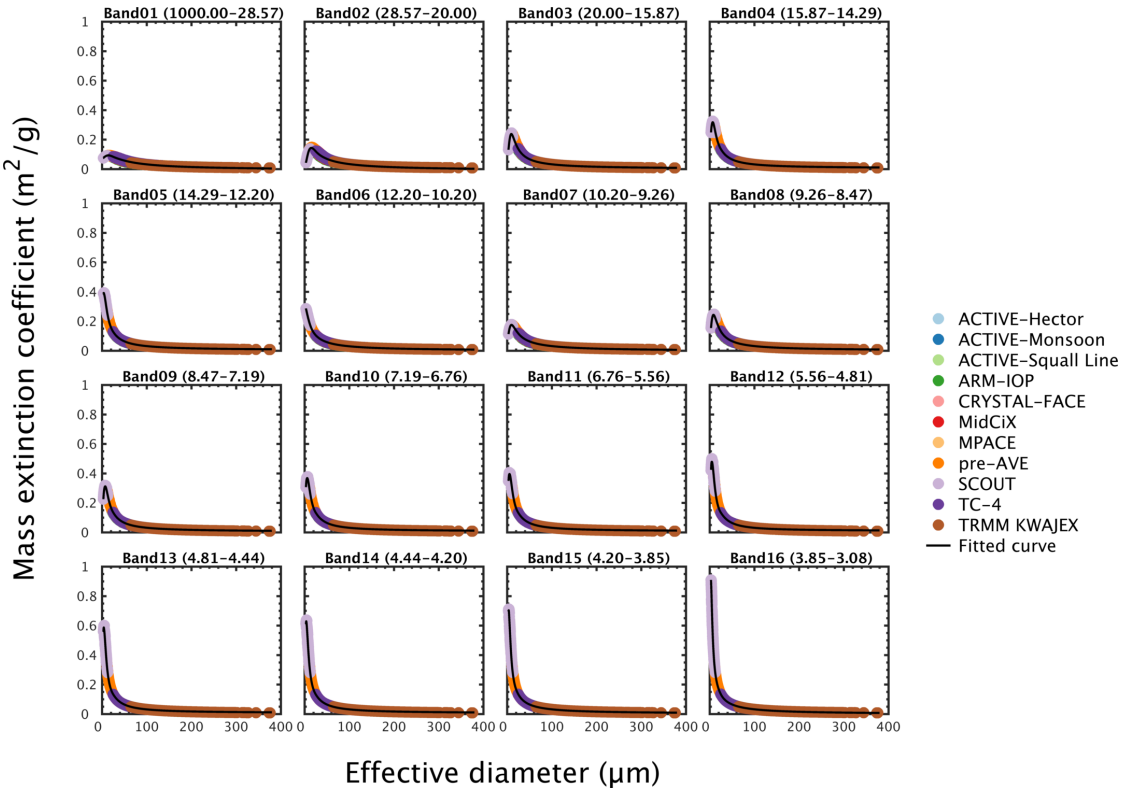

Figure 3.1 Polynomial fittings of band-averaged bulk mass extinction coefficient based on the MC6 ice cloud model for 16 RRTMG_LW bands. Numbers in parentheses are wavelength in ranges μm. Colored circles indicate PSDs used to calculate the band-averaged bulk mass extinction coefficient from 11 field campaigns. Solid lines are fitted curves.

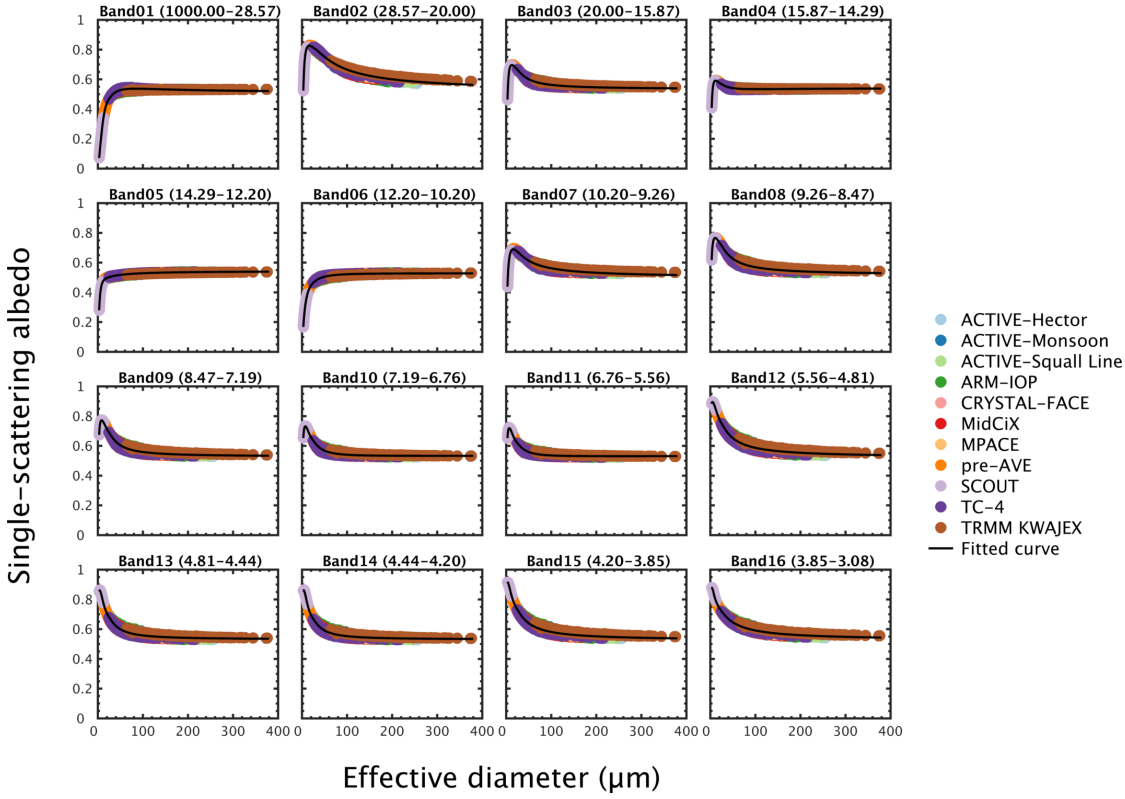

Figure 3.2 As in Figure 3.1, except for single-scattering albedo.

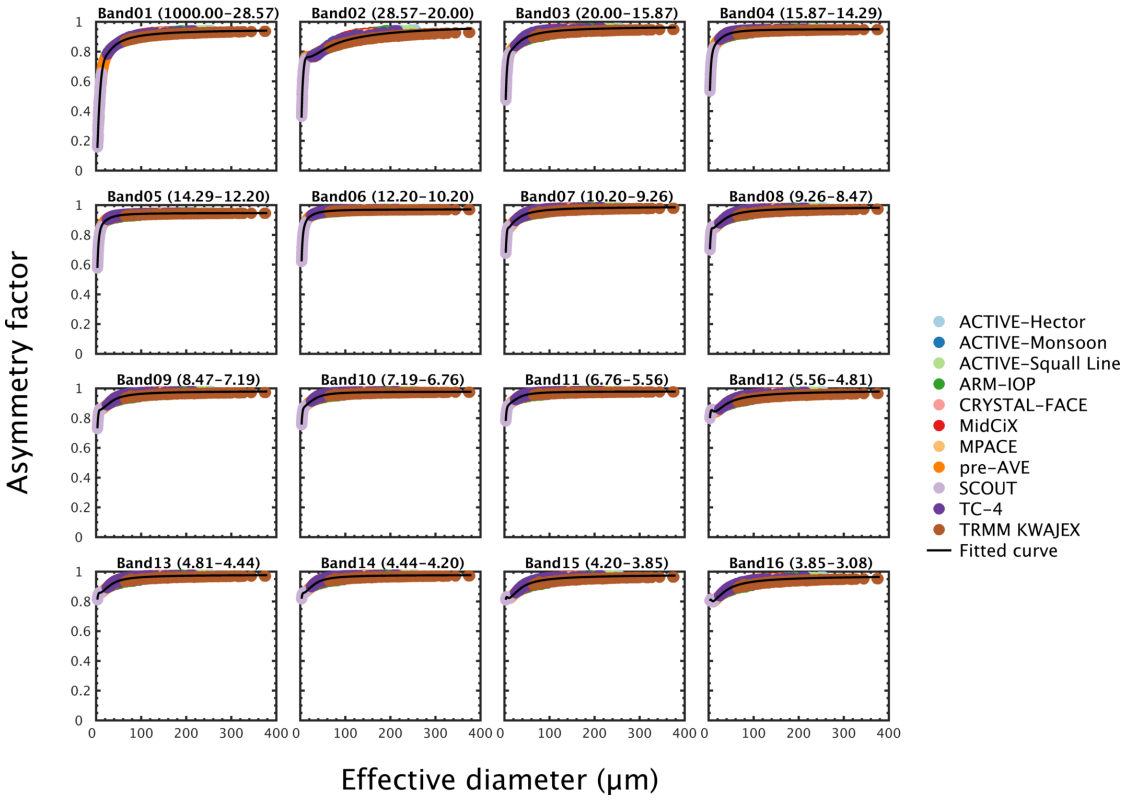

Figure 3.3 As in Figure 3.1, except for asymmetry factor.

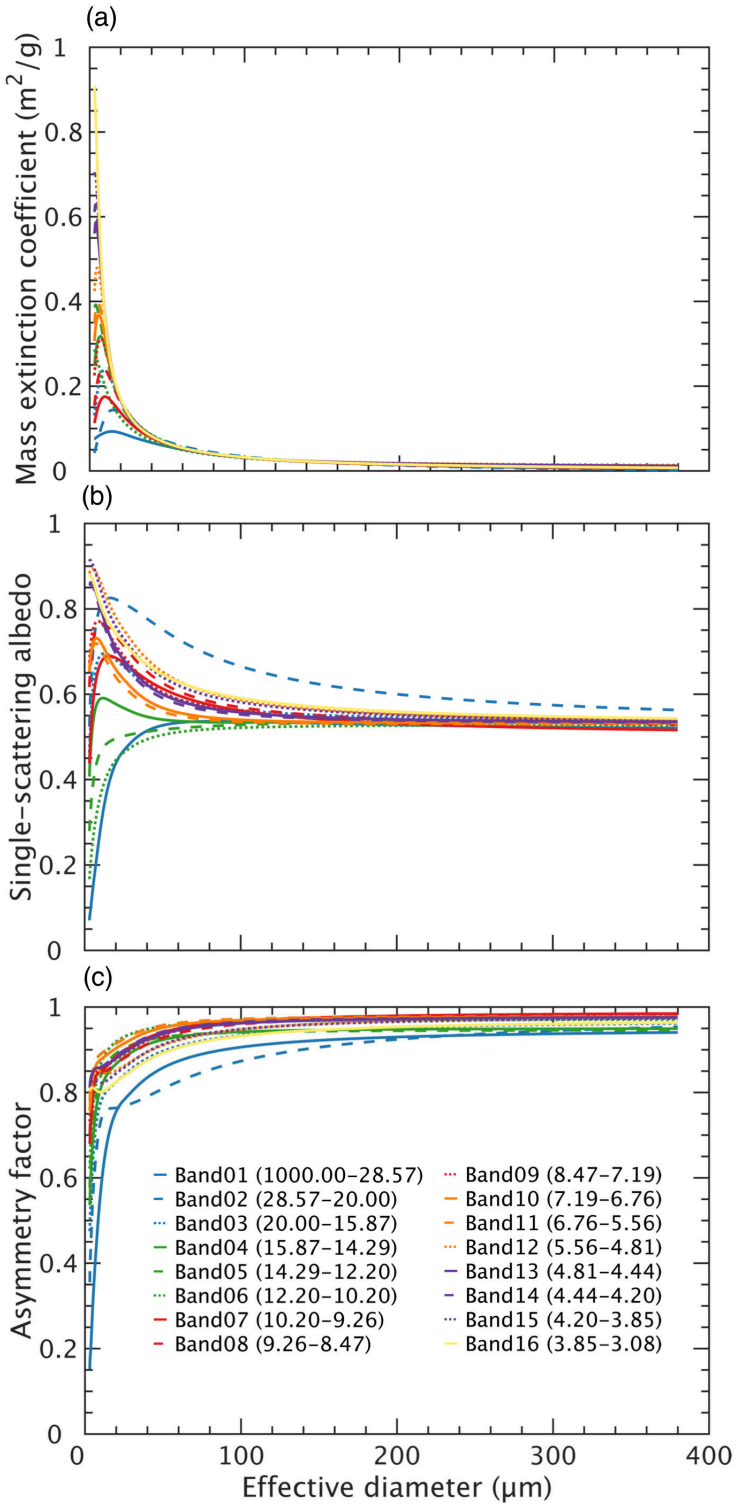

Figure 3.4 Parameterizations of (a) $\bar{\kappa}_{ext}$, (b) $\bar{\omega}$ and (c) $\bar{g}$ in 16 RRTMG_LW bands. Colored lines indicate different RRTMG_LW spectral bands.

3.3 Longwave radiative transfer models

Due to highly anisotropic scattering properties of clouds (Wendisch & Yang, 2012), accurate radiative transfer calculations are computationally expensive, so in practice, GCMs utilize approximation methods to deal with radiative transfer processes. Since there are many radiative transfer approximation methods, the accuracy and efficiency of each method should be assessed for possible effects on the computed climatic influence of longwave scattering caused by ice clouds.

The general form of the longwave radiative transfer equation, governing diffuse intensity (I) at any point in an assumed plane-parallel atmosphere with local thermodynamic equilibrium, may be expressed as follows (Fu et al., 1997; Liou, 2002; Meador & Weaver, 1980; Toon et al., 1989; Wendisch & Yang, 2012):

$$\mu \frac{dI(\tau,\mu,\phi)}{d\tau} = I(\tau,\mu,\phi) - S(\tau,\mu,\phi), \text{ and} \tag{3.11}$$

$$S(\tau,\mu,\phi) = \frac{\omega}{4\pi}\int_0^{2\pi}\int_{-1}^{1} P(\mu,\mu',\phi,\phi')I(\tau,\mu',\phi')d\mu' d\phi' + (1-\omega)B(T), \tag{3.12}$$

where τ is the optical thickness, μ is the cosine of the zenith angle θ, ϕ is the azimuth angle, S is the source function, ω is the single-scattering albedo, P is the phase function, and $B(T)$ is the Planck function at temperature T. In this study, calculations are performed for each of the 16 RRTMG_LW bands. With eqs. 3.11 and 3.12, different approximations of the radiative transfer equation may be derived according to different assumptions of I and P. The following subsections summarize four longwave radiative transfer approximation methods.

3.3.1 2-stream approximation

The "2-stream" approximation expresses the radiative fluxes in all directions around a point in a form where the average upward and downward fluxes (2 streams) can be computed analytically. Combining eqs. 3.11 and 3.12, and integrating over zenith and azimuth directions, the diffuse flux version of the longwave radiative transfer equation is as follows:

$$\begin{aligned}\frac{dF^{\pm}(\tau)}{d\tau} &= \int_0^{2\pi}\int_0^{\pm 1} I(\tau,\mu,\phi)d\mu d\phi \\ &- \int_0^{2\pi}\int_0^{\pm 1}\left[\frac{\omega}{4\pi}\int_0^{2\pi}\int_{-1}^{1} P(\mu,\mu',\phi,\phi')I(\tau,\mu',\phi')d\mu' d\phi'\right] d\mu d\phi, \\ &- \int_0^{2\pi}\int_0^{\pm 1}(1-\omega)B(T)d\mu d\phi\end{aligned} \tag{3.13}$$

where F^+ and F^- are upward $(+)$ and downward $(-)$ flux, respectively, and can be expressed as

$$F^{\pm}(\tau) = \int_0^{2\pi}\int_0^{\pm 1} I(\tau,\mu,\phi)\mu d\mu d\phi. \tag{3.14}$$

In the longwave spectrum, we may assume that flux is independent of the azimuth angle, and eq. 3.13 becomes

$$\begin{aligned}\frac{dF^{\pm}(\tau)}{d\tau} &= 2\pi I^{\pm}(\tau) \\ &-\omega\pi\int_0^{\pm 1}\int_{-1}^{1} P(\mu,\mu')I(\tau,\mu')d\mu'\, d\mu, \\ &\mp 2\pi(1-\omega)B(T)\end{aligned} \tag{3.15}$$

with

$$I^{\pm}(\tau) = \int_0^{\pm 1} I(\tau,\mu)d\mu, \tag{3.16}$$

where I^+ and I^- are the upper and lower hemispheric intensity, respectively. If we assume that the Planck function can be approximated in a function of τ, like $B(\tau)$, eq.

3.15 can be decomposed into coupled differential equations. This means that both upward and downward scattered fluxes contribute upward and downward diffuse fluxes at the same time. This is a general form of the 2-stream approximation (Edwards & Slingo, 1996; Meador & Weaver, 1980; O'Brien et al., 1997):

$$\begin{cases} \frac{dF^{+}(\tau)}{d\tau} = \gamma_1 F^{+}(\tau) - \gamma_2 F^{-}(\tau) - S^{+}(\tau) \\ \frac{dF^{-}(\tau)}{d\tau} = \gamma_2 F^{+}(\tau) - \gamma_1 F^{-}(\tau) + S^{-}(\tau) \end{cases}, \tag{3.17}$$

with

$$\gamma_1 = \widetilde{D}\left[1 - \frac{\omega}{2}(1+\chi)\right], \tag{3.18}$$

$$\gamma_2 = \widetilde{D}\frac{\omega}{2}(1-\chi), \tag{3.19}$$

$$S^{+}(\tau) = S^{-}(\tau) = \widetilde{D}\pi(1-\omega)B(\tau), \tag{3.20}$$

where $\widetilde{D}$ and χ are the diffusivity factor and diffusivity coefficient, respectively, depending on different 2-stream approximations. Table 3.4 lists values of $\widetilde{D}$ and χ for the commonly used 2-stream approximations, including the hemispheric mean (Toon et al., 1989), modified 2-stream approximation (Fu et al., 1997), quadrature method (Liou, 2002), and practical improved flux method (PIFM; Zdunkowski et al., 1982). Furthermore, the diffusivity factor of 1.66 is a commonly accepted value estimated by numerical experiments (Elsasser, 1942; Goody & Yung, 1989; O'Brien et al., 1997).

Table 3.4 Values of the diffusivity factor and diffusivity coefficient of selected 2-stream approximations.

Method	$\widetilde{D}$	χ	Reference
Hemispheric mean (HM)	2	g	Toon et al. (1989)
Modified 2-stream approximation	1.66	g	Fu et al. (1997)
Quadrature method (QM)	$\sqrt{3}$	g	Liou (2002)
PIFM	1.66	$\frac{3g}{2\widetilde{D}}$	Zdunkowski et al. (1982)

The general solution (Toon et al., 1989) of eq. 3.17 can be shown to be

$$\begin{cases} F^+(\tau) = \alpha_1 \exp(\beta\tau) + \alpha_2 \Gamma \exp(-\beta\tau) + Q^+(\tau) \\ F^-(\tau) = \alpha_1 \Gamma \exp(\beta\tau) + \alpha_2 \exp(-\beta\tau) + Q^-(\tau)' \end{cases} \tag{3.21}$$

with

$$\Gamma = \frac{\gamma_2}{\gamma_1+\beta} = \frac{\gamma_1-\beta}{\gamma_2}, \tag{3.22}$$

$$\beta = \sqrt{\gamma_1^2 - \gamma_2^2}, \tag{3.23}$$

where values of α_1 and α_2 are dependent on the boundary conditions, and $Q^{\pm}$ are the particular solutions of eq. 3.17 and are determined by function $S^{\pm}$. To derive the particular solutions, following Toon et al. (1989), we keep the first two terms of the Taylor expansions of the Planck function, and assume the linear form of the Planck function may be appropriately approximated by

$$B(T) \approx B(\tau) = B_0 + B_1\tau, \tag{3.24}$$

$$B_1 = \frac{\partial B(T)}{\partial \tau} \approx \frac{\Delta B(T)}{\Delta \tau} = \frac{B(T_{bot})-B_0}{\tau^*}, \text{ and} \tag{3.25}$$

$$B_0 = B(T_{top}), \tag{3.26}$$

where τ^* is the total optical thickness of a layer, B_0 is the Planck function at the temperature of the top of a layer (T_{top}), and T_{bot} is the temperature of the bottom of a layer. This linear assumption of the Planck function in τ has been evaluated by Wiscombe (1976), who has shown that the maximum percent errors of the approximation increase with increasing wavenumber and temperature gradient, and with decreasing temperature. In addition, other than linearization in τ, the Planck function may be approximated by the exponentials in τ, as in Fu et al. (1997) and Liou (2002). Therefore, with eqs. 3.17-3.20 and 3.24, $Q^{\pm}$ can be solved as follows:

$$\begin{cases} Q^+(\tau) = \widetilde{D}\pi\left(\frac{1-\omega}{\gamma_1-\gamma_2}\right)\left[B_0 + B_1\left(\tau + \frac{1}{\gamma_1-\gamma_2}\right)\right] \\ Q^-(\tau) = \widetilde{D}\pi\left(\frac{1-\omega}{\gamma_1-\gamma_2}\right)\left[B_0 + B_1\left(\tau - \frac{1}{\gamma_1-\gamma_2}\right)\right] \end{cases}. \tag{3.27}$$

For the applications of the 2-stream approximation in the multi-layer atmospheres, Toon et al. (1989) has proposed a numerically stable method, which organizes the equations in 3.21 for each layer to form a tridiagonal matrix. In layer m of a total M layer atmosphere, shown in Figure 3.5, we may assume that each layer of the atmosphere is homogeneous, and can express eqs. 3.21-3.23 as

$$\begin{cases} F_m^+(\tau) = \alpha_{1,m}\exp(\beta_m\tau) + \alpha_{2,m}\Gamma_m\exp(-\beta_m\tau) + Q_m^+(\tau) \\ F_m^-(\tau) = \alpha_{1,m}\Gamma_m\exp(\beta_m\tau) + \alpha_{2,m}\exp(-\beta_m\tau) + Q_m^-(\tau) \end{cases}, \tag{3.28}$$

$$\Gamma_m = \frac{\gamma_{2,m}}{\gamma_{1,m}+\beta_m} = \frac{\gamma_{1,m}-\beta_m}{\gamma_{2,m}}, \text{ and} \tag{3.29}$$

$$\beta_m = \sqrt{\gamma_{1,m}^2 - \gamma_{2,m}^2}. \tag{3.30}$$

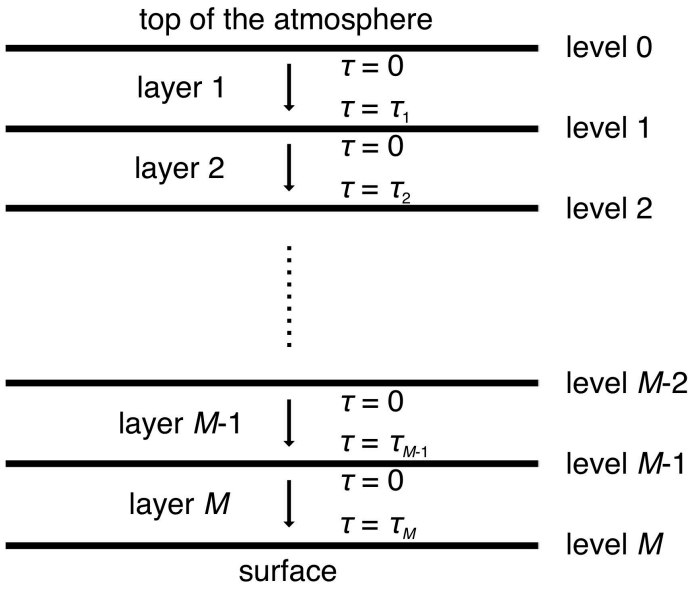

Figure 3.5 Structure of the M layer atmosphere

Since eq. 3.28 contains positive exponents, to avoid numerical instability (Toon et al., 1989), we rewrite eq. 3.28 into

$$\begin{cases} F_m^+(\tau) = Y_{1,m}\left[\exp\left(-\beta_m(\tau_m-\tau)\right) + \Gamma_m \exp(-\beta_m\tau)\right] \\ \qquad\quad +Y_{2,m}\left[\exp\left(-\beta_m(\tau_m-\tau)\right) - \Gamma_m \exp(-\beta_m\tau)\right] \\ \qquad\quad +Q_m^+(\tau) \\ F_m^-(\tau) = Y_{1,m}\left[\Gamma_m \exp\left(-\beta_m(\tau_m-\tau)\right) + \exp(-\beta_m\tau)\right] \\ \qquad\quad +Y_{2,m}\left[\Gamma_m \exp\left(-\beta_m(\tau_m-\tau)\right) - \exp(-\beta_m\tau)\right] \\ \qquad\quad +Q_m^-(\tau) \end{cases}, \tag{3.31}$$

by assuming

$$\begin{cases} Y_{1,m} = \frac{\alpha_{1,m}\exp(\beta_m\tau_m)+\alpha_{2,m}}{2} \\ Y_{2,m} = \frac{\alpha_{1,m}\exp(\beta_m\tau_m)-\alpha_{2,m}}{2} \end{cases}, \tag{3.32}$$

where τ_m is the optical thickness of the layer m. The boundary conditions of the M layer atmosphere are

$$F_1^-(0) = F_0^-(0), \tag{3.33}$$

$$F_M^+(\tau_M) = R_{sfc}F_M^-(\tau_M) + S_{sfc}, \tag{3.34}$$

$$F_m^+(\tau = \tau_m) = F_{m+1}^+(\tau = 0), \text{ and} \tag{3.35}$$

$$F_m^-(\tau = \tau_m) = F_{m+1}^-(\tau = 0), \tag{3.36}$$

where R_{sfc} is the surface reflectivity, and S_{sfc} is a source term provided by the surface, which is a function of the surface temperature (T_{sfc}) and surface emissivity (ε_{sfc}) in the longwave spectrum:

$$S_{sfc} = \varepsilon_{sfc}\pi B(T_{sfc}). \tag{3.37}$$

The boundary condition given by eq. 3.33 means that the downward diffuse flux at the top of the 1st layer equals to any incoming downward diffuse flux, and in the longwave spectrum, the incoming downward diffuse flux may be set to 0. For the second boundary condition (eq. 3.34), the sum of the reflected downward flux and the surface emitted upward flux equals the upward diffuse flux at the bottom of layer M. The last two boundary conditions (eqs. 3.35 and 3.36) state that upward and downward fluxes on the boundaries are continuous.

Following Toon et al. (1989), we may use the following expressions:

$$\begin{cases} e_{1,m} = 1 + \Gamma_m \exp(-\beta_m\tau_m) \\ e_{2,m} = 1 - \Gamma_m \exp(-\beta_m\tau_m) \\ e_{3,m} = \Gamma_m + \exp(-\beta_m\tau_m) \\ e_{4,m} = \Gamma_m - \exp(-\beta_m\tau_m) \end{cases}, \tag{3.38}$$

to rewrite boundary conditions (eqs. 3.33-3.36) using eq. 3.31. Therefore, eq. 3.33 becomes

$$Y_{1,1}e_{1,1} + Y_{2,1}(-e_{2,1}) = F_0^-(0) - Q_1^-(0), \tag{3.39}$$

eq. 3.34 becomes

$$\begin{matrix} Y_{1,M}\left(e_{1,M} - R_{sfc}e_{3,M}\right) + Y_{2,M}\left(e_{2,M} - R_{sfc}e_{4,M}\right) = \\ R_{sfc}Q_M^-(\tau_M) - Q_M^+(\tau_M) + S_{sfc} \end{matrix}, \tag{3.40}$$

eq. 3.35 becomes

$$\begin{matrix} Y_{1,m}e_{1,m} + Y_{2,m}e_{2,m} - Y_{1,m+1}e_{3,m+1} + Y_{2,m+1}e_{4,m+1} = \\ Q_{m+1}^+(0) - Q_m^+(\tau_m) \end{matrix}, \text{ and} \tag{3.41}$$

eq. 3.36 becomes

$$\begin{matrix} Y_{1,m}e_{3,m} + Y_{2,m}e_{4,m} - Y_{1,m+1}e_{1,m+1} + Y_{2,m+1}e_{2,m+1} = \\ Q_{m+1}^-(0) - Q_m^-(\tau_m) \end{matrix}. \tag{3.42}$$

With eqs. 3.39-3.42, the following pentadiagonal matrix may be derived:

$$\begin{bmatrix} e_{1,1} & -e_{2,1} & & & & & & & \\ e_{1,1} & e_{2,1} & -e_{3,2} & e_{4,2} & & & & & \\ e_{3,1} & e_{4,1} & -e_{1,2} & e_{2,2} & & & & & \\ & & e_{1,2} & e_{2,2} & -e_{3,3} & e_{4,3} & & & \\ & & e_{3,2} & e_{4,2} & -e_{1,3} & e_{2,3} & & & \\ & & & & \vdots & \vdots & & & \\ & & & & e_{1,m} & e_{2,m} & -e_{3,m+1} & e_{4,m+1} & \\ & & & & e_{3,m} & e_{4,m} & -e_{1,m+1} & e_{2,m+1} & \\ & & & & & & \vdots & \vdots & \\ & & & & & & e_{1,M} & e_{2,M} & \\ & & & & & & \left(-R_{sfc}e_{3,M}\right) & \left(-R_{sfc}e_{4,M}\right) & \end{bmatrix} \begin{bmatrix} Y_{1,1} \\ Y_{2,1} \\ Y_{1,2} \\ Y_{2,2} \\ Y_{1,3} \\ Y_{2,3} \\ \vdots \\ Y_{1,m} \\ Y_{2,m} \\ Y_{1,m+1} \\ Y_{2,m+1} \\ \vdots \\ Y_{1,M} \\ Y_{2,M} \end{bmatrix} =$$

$$\begin{bmatrix} F_0^-(0) - Q_1^-(0) \\ \vdots \\ Q_{m+1}^+(0) - Q_m^+(\tau_m) \\ Q_{m+1}^-(0) - Q_m^-(\tau_m) \\ \vdots \\ R_{sfc}Q_M^-(\tau_M) - Q_M^+(\tau_M) + S_{sfc} \end{bmatrix}. \tag{3.43}$$

From eq. 3.43, we notice that eqs. 3.39-3.42 can be rearranged to form a tridiagonal matrix by the following strategies,

$e_{2,m+1}$×eq. 3.41 $- e_{4,m+1}$×eq. 3.42 for even terms, and

$e_{3,m}$×eq. 3.41 $- e_{1,m}$×eq. 3.42 for odd terms.

After rearranging, we can express the tridiagonal matrix as

$$AY = G \tag{3.44}$$

with

$$A = \begin{bmatrix} e_{1,1} & -e_{2,1} & & & & \\ \ddots & \vdots & & & & \\ & \begin{pmatrix} e_{1,m}e_{2,m+1} \\ -e_{3,m}e_{4,m+1} \end{pmatrix} & \begin{pmatrix} e_{2,m}e_{2,m+1} \\ -e_{4,m}e_{4,m+1} \end{pmatrix} & \begin{pmatrix} e_{1,m+1}e_{4,m+1} \\ -e_{3,m+1}e_{2,m+1} \end{pmatrix} & \\ & & \begin{pmatrix} e_{2,m}e_{3,m} \\ -e_{4,m}e_{1,m} \end{pmatrix} & \begin{pmatrix} e_{1,m+1}e_{1,m} \\ -e_{3,m+1}e_{3,m} \end{pmatrix} & \begin{pmatrix} e_{4,m+1}e_{3,m} \\ -e_{2,m+1}e_{1,m} \end{pmatrix} \\ & & \ddots & \vdots & \vdots \\ & & & e_{1,M} - R_{sfc}e_{3,M} & e_{2,M} - R_{sfc}e_{4,M} \end{bmatrix} \tag{3.45}$$

$$Y = \begin{bmatrix} Y_{1,1} \\ Y_{2,1} \\ Y_{1,2} \\ Y_{2,2} \\ \vdots \\ Y_{1,m} \\ Y_{2,m} \\ Y_{1,m+1} \\ Y_{2,m+1} \\ \vdots \\ Y_{1,M} \\ Y_{2,M} \end{bmatrix}, \text{ and} \tag{3.46}$$

$$G = \begin{bmatrix} F_0^-(0) - Q_1^-(0) \\ \vdots \\ e_{2,m+1}[Q_{m+1}^+(0) - Q_m^+(\tau_m)] - e_{4,m+1}[Q_{m+1}^-(0) - Q_m^-(\tau_m)] \\ e_{3,m}[Q_{m+1}^+(0) - Q_m^+(\tau_m)] - e_{1,m}[Q_{m+1}^-(0) - Q_m^-(\tau_m)] \\ \vdots \\ R_{sfc}Q_M^-(\tau_M) - Q_M^+(\tau_M) + S_{sfc} \end{bmatrix}. \tag{3.47}$$

As stated by Toon et al. (1989), eq. 3.44 can be simply described as

$$A_i Y_{i-1} + C_i Y_i + E_i Y_{i+1} = G_i \tag{3.48}$$

by assuming

$$\begin{cases} Y_i = Y_{1,m}, \text{ for } i = 2m-1 \text{ (odd terms)} \\ Y_i = Y_{2,m}, \text{ for } i = 2m \text{ (even terms)} \end{cases}, \tag{3.49}$$

and can be summarized into the following groups. At the top of the 1st layer ($i = 1$), the coefficients of eq. 3.48 are

$$\begin{cases} A_1 = 0 \\ C_1 = e_{1,1} \\ E_1 = -e_{2,1} \\ G_1 = F_0^-(0) - Q_1^-(0) \end{cases}, \tag{3.50}$$

and at the bottom of the M^{th} layer ($i = 2M$), the coefficients can be expressed as

$$\begin{cases} A_{2M} = e_{1,M} - R_{\text{sfc}} e_{3,M} \\ C_{2M} = e_{2,M} - R_{\text{sfc}} e_{4,M} \\ E_{2M} = 0 \\ G_{2M} = R_{sfc} Q_M^-(\tau_M) - Q_M^+(\tau_M) + S_{sfc} \end{cases}. \tag{3.51}$$

For the even internal boundaries ($i = 2$ to $2M-2$), the coefficients are

$$\begin{cases} A_i = e_{1,m} e_{2,m+1} - e_{3,m} e_{4,m+1} \\ C_i = e_{2,m} e_{2,m+1} - e_{4,m} e_{4,m+1} \\ E_i = e_{1,m+1} e_{4,m+1} - e_{3,m+1} e_{2,m+1} \\ G_i = e_{2,m+1}[Q_{m+1}^+(0) - Q_m^+(\tau_m)] - e_{4,m+1}[Q_{m+1}^-(0) - Q_m^-(\tau_m)] \end{cases}, \tag{3.52}$$

and for the odd internal boundaries ($i = 3$ to $2M-1$), the coefficients are

$$\begin{cases} A_i = e_{2,m} e_{3,m} - e_{4,m} e_{1,m} \\ C_i = e_{1,m+1} e_{1,m} - e_{3,m+1} e_{3,m} \\ E_i = e_{4,m+1} e_{3,m} - e_{2,m+1} e_{1,m} \\ G_i = e_{3,m}[Q_{m+1}^+(0) - Q_m^+(\tau_m)] - e_{1,m}[Q_{m+1}^-(0) - Q_m^-(\tau_m)] \end{cases}. \tag{3.53}$$

In this study, we use the tridiagonal matrix algorithm (Cheney & Kincaid, 2007) to solve the tridiagonal matrix, eq. 3.44, to get Y_i for the each boundary, and then by using eq. 3.32, the coefficients $\alpha_{1,m}$ and $\alpha_{2,m}$ can be derived by

$$\begin{cases} \alpha_{1,m} = \left(Y_{1,m} + Y_{2,m}\right)\exp(-\beta_m \tau_m) \\ \alpha_{2,m} = Y_{1,m} - Y_{2,m} \end{cases}. \tag{3.54}$$

As a result, the upward and downward flux on each layer boundary can be calculated by eq. 3.28.

3.3.2 2-/4-stream approximation

The 2-/4-stream approximation (Fu et al., 1997; Liou, 2002; Toon et al., 1989) is developed based on the 2-stream source function technique proposed by Toon et al. (1989), which states that the 2-stream approximations can accurately approximate the longwave intensities of the source function (eq. 3.12). The concept of the 2-/4-stream approximation is to use the 2-stream approach to represent the source function analytically, and to integrate the intensity field at 2 upward and 2 downward specifically chosen angles (4 streams) to approximate the total upward and downward fluxes. Therefore, instead of starting with the diffuse flux version of the radiative transfer equation, as in eq. 3.13, we derive the 2-/4-stream approximation from the diffuse intensity (eqs. 3.11 and 3.12).

Given the additional theorem for spherical harmonics, the azimuthal independent phase function can be expanded by the L terms of Legendre polynomials (P_l), as follows (Liou, 2002; Wendisch & Yang, 2012):

$$P(\mu, \mu') = \sum_{l=0}^{L} w_l P_l(\mu) P_l(\mu'), \tag{3.55}$$

where w_l is the Legendre polynomial expansion coefficient with index l, and can be calculated by the orthogonal properties of Legendre polynomials. With the 2-stream approximation, the intensity in each layer is

$$I(\tau,\mu_1)=\begin{cases}I^+(\tau), \text{ for } \mu_1=\frac{1}{\sqrt{3}}\\ I^-(\tau), \text{ for } \mu_1=\frac{-1}{\sqrt{3}},\end{cases} \tag{3.56}$$

where the selection of μ_1 is based on Gaussian quadrature. The phase function can be simply represented by the first 2 moments ($L=1$) of the Legendre polynomials, or

$$\begin{aligned}P(\mu_1,\mu_1') &= 1+3g\mu_1\mu_1'\\ &= \begin{cases}1+g, \text{for } \mu_1\mu_1'>0.\\ 1-g, \text{for } \mu_1\mu_1'<0\end{cases}\end{aligned} \tag{3.57}$$

As a result, from eq. 3.12, the azimuthal independent source function S becomes

$$\begin{aligned}S(\tau,\mu) &= \frac{\omega}{2}\int_{-1}^{1}P(\mu,\mu')I(\tau,\mu')d\mu'+(1-\omega)B(T)\\ &= \frac{\omega}{2}\left[\int_0^1 P(\mu,\mu')I(\tau,\mu')d\mu'+\int_{-1}^{0}P(\mu,\mu')I(\tau,\mu')d\mu'\right]+(1-\omega)B(T)\end{aligned}. \tag{3.58}$$

By using eqs. 3.56 and 3.57 and taking the linear approximation of the Planck function (eq. 3.24), S can be derived as

$$S(\tau,\mu_1)=\frac{\omega}{2}[(1+g)I^+(\tau)+(1-g)I^-(\tau)]+(1-\omega)(B_0+B_1\tau). \tag{3.59}$$

Meanwhile, eq. 3.11 can also be rewritten under the azimuthal independent assumption using the 2-stream approximation, as

$$\begin{cases}+\mu_1\frac{dI^+(\tau)}{d\tau}=I^+(\tau)-S^+(\tau), \text{ for } \mu_1=\frac{1}{\sqrt{3}}\\ -\mu_1\frac{dI^-(\tau)}{d\tau}=I^-(\tau)-S^-(\tau), \text{ for } \mu_1=\frac{-1}{\sqrt{3}}.\end{cases} \tag{3.60}$$

Combining eqs. 3.59 and 3.60 leads to coupled differential equations for diffuse intensities:

$$\begin{cases}\frac{dI^+(\tau)}{d\tau}=\gamma_1 I^+(\tau)-\gamma_2 I^-(\tau)-\gamma_3(B_0+B_1\tau)\\ \frac{dI^-(\tau)}{d\tau}=\gamma_2 I^+(\tau)-\gamma_1 I^-(\tau)+\gamma_3(B_0+B_1\tau)\end{cases}, \tag{3.61}$$

with γ_1 and γ_2 from eqs. 3.18 and 3.19 for $\widetilde{D} = 1/\mu_1$ and $\chi = g$ rearranged to

$$\begin{aligned}\gamma_1 &= \widetilde{D}\left[1 - \frac{\omega}{2}(1+\chi)\right] \\ &= \frac{1}{\mu_1}\left[1 - \frac{\omega}{2}(1+g)\right]\end{aligned}, \tag{3.62}$$

$$\begin{aligned}\gamma_2 &= \widetilde{D}\frac{\omega}{2}(1-\chi) \\ &= \frac{\omega}{2\mu_1}(1-g)\end{aligned}, \text{ and} \tag{3.63}$$

$$\gamma_3 = \frac{1-\omega}{\mu_1}. \tag{3.64}$$

To solve the coupled differential equations (eq. 3.61), we may organize the equations to form

$$\begin{cases}\frac{dU(\tau)}{d\tau} = (\gamma_1 + \gamma_2)V(\tau) \\ \frac{dV(\tau)}{d\tau} = (\gamma_1 - \gamma_2)U(\tau) - 2\gamma_3(B_0 + B_1\tau)\end{cases}, \tag{3.65}$$

where $U(\tau) = I^+(\tau) + I^-(\tau)$ and $V(\tau) = I^+(\tau) - I^-(\tau)$, and a second order differential equation can be derived as follows:

$$\begin{aligned}\frac{d^2U(\tau)}{d\tau^2} &= (\gamma_1 + \gamma_2)\frac{dV(\tau)}{d\tau} \\ &= U(\tau)(\gamma_1 + \gamma_2)(\gamma_1 - \gamma_2) - 2\gamma_3(\gamma_1 + \gamma_2)(B_0 + B_1\tau)\end{aligned} \tag{3.66}$$

$$\frac{d^2U(\tau)}{d\tau^2} - \beta^2 U(\tau) = -2\gamma_3(\gamma_1 + \gamma_2)(B_0 + B_1\tau) \tag{3.67}$$

Since the homogeneous solution of eq. 3.67 is a linear combination of $\exp(\beta\tau)$ and $\exp(-\beta\tau)$, we may assume the homogeneous (subscript h) solution (I_h) of eq. 3.61 is in the same form, such as

$$\begin{cases}I_h^+(\tau) = A_h \exp(\beta\tau) + B_h \exp(-\beta\tau) \\ I_h^-(\tau) = C_h \exp(\beta\tau) + D_h \exp(-\beta\tau)\end{cases}, \tag{3.68}$$

where A_h, B_h, C_h, and D_h are coefficients. By using eqs. 3.68 and 3.61, the relationships among A_h, B_h, C_h, and D_h are

$$\begin{cases} A_h = \frac{-\gamma_2}{\beta-\gamma_1} C_h \\ B_h = \frac{\gamma_2}{\beta+\gamma_1} D_h \end{cases}. \tag{3.69}$$

By comparing with eq. 3.61, we may assume the particular (subscript p) solution (I_p) of eq. 3.61 is also a linear combination of τ, such as

$$I_p = h + k\tau. \tag{3.70}$$

Then, we take the derivative of $dI^{\pm}(\tau)/d\tau$:

$$\begin{cases} \frac{d^2I^+(\tau)}{d\tau^2} = \gamma_1 \frac{dI^+(\tau)}{d\tau} - \gamma_2 \frac{dI^-(\tau)}{d\tau} - \gamma_3 B_1 \\ \qquad\qquad = (\gamma_1^2 - \gamma_2^2) I^+ - \gamma_3(\gamma_1+\gamma_2)(B_0 + B_1\tau) - \gamma_3 B_1 \\ \frac{d^2I^-(\tau)}{d\tau^2} = \gamma_2 \frac{dI^+(\tau)}{d\tau} - \gamma_1 \frac{dI^-(\tau)}{d\tau} + \gamma_3 B_1 \\ \qquad\qquad = (\gamma_1^2 - \gamma_2^2) I^- - \gamma_3(\gamma_1+\gamma_2)(B_0 + B_1\tau) + \gamma_3 B_1 \end{cases}, \tag{3.71}$$

and using eq. 3.70, the coefficients h and k are

$$\begin{cases} h = \frac{\gamma_3}{\gamma_1-\gamma_2}\left(B_0 + \frac{B_1}{\gamma_1+\gamma_2}\right) \\ k = \frac{\gamma_3}{\gamma_1-\gamma_2} B_1 \end{cases}, \text{ for } I_p^+(\tau) \text{ and} \tag{3.72}$$

$$\begin{cases} h = \frac{\gamma_3}{\gamma_1-\gamma_2}\left(B_0 - \frac{B_1}{\gamma_1+\gamma_2}\right) \\ k = \frac{\gamma_3}{\gamma_1-\gamma_2} B_1 \end{cases}, \text{ for } I_p^-(\tau). \tag{3.73}$$

Therefore, by using the homogeneous (eqs. 3.68 and 3.69) and particular solution (eqs. 3.70, 3.72 and 3.73) of eq. 3.61, the upward and downward diffuse intensities are

$$\begin{cases} I^+(\tau) = A_h \exp(\beta\tau) + \Gamma D_h \exp(-\beta\tau) + \xi\left[\left(B_0 + \frac{B_1}{\gamma_1+\gamma_2}\right) + B_1\tau\right] \\ I^-(\tau) = \Gamma A_h \exp(\beta\tau) + D_h \exp(-\beta\tau) + \xi\left[\left(B_0 - \frac{B_1}{\gamma_1+\gamma_2}\right) + B_1\tau\right] \end{cases} \tag{3.74}$$

with

$$\xi = \frac{\gamma_3}{\gamma_1-\gamma_2} = 1. \tag{3.75}$$

In practice, with an atmosphere with M layers, because eq. 3.74 contains positive exponents, we apply the same technique used in section 3.3.1 (eqs. 3.32 and 3.48-3.54) to make the computation more stable, in the following form:

$$\begin{cases} A_{h,m} = \left(Y_{1,m} + Y_{2,m}\right)\exp(-\beta_m \tau_m) \\ D_{h,m} = Y_{1,m} - Y_{2,m} \end{cases}, \tag{3.76}$$

and use the boundary conditions, which are similar to eqs. 3.33-3.36, follows:

$$\begin{cases} I_1^-(0) = I_0^-(0) \\ I_M^+(\tau_M) = R_{sfc} I_M^-(\tau_M) + \varepsilon_{sfc} B\left(T_{sfc}\right) \\ I_m^+(\tau = \tau_m) = I_{m+1}^+(\tau = 0) \\ I_m^-(\tau = \tau_m) = I_{m+1}^-(\tau = 0) \end{cases}, \tag{3.77}$$

to solve the coefficients $Y_{1,m}$ and $Y_{2,m}$. With eqs. 3.74 and 3.75, the 2-stream approximation of the source function $S^{\pm}$ (eq. 3.59) can be simplified to

$$\begin{cases} S_m^+(\tau, \mu_1) = H_m \mu_1 \exp\left(\beta_m(\tau - \tau_m)\right) + J_m \mu_1 \exp(-\beta_m \tau) \\ \qquad\qquad +\eta_{1,m} + \eta_{2,m}\tau, \text{ for } \mu_1 = \frac{1}{\sqrt{3}} \\ S_m^-(\tau, \mu_1) = K_m \mu_1 \exp\left(\beta_m(\tau - \tau_m)\right) + Z_m \mu_1 \exp(-\beta_m \tau) \\ \qquad\qquad +\sigma_{1,m} + \sigma_{2,m}\tau, \text{ for } \mu_1 = \frac{-1}{\sqrt{3}} \end{cases}, \tag{3.78}$$

with

$$\begin{cases} H_m = \left(\frac{1}{\mu_1} - \beta_m\right)\left(Y_{1,m} + Y_{2,m}\right) \\ J_m = \left(\frac{1}{\mu_1} + \beta_m\right)\Gamma_m\left(Y_{1,m} - Y_{2,m}\right) \\ \eta_{1,m} = \left[B_{0,m} + B_{1,m}\left(\frac{1}{\gamma_{1,m}+\gamma_{2,m}} - \mu_1\right)\right] \\ \eta_{2,m} = B_{1,m} \end{cases} \text{ and} \tag{3.79}$$

$$\begin{cases} K_m = \left(\frac{1}{\mu_1} + \beta_m\right) \Gamma_m \left(Y_{1,m} + Y_{2,m}\right) \\ Z_m = \left(\frac{1}{\mu_1} - \beta_m\right) \left(Y_{1,m} - Y_{2,m}\right) \\ \sigma_{1,m} = \left[B_{0,m} - B_{1,m}\left(\frac{1}{\gamma_{1,m}+\gamma_{2,m}} - \mu_1\right)\right] \\ \sigma_{2,m} = B_{1,m} \end{cases}. \tag{3.80}$$

Based on the integral technique (Liou, 2002; Wendisch & Yang, 2012), we can directly solve eq. 3.60 for an arbitrary cosine of the zenith angle (μ) by multiplying by $\exp(-\tau/\mu)$ or $\exp(\tau/\mu)$ as follows:

$$\begin{cases} \mu \exp\left(-\frac{\tau}{\mu}\right) dI_m^+(\tau,\mu) = \exp\left(-\frac{\tau}{\mu}\right) I_m^+(\tau,\mu) d\tau \\ \qquad\qquad -\exp\left(-\frac{\tau}{\mu}\right) S_m^+(\tau,\mu) d\tau, \text{ for } 0 < \mu \leq 1 \\ -\mu \exp\left(\frac{\tau}{\mu}\right) dI_m^-(\tau,\mu) = \exp\left(\frac{\tau}{\mu}\right) I_m^-(\tau,\mu) d\tau \\ \qquad\qquad -\exp\left(\frac{\tau}{\mu}\right) S_m^-(\tau,\mu) d\tau, \text{ for } -1 \leq \mu < 0 \end{cases}. \tag{3.81}$$

By using the chain rule,

$$\begin{cases} d\left[\exp\left(-\frac{\tau}{\mu}\right) I_m^+(\tau,\mu)\right] = \exp\left(-\frac{\tau}{\mu}\right) dI_m^+(\tau,\mu) - \exp\left(-\frac{\tau}{\mu}\right) I_m^+(\tau,\mu) d\frac{\tau}{\mu} \\ d\left[\exp\left(\frac{\tau}{\mu}\right) I_m^-(\tau,\mu)\right] = \exp\left(\frac{\tau}{\mu}\right) dI_m^-(\tau,\mu) + \exp\left(\frac{\tau}{\mu}\right) I_m^-(\tau,\mu) d\frac{\tau}{\mu} \end{cases}, \tag{3.82}$$

and taking integration from 0 to τ_m, eq. 3.81 becomes

$$\begin{aligned} I_m^+(0,\mu) = {} & I_m^+(\tau_m,\mu) \exp\left(\frac{-\tau_m}{\mu}\right) \\ & + \int_0^{\tau_m} S_m^+(\tau',\mu) \exp\left(\frac{-\tau'}{\mu}\right) d\frac{\tau'}{\mu}, \text{ for } 0 < \mu \leq 1 \end{aligned}, \text{ and} \tag{3.83}$$

$$\begin{aligned} I_m^-(\tau_m,\mu) = {} & I_m^-(0,\mu) \exp\left(\frac{-\tau_m}{\mu}\right) \\ & + \int_0^{\tau_m} S_m^-(\tau',\mu) \exp\left(\frac{-(\tau_m-\tau')}{\mu}\right) d\frac{\tau'}{\mu}, \text{ for } -1 \leq \mu < 0 \end{aligned}. \tag{3.84}$$

With the simplified 2-stream source function (eq. 3.78), we can calculate the integration in eqs. 3.83 and 3.84, and the upward and downward diffuse intensities at the cosine of zenith angle μ may be approximated as follows.

$$
\begin{aligned}
I_m^+(0,\mu) &\approx I_m^+(\tau_m,\mu)\exp\left(\frac{-\tau_m}{\mu}\right) + \int_0^{\tau_m} S_m^+(\tau',\mu_1)\exp\left(\frac{-\tau'}{\mu}\right) d\frac{\tau'}{\mu} \\
&= I_m^+(\tau_m,\mu)\exp\left(\frac{-\tau_m}{\mu}\right) \\
&+ \int_0^{\tau_m} \left[\begin{matrix} H_m\mu_1\exp\left(\beta_m(\tau'-\tau_m)\right) + J_m\mu_1\exp(-\beta_m\tau') \\ +\eta_{1,m} + \eta_{2,m}\tau' \end{matrix}\right] \exp\left(\frac{-\tau'}{\mu}\right) d\frac{\tau'}{\mu} \\
&= I_m^+(\tau_m,\mu)\exp\left(\frac{-\tau_m}{\mu}\right) \\
&+ \frac{\mu_1}{\mu\beta_m - 1} H_m\left[\exp\left(\frac{-\tau_m}{\mu}\right) - \exp(-\beta_m\tau_m)\right] \\
&+ \frac{\mu_1}{\mu\beta_m + 1} J_m\left[1 - \exp\left(\frac{-\tau_m}{\mu}(\mu\beta_m + 1)\right)\right] \\
&+ \eta_{1,m}\left[1 - \exp\left(\frac{-\tau_m}{\mu}\right)\right] \\
&+ \eta_{2,m}\left[\mu - (\tau_m + \mu)\exp\left(\frac{-\tau_m}{\mu}\right)\right], \text{ for } 0 < \mu \le 1
\end{aligned}
\tag{3.85}
$$

$$
\begin{aligned}
I_m^-(\tau_m,\mu) &\approx I_m^-(0,\mu)\exp\left(\frac{-\tau_m}{\mu}\right) + \int_0^{\tau_m} S_m^-(\tau',\mu_1)\exp\left(\frac{-(\tau_m-\tau')}{\mu}\right) d\frac{\tau'}{\mu} \\
&= I_m^-(0,\mu)\exp\left(\frac{-\tau_m}{\mu}\right) \\
&+ \int_0^{\tau_m} \left[\begin{matrix} K_m\mu_1\exp\left(\beta_m(\tau'-\tau_m)\right) + Z_m\mu_1\exp(-\beta_m\tau') \\ +\sigma_{1,m} + \sigma_{2,m}\tau' \end{matrix}\right] \exp\left(\frac{-(\tau_m-\tau')}{\mu}\right) d\frac{\tau'}{\mu} \\
&= I_m^-(0,\mu)\exp\left(\frac{-\tau_m}{\mu}\right) \\
&+ \frac{\mu_1}{\mu\beta_m + 1} K_m\left[1 - \exp\left(\frac{-\tau_m}{\mu}(\mu\beta_m + 1)\right)\right] \\
&+ \frac{\mu_1}{\mu\beta_m - 1} Z_m\left[\exp\left(\frac{-\tau_m}{\mu}\right) - \exp(-\beta_m\tau_m)\right] \\
&+ \sigma_{1,m}\left[1 - \exp\left(\frac{-\tau_m}{\mu}\right)\right] \\
&+ \sigma_{2,m}\left[\tau_m - \mu + \mu\exp\left(\frac{-\tau_m}{\mu}\right)\right], \text{ for } -1 \le \mu < 0
\end{aligned}
\tag{3.86}
$$

The downward diffuse intensity at zenith angle θ on the bottom of each atmosphere layer may be calculated by using eq. 3.86, and then the upward diffuse intensity at zenith angle θ on the top of each atmosphere layer may be derived by using eq. 3.85 and the surface boundary condition. As a result, following eq. 3.14, we may integrate 2 chosen directions (μ_1 and μ_2) of the upward diffuse intensity to approximate the total upward flux on each boundary, and the downward flux can also be calculated in the same method, such as

$$F_m^+(\tau) = 2\pi \int_0^1 I_m(\tau,\mu)\mu d\mu \approx 2\pi \sum_{i=1}^{2} I_m^+(\tau,\mu_i)\mu_i s_i \text{, for } \mu_i = 0.2113248 \text{ and } 0.7886752, \text{ and} \quad (3.87)$$

$$F_m^-(\tau) = 2\pi \int_0^{-1} I_m(\tau,\mu)\mu d\mu \approx 2\pi \sum_{i=1}^{2} I_m^-(\tau,\mu_i)\mu_i s_i \text{, for } \mu_i = -0.2113248 \text{ and } -0.7886752, \quad (3.88)$$

where the selection of μ_i is based on the double Gaussian quadrature (Liou, 2002; Wendisch & Yang, 2012) with weighting $s_1 = s_2 = 0.5$.

Although, in this derivation, the diffusivity factors $\widetilde{D} = 1/\mu_1 = \pm\sqrt{3}$ are used to approximate the mean intensities of the source function, using ± 2 or ± 1.66 for the diffusivity factors are also suggested in other studies as shown in Table 3.4 (Fu et al., 1997; Liou, 2002; Toon et al., 1989), which show similar simulated flux results even though they choose different diffusivity factors.

3.3.3 *n*-stream approximation

In this study, n-stream approximations (with $n \geq 4$, where n is an even number) are performed by a sophisticated and numerical stable program, called DIScrete Ordinate Radiative Transfer or DISORT (Stamnes et al., 1988; Stamnes et al., 2017), which

comprehensively solves the radiative transfer equations (eqs. 3.11 and 3.12) by the Discrete Ordinate Method (Chandrasekhar, 1950). Increasing the number of streams leads to a better approximation of the solution of the full radiative transfer equations. The DISORT program can be downloaded from http://lllab.phy.stevens.edu/disort/. The basic concept of the method is described below.

With the phase function expanded using n Legendre polynomials as in eq. 3.55, the azimuthal independent radiative transfer equation stated in eqs. 3.11 and 3.12 can be discretized into n differential equations ($i = \pm 1,\ \pm 2,\ \pm n/2$) as follows (Fu et al., 1997; Liou, 2002; Wendisch & Yang, 2012):

$$\begin{aligned}\mu_i \frac{dI(\tau,\mu_i)}{d\tau} &= I(\tau,\mu_i) - \frac{\omega}{2}\sum_{j=-n}^{n} I(\tau,\mu_j)P(\mu_i,\mu_j)s_j - (1-\omega)B(T) \\ &= I(\tau,\mu_i) - \frac{\omega}{2}\sum_{l=0}^{L} w_l P_l(\mu_i)\sum_{j=-n}^{n} I(\tau,\mu_j)P_l(\mu_j)s_j - (1-\omega)B(T)\end{aligned}, \quad (3.89)$$

where $j \neq 0$, and the selection of the cosine of zenith angles (μ_i) and integration weights (s_j) are based on the Gaussian quadrature rule, which satisfies $\mu_{-i} = -\mu_i$, $s_j = s_{-j}$, and $\sum_{j=-n}^{n} s_n = 2$.

By solving eq. 3.89, the solution of the diffuse intensities contains n unknown coefficients. In a general situation, such as an M-layer atmosphere, $M \times n$ unknown coefficients can be obtained by applying boundary conditions (eq. 3.77), which provide $M \times n$ equations. Therefore, upward and downward fluxes may be calculated by summation of quadrature weighted upward and downward intensities, respectively, such as,

$$\begin{aligned}F_m^{\pm}(\tau) &= 2\pi \int_0^{\pm 1} I_m(\tau,\mu)\mu d\mu \\ &\approx 2\pi \sum_{i=1}^{n} I_m^{\pm}(\tau,\mu_{\pm i})\mu_{\pm i} s_{\pm i}\end{aligned}. \quad (3.90)$$

This is a general expression of eqs. 3.87 and 3.88.

3.3.4 δ-function adjustment and similarity principle

In radiation transfer simulations, to overcome the strong forward scattering properties of ice clouds when the asymmetry factor is close to 1 (large particles) in Figure 3.4, the forward scattering peak of the phase function is truncated based on the δ-function (Joseph et al., 1976; Potter, 1970) and the other optical properties, including the optical thickness (τ) and the single-scattering albedo (ω), must also be scaled based on the similarity principle (Fu et al., 1997; Liou, 2002; Wendisch & Yang, 2012), as follows:

$$\tau' = (1 - \omega f)\tau, \text{ and} \tag{3.91}$$

$$\omega' = \frac{(1-f)\omega}{1-f\omega}, \tag{3.92}$$

where τ' and ω' are the scaled optical thickness and single-scattering albedo, respectively, and f is the fraction of the scattered energy in the forward peak (so f is called the truncation factor).

Since absorption dominates over scattering processes in the longwave spectral bands (Fu et al., 1997) and this study focuses on the flux simulations, we may use the asymmetry factor to represent the phase function analytically by the Henyey-Greenstein (HG) phase function (Henyey & Greenstein, 1941; Liou, 2002),

$$\begin{aligned} P_{\mathrm{HG}}(\cos\Theta) &= \frac{1-g^2}{(1+g^2-2g\cos\Theta)^{3/2}} \\ &= \sum_{l=0}^{L}(2l+1)g^l P_l(\cos\Theta) \end{aligned}, \tag{3.93}$$

where Θ is the scattering angle, and the expansion coefficients of the HG phase function can be expressed as

$$w_l = (2l+1)g^l. \tag{3.94}$$

After applying the δ-function adjustment to the HG phase function (Liou, 2002) as follows:

$$P_{\mathrm{HG},\delta}(\cos\Theta) = 2f\delta(1-\cos\Theta) + (1-f)P'_{\mathrm{HG}}(\cos\Theta), \tag{3.95}$$

the scaled HG phase function is expressed as

$$P'_{\mathrm{HG}}(\cos\Theta) = \sum_{l=0}^{L} w'_l P_l(\cos\Theta), \tag{3.96}$$

where the w'_l values are the scaled Legendre polynomial expansion coefficients. Furthermore, requiring that the phase functions are identical before and after the δ-function adjustment, or

$$P_{\mathrm{HG}}(\cos\Theta) = P_{\mathrm{HG},\delta}(\cos\Theta), \tag{3.97}$$

and applying the orthogonal properties of the Legendre polynomials (Liou, 2002), we derive the scaled expansion coefficients as

$$w'_l = \frac{w_l - f(2l+1)}{1-f}. \tag{3.98}$$

Therefore, f can be determined by making the $(L+1)^{\text{th}}$ moment of the scaled HG phase function equal to 0 (Liou, 2002):

$$\begin{aligned} f &= \frac{w_{L+1}}{2(L+1)+1} \\ &= g^{L+1} \end{aligned}. \tag{3.99}$$

Although the simulated intensities are not exact when the phase function is scaled according to the truncation factor f, fluxes can be accurately calculated by this approach (Stamnes et al., 2017; Wiscombe, 1977).

In the 2-stream and 2-/4-stream approximations, since we use the first 2 moments ($L = 1$) of the Legendre polynomials to expand the phase function, the truncation factor

f is g^2. In general, the truncation factor f is g^n for the n-stream approximations, which uses n moments of the Legendre polynomials ($L = n - 1$) to expand the HG phase function.

3.4 Results and discussion

This section compares the accuracy and efficiency of different RTM approximations, listed in Table 3.5. All comparisons use the MC6 ice cloud model. We apply the parameterizations of ice cloud band-averaged bulk longwave optical properties shown in Figure 3.4 and the δ-function adjustment technique mentioned in section 3.3.4. Then, we calculate the broadband emissivity of an isothermal homogeneous cloud layer, as shown in Figure 3.6. The emissivity (ε_{cld}) of the cloud layer can be derived by

$$\varepsilon_{cld} = \frac{F}{\pi B(T_{cld})}, \tag{3.100}$$

where F is the outgoing flux on both the upper and lower cloud boundaries, and $B(T_{cld})$ is the Planck function at the cloud temperature T_{cld}. Since the values of the mass extinction coefficients are similar in all visible bands (Figure 3.7), to make consistent comparisons we use the shortwave extinction optical thickness ($\tau_{sw,ext}$) in RRTMG_SW band 24 (0.78-0.62 μm) to simulate emissivity in longwave RRTMG_LW bands 1 to 16 for different RTMs. First, the longwave extinction optical thickness ($\tau_{lw,ext}$) is parameterized by

$$\tau_{lw,ext} = \frac{\overline{\kappa}_{lw,ext}}{\overline{\kappa}_{sw,ext}} \tau_{sw,ext}. \tag{3.101}$$

The mass extinction coefficients in the visible bands shown in Figure 3.7 are then parameterized by the method described in section 3.2, and the R^2 values of the polynomial fittings are all larger than 0.9.

Table 3.5 Abbreviations of RTMs.

Abbreviation	RTM
AA	Absorption approximation
ASA	Absorption approximation with scattering parameterization
2S	2-stream approximation
2/4S	2-/4-stream approximation
*n*S*n*M	n-Stream DISORT with HG Phase function expanded from n Moments of Legendre expansion coefficients

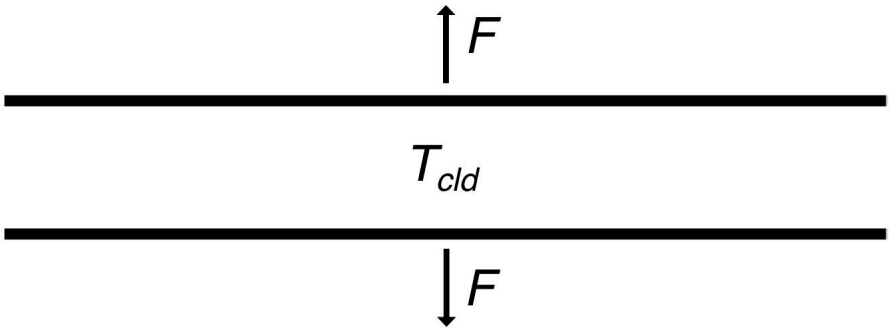

Figure 3.6 A homogeneous cloud layer at temperature T_{cld}.

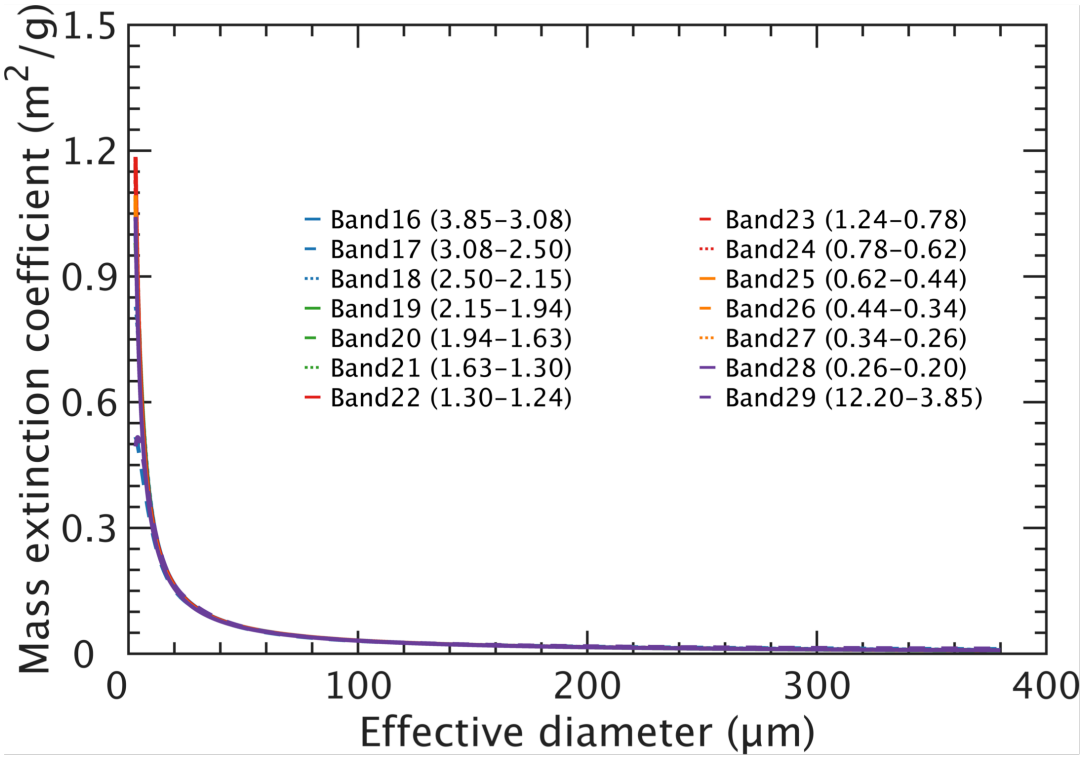

Figure 3.7 Parameterizations of $\bar{\kappa}_{ext}$ for RRTMG_SW bands. Colored lines indicate different RRTMG_SW spectral bands.

In the absorption approximation method (AA; Fu et al., 1997), the absorption optical thickness ($\tau_{lw,abs}$)

$$\tau_{lw,abs} = \tau_{lw,ext}(1 - \bar{\omega}_{lw}), \tag{3.102}$$

is used to compute flux. The absorption approximation method with scattering parameterization (ASA; Chou et al., 1999) simulates flux by utilizing the scaled absorption optical thickness ($\tau^*_{lw,abs}$):

$$\tau^*_{lw,abs} = \tau_{lw,ext}[1 - \bar{\omega}_{lw}(1 - b_s)], \tag{3.103}$$

where b_s is the backscattering function, parameterized by

$$b_s = 1 - \sum_j^4 a_{s,j} \bar{g}_{lw}^{j-1} \tag{3.104}$$

with coefficients $a_{s,1} = 0.5$, $a_{s,2} = 0.3738$, $a_{s,3} = 0.0076$, and $a_{s,4} = 0.1186$. For the 2-stream (2S), the 2-/4-stream (2/4S), and the n-stream (nSnM) approximations, $\tau_{lw,ext}$, $\bar{\omega}_{lw}$, and $\bar{g}_{lw}$ are used to calculate fluxes by applying eq. 3.94 to generate the expansion coefficients of the HG phase function for nSnM and using eqs. 3.91, 3.92, and 3.98 to adjust optical properties with truncation factors $f = \bar{g}_{lw}^2$ for 2S and 2/4S, and $f = \bar{g}_{lw}^n$ for nSnM by eq. 3.99.

To compute an "accurate" reference for comparisons of the approximate RTMs, the reference of cloud emissivity was calculated by using the 128-stream DISORT (128S128M), and is shown in Figure 3.8. The emissivity increases with visible optical thickness, and increases at first and then slightly decreases with D_e. Table 3.6 lists 840 cases used to compare approximate and reference emissivity for each RTM approximation. The percentage emissivity errors of 22 different approximate RTMs are shown in Figure 3.9.

Table 3.6 Cases used in emissivity comparisons.

$\tau_{sw,ext}$	D_e
0.1 to 0.9 with interval 0.1, 1 to 9 with interval 1, and 10 to 100 with interval 10	10 to 300 μm with interval 10 μm

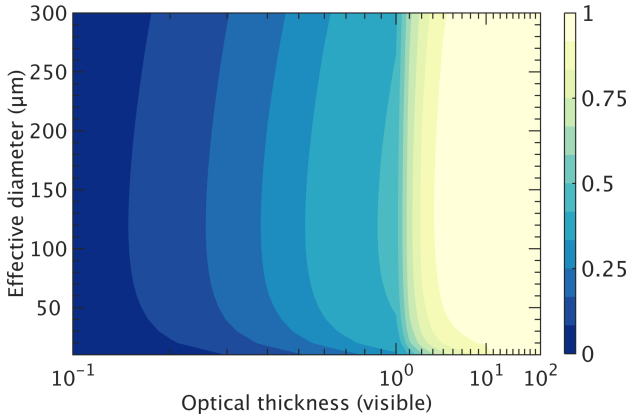

Figure 3.8 Ice cloud layer emissivity simulated by the 128-stream DISORT as a function of visible optical thickness and D_e.

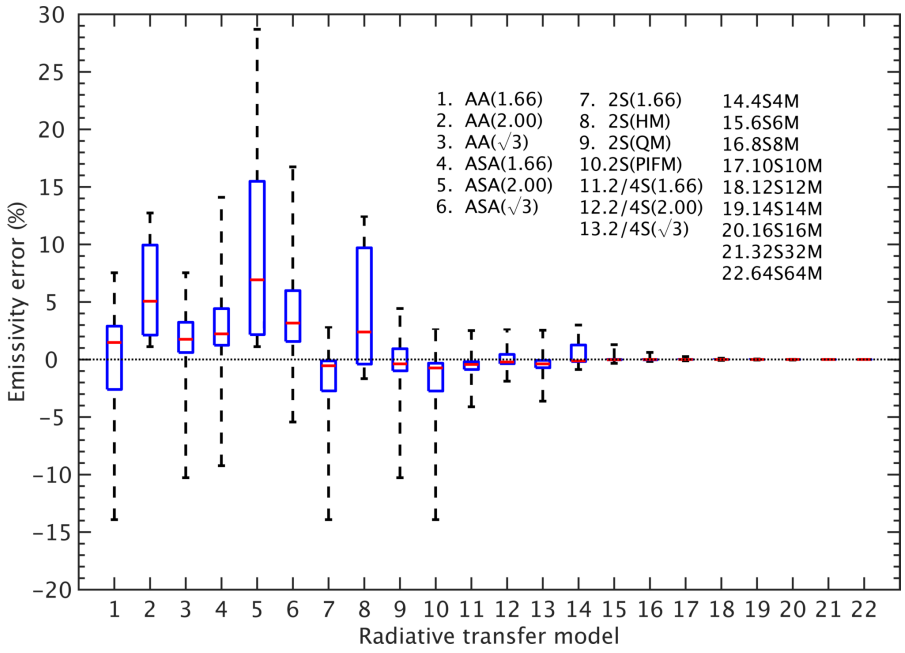

Figure 3.9 Emissivity percentage errors from various RTMs by comparing to reference emissivity from 128S128M DISORT. Each error is 100 × (approximate RTM - reference) / reference. In each box, the red line means the median, and the bottom and top of the blue box indicate the 25th and 75th percentiles, respectively for the 840 cases. Upper and lower edges of dashed lines denote the extreme errors from the 840 cases. Numbers in parentheses are diffusivity factors. HM, QM, PIFM mean the hemispheric mean, the quadrature method, and the practical improved flux method, respectively.

For the AA and ASA models, most of simulation errors are within ±15%, except for ASA(2.00), which overestimates emissivity with up to nealy 30% error. Figure 3.10 shows the error distributions with visible optical thickness and D_e for the AA and ASA models. With the AA models, the approximate emissivity is too small when the visible optical thickness is less than approximately 1, and is too large when the visible optical thickness is larger than 1. Errors for the estimated emissivity are larger when D_e is smaller. The error distributions of AA are different from using ASA, which generates a positive error peak when visible optical thickness is about 1 and D_e is less than 50 μm, and has negative errors when visible optical thickness is small and D_e is large. When using a diffusivity factor of 2, both AA and ASA overestimate emissivity with the largest error for AA around 1 visible optical thickness and with the largest error for ASA when visible optical thickness is between 0.3 and 2 and D_e is less than 30 μm.

For the 2S model, in Figure 3.9 the overall errors are smaller with less biases than the AA and ASA models, and the largest emissivity errors are within ±15%. Figure 3.11 shows that the 2S(1.66), 2S(QM), and 2S(PIFM) models have similar error patterns with maximum positive errors along visible optical thickness about 2 and largest negative errors when both visible optical thickness and D_e are small. On the other hand, the emissivity simulated by using the 2S(HM) is overestimated when visible optical thickness is smaller than about 10 with significant errors (almost +15%) with optical thickness around 0.6 to 1. Edwards (1996) and Toon et al. (1989) justified the use of 2S(HM), and specifically emphasized that with a large optical thickness in an isothermal atmospheric layer, the diffusivity factor should be 2 (hemispheric mean) to get the

correct distribution of the Planck function in the longwave spectrum. However, O'Brien et al. (1997) argued that this restriction is correct in the interior point of the layer, but is not justified close to the upper and lower cloud boundaries, where scattering and emission processes determine the angular distribution of the intensities. By numerical comparisons, Figure 3.9 and Figure 3.11 support O'Brien's arguments, showing that most simulation errors are smaller, including smaller biases, when using 2S(QM), 2S(PIDM), or 2S(1.66), but when using 2S(HM), the emissivity is usually significantly overestimated.

In Figure 3.9, the emissivity errors for the 2/4S models with different diffusivity factors are similar and are all within ±5%. The small errors support arguments in Liou (2002). Figure 3.12 shows that for the 2/4S models the simulated emissivity has a negative error peak when D_e is less than 30 μm and visible optical thickness is about 1-3, and has significant positive errors when D_e is large and visible optical thickness is less than 1. Specifically, the largest positive errors are about 3% for all 2/4S models, but using 2/4S(2.00) gives smaller negative simulation errors (about -2%) than 2/4S(1.66) and 2/4S($\sqrt{3}$) (about -4%). In the comparisons of simulation errors using the 2/4S and 4S4M models, although the 4S4M model calculates radiation fields by using higher angular resolution than the 2/4S models, larger overestimations occur for 4S4M when the visible optical thickness is less than 0.5. However, in Figure 3.9, by increasing the number of streams, the extreme error is about 1% for the 6S6M model, and errors are close to 0 when the stream number is larger than 12.

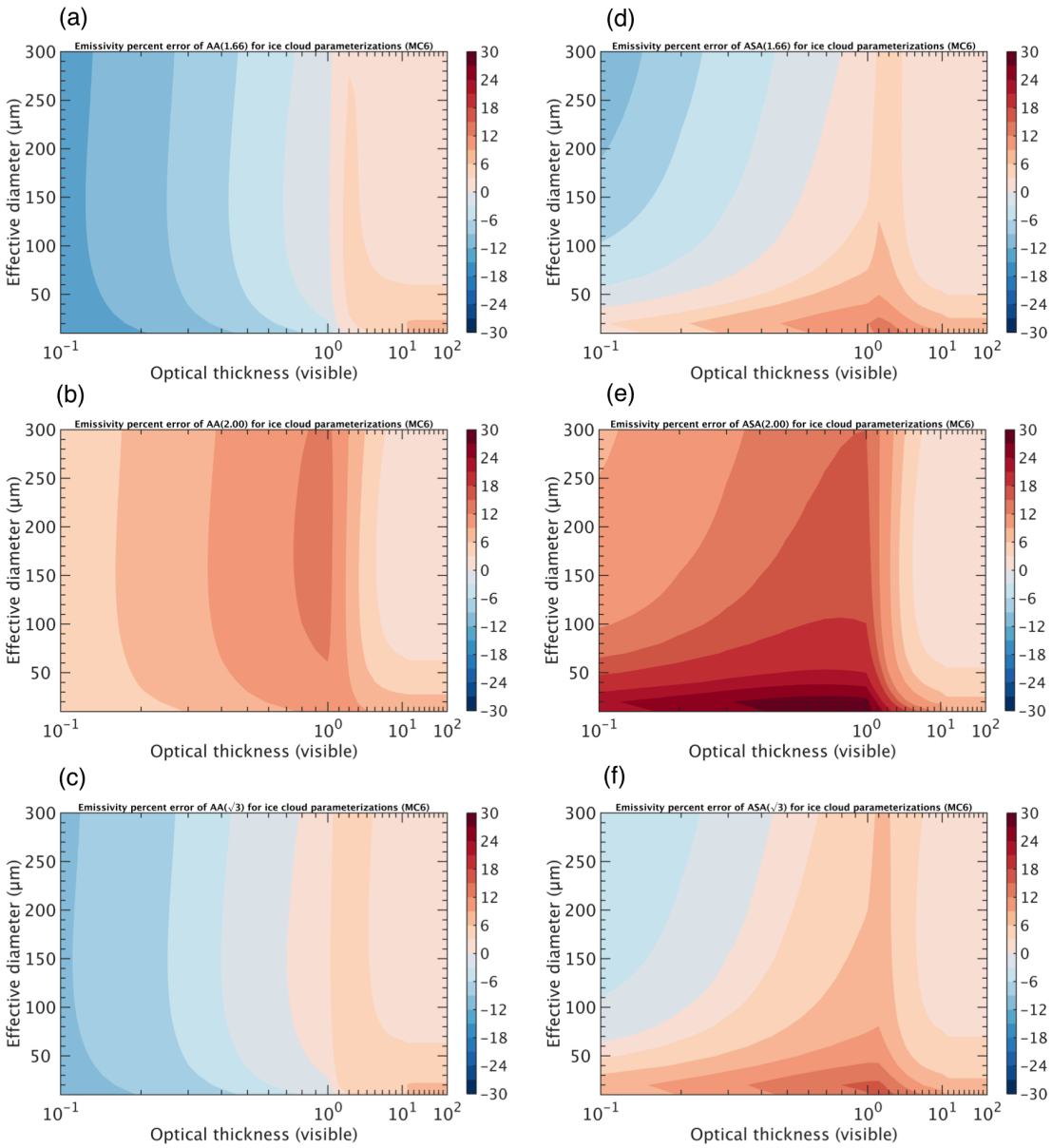

Figure 3.10 Emissivity percentage errors as a function of visible optical thickness and D_e for (a) AA(1.66), (b) AA(2.00), (c) AA($\sqrt{3}$), (d) ASA(1.66), (e) ASA(2.00), (f) ASA($\sqrt{3}$). Color bar indicates percentage error (approximate model minus reference model).

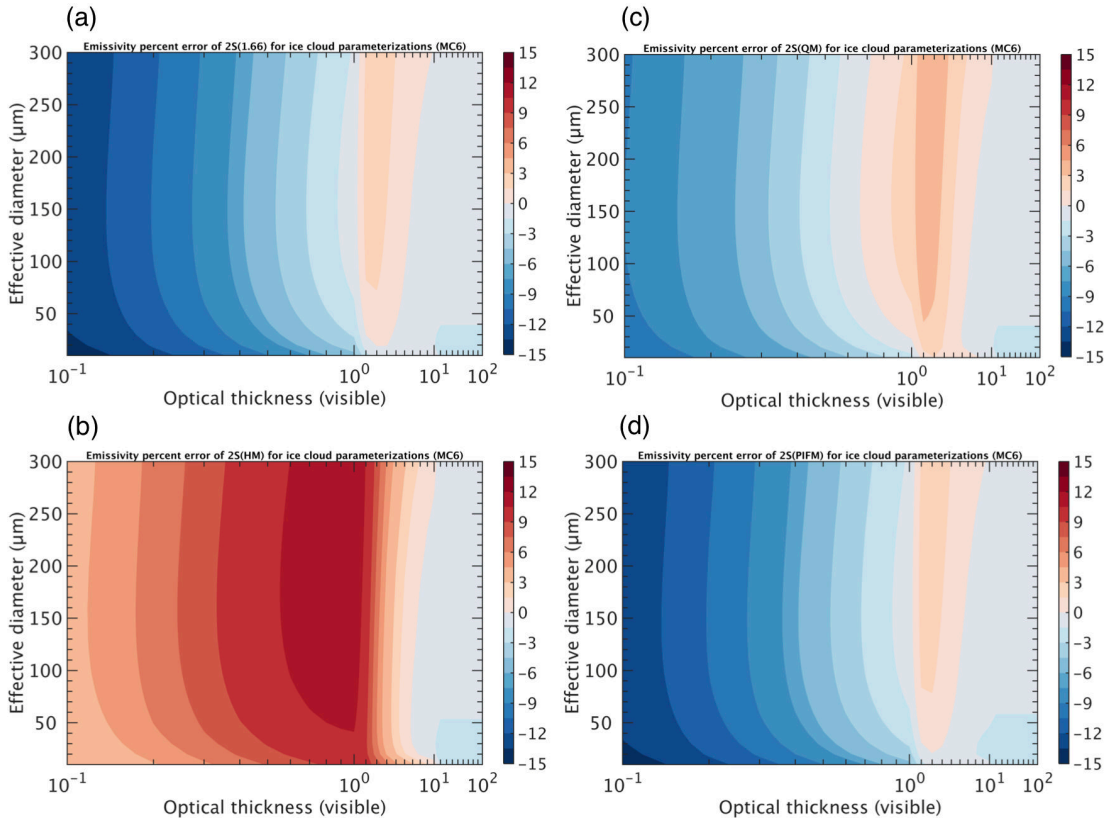

Figure 3.11 Emissivity percentage errors in a function of visible optical thickness and D_e for (a) 2S(1.66), (b) 2S(HM), (c) 2S(QM), and (d) 2S(PIFM). Errors are defined and displayed as in Figure 3.10.

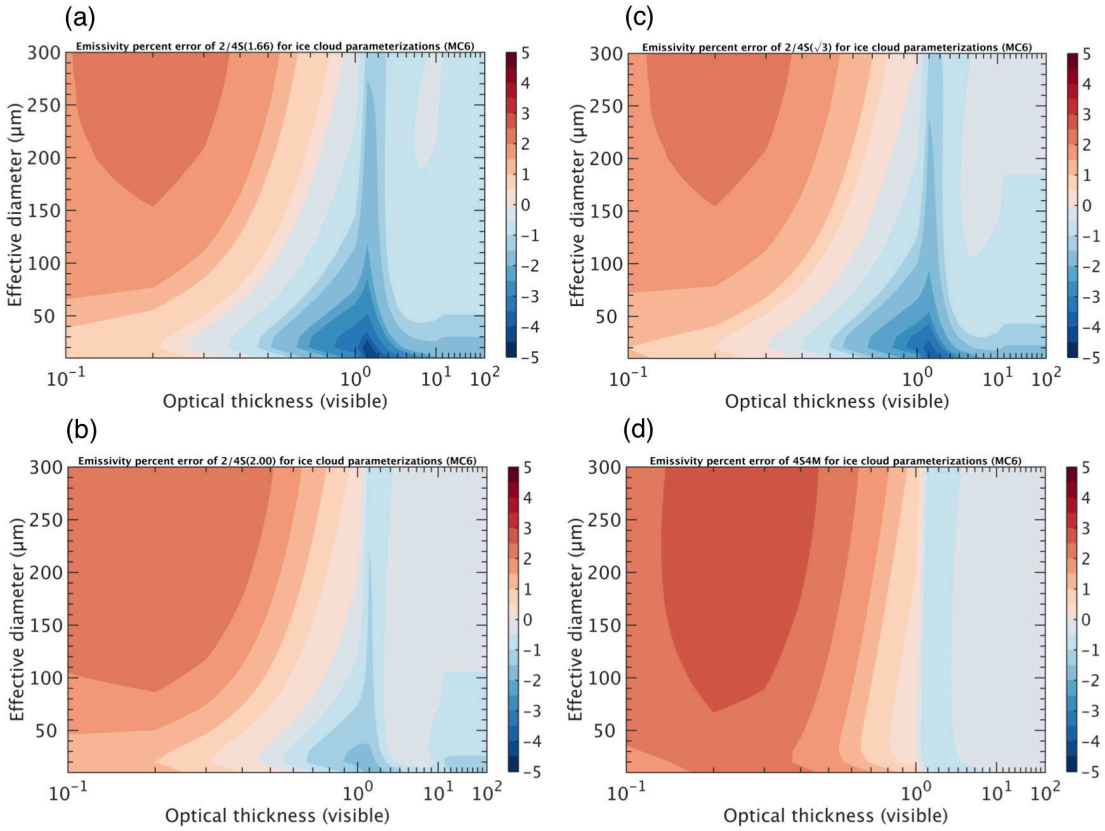

Figure 3.12 Emissivity percentage errors in a function of visible optical thickness and D_e for (a) 2/4S(1.66), (b) 2/4S(2.00), (c) 2/4S($\sqrt{3}$), and (d) 4S4M. Errors are defined and displayed as in Figure 3.10.

For evaluating the computation efficiency, we calculated the mean computational time from 1,000 runs of each of the AA, ASA, 2S, and 2/4S models and 100 runs of the *n*S*n*M models. Figure 3.13 shows the average computational time, normalized to the computational time of the 2/4S model. Since the execution time of the ASA model is about the same with the AA model, we only present comparisons for the AA model in Figure 3.13. Not surprisingly, higher angular resolution in the radiative transfer

calculations requires a longer computing time, so the 128S128M model takes about 5 orders of magnitude longer time than 2S model and about 3 orders longer time than 4S4M model. Compared to the 2/4S model run average, AA, 2S, or 4S4M models take about 0.3, 0.5, or 25 times as much computing time.

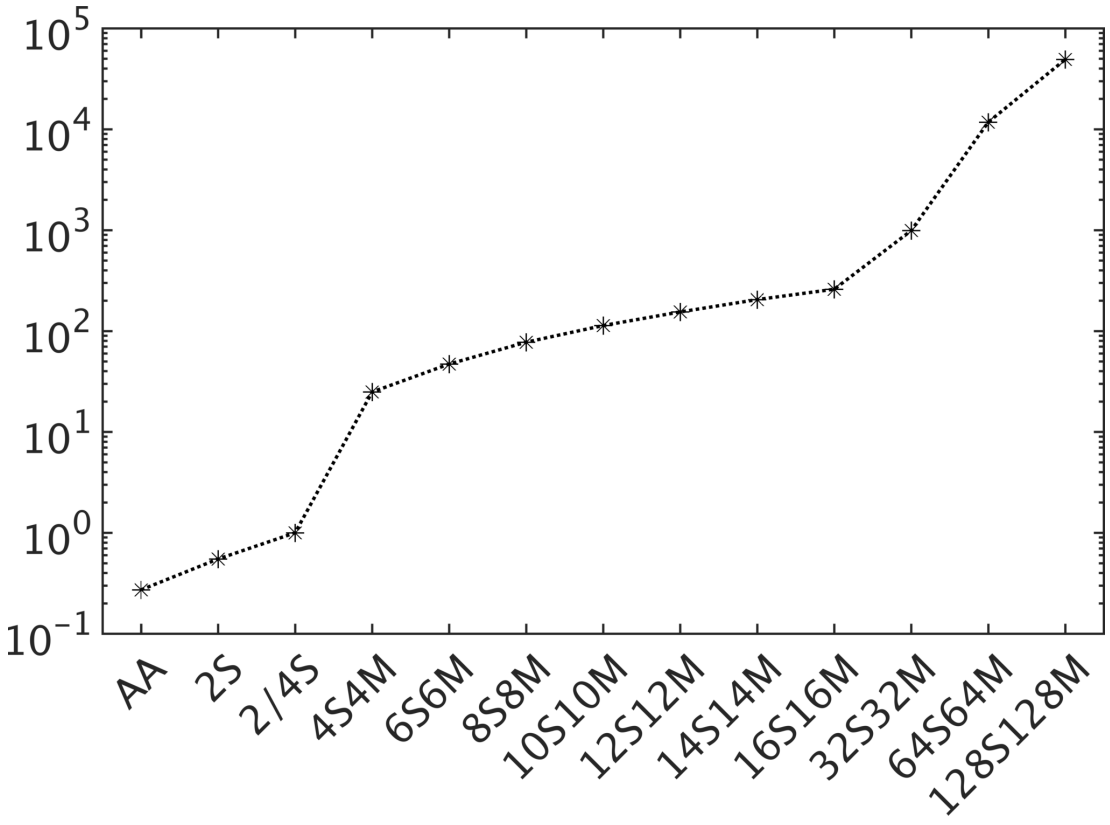

Figure 3.13 Computational efficiency for different RTM modules (normalized to 2/4S averaged computational time). The averaged computational time of ASA is the same with AA, and does not show in the Figure.

3.5 Conclusions

This study compares the computational time and average approximation errors of ice cloud emissivity obtained by various approximate RTMs (2-stream, 2-/4-strem, and DISORT with 4 to 64 streams) relative to the reference 128S128M (128-stream) DISORT calculation. All runs assume an isothermal homogeneous cloud layer with parameterizations of the MC6 ice cloud optical model, and each RTM calculates emissivity at 28 visible optical thickness and 30 effective diameter values (total 840 cases), averaged over the 16 RRTMG_LW spectral bands.

To assess the RTMs, calculation accuracy is defined as the percentage difference of the approximate method minus the reference value computed using the 128-stream (128S128M) DISORT model. Computational efficiency is estimated by measuring the average execution time for the RTM modules relative to the 2-/4-stream computation time. Although the AA, ASA, and 2S models have the most computational economy, these methods also have the largest errors (> 10%) in some cases. Increasing angular resolution in the RTM makes calculations more accurate, but computing time increases exponentially. While the 6S6M model has emissivity errors < 1%, computation takes 50 times as long as 2/4S, while the 2/4S errors are < 5%. However, even though the computational load of the 4S4M model is 25 times as much as 2/4S, the overall 4S4M simulated emissivity is no better than by using 2/4S. In general, taking accuracy and efficiency into account, 2/4S provides relatively accurate results with relatively fast computations.

References

Allan, R. P. (2011). Combining satellite data and models to estimate cloud radiative effect at the surface and in the atmosphere. *Meteorological Applications*, *18*(3), 324–333. https://doi.org/10.1002/met.285

Baran, A. J. (2009). A review of the light scattering properties of cirrus. *Journal of Quantitative Spectroscopy and Radiative Transfer*, *110*(14–16), 1239–1260. https://doi.org/10.1016/j.jqsrt.2009.02.026

Baran, A. J. (2012). From the single-scattering properties of ice crystals to climate prediction: A way forward. *Atmospheric Research*, *112*, 45–69. https://doi.org/10.1016/j.atmosres.2012.04.010

Baum, B. A., Heymsfield, A. J., Yang, P., & Bedka, S. T. (2005a). Bulk scattering properties for the remote sensing of ice clouds. Part I: Microphysical data and models. *Journal of Applied Meteorology*, *44*(12), 1885–1895. https://doi.org/10.1175/JAM2308.1

Baum, B. A., Yang, P., Heymsfield, A. J., Platnick, S., King, M. D., Hu, Y.-X., & Bedka, S. T. (2005b). Bulk scattering properties for the remote sensing of ice clouds. Part II: Narrowband models. *Journal of Applied Meteorology*, *44*(12), 1896–1911. https://doi.org/10.1175/JAM2309.1

Baum, B. A., Yang, P., Heymsfield, A. J., Schmitt, C. G., Xie, Y., Bansemer, A., … Zhang, Z. (2011). Improvements in shortwave bulk scattering and absorption models for the remote sensing of ice clouds. *Journal of Applied Meteorology and Climatology*, *50*(5), 1037–1056. https://doi.org/10.1175/2010JAMC2608.1

Baum, B. A., Yang, P., Heymsfield, A. J., Bansemer, A., Cole, B. H., Merrelli, A., … Wang, C. (2014). Ice cloud single-scattering property models with the full phase matrix at wavelengths from 0.2 to 100 μm. *Journal of Quantitative Spectroscopy and Radiative Transfer*, *146*, 123–139. https://doi.org/10.1016/j.jqsrt.2014.02.029

Bi, L., Yang, P., Kattawar, G. W., Baum, B. A., Hu, Y. X., Winker, D. M., … Lu, J. Q. (2009). Simulation of the color ratio associated with the backscattering of radiation by ice particles at the wavelengths of 0.532 and 1.064 μm. *Journal of Geophysical Research*, *114*(D4), D00H08. https://doi.org/10.1029/2009JD011759

Chandrasekhar, S. (1950). *Radiative Transfer*. Oxford: Clarendon Press.

Cheney, E. W., & Kincaid, D. R. (2007). *Numerical Mathematics and Computing* (6th ed.). Pacific Grove, CA: Brooks/Cole Publishing Co.

Chou, M.-D., Lee, K.-T., Tsay, S.-C., & Fu, Q. (1999). Parameterization for cloud longwave scattering for use in atmospheric models. *Journal of Climate*, *12*(1), 159–169. https://doi.org/10.1175/1520-0442-12.1.159

Clough, S. A., Shephard, M. W., Mlawer, E. J., Delamere, J. S., Iacono, M. J., Cady-Pereira, K., … Brown, P. D. (2005). Atmospheric radiative transfer modeling: A summary of the AER codes. *Journal of Quantitative Spectroscopy and Radiative Transfer*, *91*(2), 233–244. https://doi.org/10.1016/j.jqsrt.2004.05.058

Curry, J. A., & Herman, G. F. (1985). Infrared radiative properties of summertime Arctic stratus clouds. *Journal of Climate and Applied Meteorology*, *24*(6), 525–538. https://doi.org/10.1175/1520-0450(1985)024<0525:IRPOSA>2.0.CO;2

Ebert, E. E., & Curry, J. A. (1992). A parameterization of ice cloud optical properties for climate models. *Journal of Geophysical Research*, *97*(D4), 3831–3836. https://doi.org/10.1029/91JD02472

Edwards, J. M. (1996). Efficient calculation of infrared fluxes and cooling rates using the two-stream equations. *Journal of the Atmospheric Sciences*, *53*(13), 1921–1932. https://doi.org/10.1175/1520-0469(1996)053<1921:ECOIFA>2.0.CO;2

Edwards, J. M., & Slingo, A. (1996). Studies with a flexible new radiation code. I: Choosing a configuration for a large-scale model. *Quarterly Journal of the Royal Meteorological Society*, *122*(531), 689–719. https://doi.org/10.1002/qj.49712253107

Edwards, J. M., Havemann, S., Thelen, J.-C., & Baran, A. J. (2007). A new parametrization for the radiative properties of ice crystals: Comparison with existing schemes and impact in a GCM. *Atmospheric Research*, *83*(1), 19–35. https://doi.org/10.1016/j.atmosres.2006.03.002

Elsasser, W. M. (1942). Heat transfer by infrared radiation in the atmosphere. *Harvard Meteorological Studies*, *6*, 107.

Foot, J. S. (1988). Some observations of the optical properties of clouds. II: Cirrus. *Quarterly Journal of the Royal Meteorological Society*, *114*(479), 145–164. https://doi.org/10.1002/qj.49711447908

Fu, Q. (1996). An accurate parameterization of the solar radiative properties of cirrus clouds for climate models. *Journal of Climate*, *9*(9), 2058–2082. https://doi.org/10.1175/1520-0442(1996)009<2058:AAPOTS>2.0.CO;2

Fu, Q., Liou, K. N., Cribb, M. C., Charlock, T. P., & Grossman, A. (1997). Multiple scattering parameterization in thermal infrared radiative transfer. *Journal of the*

Atmospheric Sciences, *54*(24), 2799–2812. https://doi.org/10.1175/1520-0469(1997)054<2799:MSPITI>2.0.CO;2

Fu, Q., Yang, P., & Sun, W. B. (1998). An accurate parameterization of the infrared radiative properties of cirrus clouds for climate models. *Journal of Climate*, *11*(9), 2223–2237. https://doi.org/10.1175/1520-0442(1998)011<2223:AAPOTI>2.0.CO;2

Goody, R. M., & Yung, Y. L. (1989). *Atmospheric Radiation: Theoretical Basis* (2nd ed.). New York: Oxford University Press.

Henyey, L. C., & Greenstein, J. L. (1941). Diffuse radiation in the Galaxy. *The Astrophysical Journal*, *93*, 70–83. https://doi.org/10.1086/144246

Heymsfield, A. J., Schmitt, C., Bansemer, A., & Twohy, C. H. (2010). Improved representation of ice particle masses based on observations in natural clouds. *Journal of the Atmospheric Sciences*, *67*(10), 3303–3318. https://doi.org/10.1175/2010JAS3507.1

Heymsfield, A. J., Schmitt, C., & Bansemer, A. (2013). Ice cloud particle size distributions and pressure-dependent terminal velocities from in situ observations at temperatures from 0° to −86°C. *Journal of the Atmospheric Sciences*, *70*(12), 4123–4154. https://doi.org/10.1175/JAS-D-12-0124.1

Hong, G., Yang, P., Baum, B. A., Heymsfield, A. J., & Xu, K.-M. (2009). Parameterization of shortwave and longwave radiative properties of ice clouds for use in climate models. *Journal of Climate*, *22*(23), 6287–6312. https://doi.org/10.1175/2009JCLI2844.1

Iacono, M. J., Delamere, J. S., Mlawer, E. J., Shephard, M. W., Clough, S. A., & Collins, W. D. (2008). Radiative forcing by long-lived greenhouse gases: Calculations with the AER radiative transfer models. *Journal of Geophysical Research*, *113*(13), D13103. https://doi.org/10.1029/2008JD009944

Joseph, J. H., Wiscombe, W. J., & Weinman, J. A. (1976). The delta-eddington approximation for radiative flux transfer. *Journal of the Atmospheric Sciences*, *33*(12), 2452–2459. https://doi.org/10.1175/1520-0469(1976)033<2452:TDEAFR>2.0.CO;2

Liou, K.-N. (2002). *An Introduction to Atmospheric Radiation* (2nd ed.). Amsterdam, the Netherlands: Academic Press.

Kosarev, A. L., & Mazin, I. P. (1991). An empirical model of the physical structure of upper-layer clouds. *Atmospheric Research*, *26*(3), 213–228. https://doi.org/10.1016/0169-8095(91)90055-2

Meador, W. E., & Weaver, W. R. (1980). Two-stream approximations to radiative transfer in planetary atmospheres: A unified description of existing methods and a new improvement. *Journal of the Atmospheric Sciences*, *37*(3), 630–643. https://doi.org/10.1175/1520-0469(1980)037<0630:TSATRT>2.0.CO;2

Mitchell, D. L. (1991). Evolution of snow-size spectra in cyclonic storms. Part II: Deviations from the exponential form. *Journal of the Atmospheric Sciences*, *48*(16), 1885–1899. https://doi.org/10.1175/1520-0469(1991)048<1885:EOSSSI>2.0.CO;2

O'Brien, D. M., Rikus, L. J., Dilley, A. C., & Edwards, M. (1997). Spectral analysis of infrared heating in clouds computed with two-stream radiation codes. *Journal of Quantitative Spectroscopy and Radiative Transfer*, *57*(6), 725–737. https://doi.org/10.1016/S0022-4073(97)00044-7

Platnick, S., King, M. D., Meyer, K. G., Wind, G., Amarasinghe, N., Marchant, B., … Riedi, J. (2015). MODIS cloud optical properties: User guide for the Collection 6 Level-2 MOD06/MYD06 product and associated Level-3 Datasets, Version 1.0. Retrieved from http://modis-atmos.gsfc.nasa.gov/_docs/C6MOD06OPUserGuide.pdf

Platnick, S., Meyer, K. G., King, M. D., Wind, G., Amarasinghe, N., Marchant, B., … Riedi, J. (2017). The MODIS cloud optical and microphysical products: Collection 6 updates and examples from Terra and Aqua. *IEEE Transactions on Geoscience and Remote Sensing*, *55*(1), 502–525. https://doi.org/10.1109/TGRS.2016.2610522

Potter, J. F. (1970). The delta function approximation in radiative transfer theory. *Journal of the Atmospheric Sciences*, *27*(6), 943–949. https://doi.org/10.1175/1520-0469(1970)027<0943:TDFAIR>2.0.CO;2

Stamnes, K., Tsay, S.-C., Wiscombe, W., & Jayaweera, K. (1988). Numerically stable algorithm for discrete-ordinate-method radiative transfer in multiple scattering and emitting layered media. *Applied Optics*, *27*(12), 2502–2509. https://doi.org/10.1364/AO.27.002502

Stamnes, K., Thomas, G. E., & Stamnes, J. J. (2017). *Radiative Transfer in the Atmosphere and Ocean* (2nd ed.). Cambridge: Cambridge University Press. https://doi.org/10.1017/9781316148549

Stephens, G. L. (1984). The parameterization of radiation for numerical weather prediction and climate models. *Monthly Weather Review*, *112*(4), 826–867. https://doi.org/10.1175/1520-0493(1984)112<0826:TPORFN>2.0.CO;2

Toon, O. B., McKay, C. P., Ackerman, T. P., & Santhanam, K. (1989). Rapid calculation of radiative heating rates and photodissociation rates in inhomogeneous multiple scattering atmospheres. *Journal of Geophysical Research*, *94*(D13), 16287–16301. https://doi.org/10.1029/JD094iD13p16287

Yang, P., Bi, L., Baum, B. A., Liou, K.-N., Kattawar, G. W., Mishchenko, M. I., & Cole, B. (2013). Spectrally consistent scattering, absorption, and polarization properties of atmospheric ice crystals at wavelengths from 0.2 to 100 μm. *Journal of the Atmospheric Sciences*, *70*(1), 330–347. https://doi.org/10.1175/JAS-D-12-039.1

Yang, P., Liou, K., Bi, L., Liu, C., Yi, B., & Baum, B. A. (2015). On the radiative properties of ice clouds: Light scattering, remote sensing, and radiation parameterization. *Advances in Atmospheric Sciences*, *32*(1), 32–63. https://doi.org/10.1007/s00376-014-0011-z

Yi, B., Yang, P., Baum, B. A., L'Ecuyer, T., Oreopoulos, L., Mlawer, E. J., … Liou, K.-N. (2013). Influence of ice particle surface roughening on the global cloud radiative effect. *Journal of the Atmospheric Sciences*, *70*(9), 2794–2807. https://doi.org/10.1175/JAS-D-13-020.1

Warren, S. G., & Brandt, R. E. (2008). Optical constants of ice from the ultraviolet to the microwave: A revised compilation. *Journal of Geophysical Research: Atmospheres*, *113*(14), 1–10. https://doi.org/10.1029/2007JD009744

Wendisch, M., & Yang, P. (2012). *Theory of Atmospheric Radiative Transfer : A Comprehensive Introduction*. Weinheim: Wiley-VCH.

Wiscombe, W. J. (1976). Extension of the doubling method to inhomogeneous sources. *Journal of Quantitative Spectroscopy and Radiative Transfer*, *16*(6), 477–489. https://doi.org/10.1016/0022-4073(76)90083-2

Wiscombe, W. J. (1977). The delta–M method: Rapid yet accurate radiative flux calculations for strongly asymmetric phase functions. *Journal of the Atmospheric Sciences*, *34*(9), 1408–1422. https://doi.org/10.1175/1520-0469(1977)034<1408:TDMRYA>2.0.CO;2

Zdunkowski, W. G., Panhans, W.-G., Welch, R. M., & Korb, G. J. (1982). A radiation scheme for circulation and climate models. *Contributions to Atmospheric Physics*, *55*, 215–238.

4. CONCLUSIONS AND FUTURE WORK

This dissertation investigated influence of longwave scattering by clouds. First, we used a high spatial resolution satellite dataset called CCCM to analyze the impact of neglecting longwave scattering by clouds. The evaluations characterize the impacts by cloud phases and types, and also show the variation of the radiative scattering effect in time and space domain. After quantifying the radiative effects of excluding cloud longwave scattering, accuracy and efficiency of various RTMs were assessed by using newly parameterized MC6 ice cloud optical properties. The main conclusions of these studies are summarized as follows.

4.1 Conclusions

The results from evaluating the radiative effect caused by neglecting longwave scattering show that OLR is overestimated by up to 12 W/m^2 over the ITCZ and particularly in the Pacific warm pool, since highly scattering ice clouds are prevalent in these areas. For the downward longwave flux, underestimation is at most 3.6 W/m^2 in midlatitude, polar, and mountain regions by neglecting scattering, because these areas are relatively dry and downward scattering can reach to the surface without absorbing by gases. In the zonal distributions, simulation biases shift with the ITCZ from south to north and south again throughout the year. However, downward flux biases are close to 0 in the Tropics due to gas absorption. Overall, neglecting longwave scattering in clouds causes 2.6 W/m^2 overestimation of OLR and 1.2 W/m^2 underestimation of the surface downward longwave fluxes. These are about 10% and 5% of the global LW cloud

radiative effect, respectively. Due to their optical properties, ice clouds cause larger simulation biases than water clouds, especially in the far-IR spectral bands (350 - 500 cm^{-1}). Furthermore, due to effects of cloud vertical structures, higher and thicker clouds have larger OLR biases (up to 5 W/m^2), but the surface downward flux biases are about 1.4 W/m^2, except for thin high clouds (1H). Comparing with the clear-sky radiative effect of doubling CO_2, we find that the radiative influence of neglecting longwave scattering and doubling CO_2 are similar.

In the evaluations of different RTMs, using parameterizations of MC6 ice cloud optical properties, the 2/4S approximation shows the best performance in calculating cloud emissivity for a single homogeneous isothermal layer. This method has the best balance between computational cost and accuracy. More precisely, the 2/4S approximations are more accurate than the 4S/4M with 25 times less computing time, and are about 3 times as accurate than the 2S with only doubled computing time. To get more accurate emissivity simulations, at least 6-stream is needed to make errors smaller than 1%, and computing cost is about 50 times more expensive than by using 2/4S.

4.2 Future work

Although we use the CCCM dataset to estimate the global radiatve effect of omitting longwave scattering by clouds, the measured cloud information is a snapshot at the same time of day because the A-train satellites crosses the equator at about 1:30 p.m. local time. Such evaluations do not take the contributions of dynamic processes into account. Therefore, using GCMs to investigate the potential influence of the longwave

scattering can overcome the deficit of dynamical influence in the satellite measurements by considering all times of day and night.

We did a sensitivity analysis by using the latest Community Earth System Model (CESM) version 1.2 (Hurrell et al., 2013). In the experiments, we replaced the radiative solver and ice cloud optical properties by 2/4S(1.66) and the MC6 ice cloud optical property parameterizations, respectively. The global resolution was set to 2°, and the model was configured by the F_2000_CAM5 compset, which forces the model to use prescribed sea surface temperature and sea ice fractions (climatology of 1982 - 2001; Hurrell et al., 2008). The model was run from 2000/01 to 2044/12 for two cases, one considering longwave scattering by clouds, and the other neglecting the scattering effect.

Similar to tests shown in Chapter 2, TOA upward flux is overestimated by about 0.8 W/m^2 in Figure 4.1, and surface downward flux is underestimated by about 0.4 W/m^2 in Figure 4.2, causing about 0.4 K surface temperature warming when longwave scattering by ice clouds is considered in Figure 4.3.

In this simple test, we only considered scattering properties of ice clouds. To do a more robust experiment, both scattering properties of ice and water clouds have to be included. Additionally, since downward longwave scattering may increase the sea surface temperature, which would affect cloud formations, fully coupled simulations are required to analyze the radiation-cloud interactions triggered by longwave scattering.

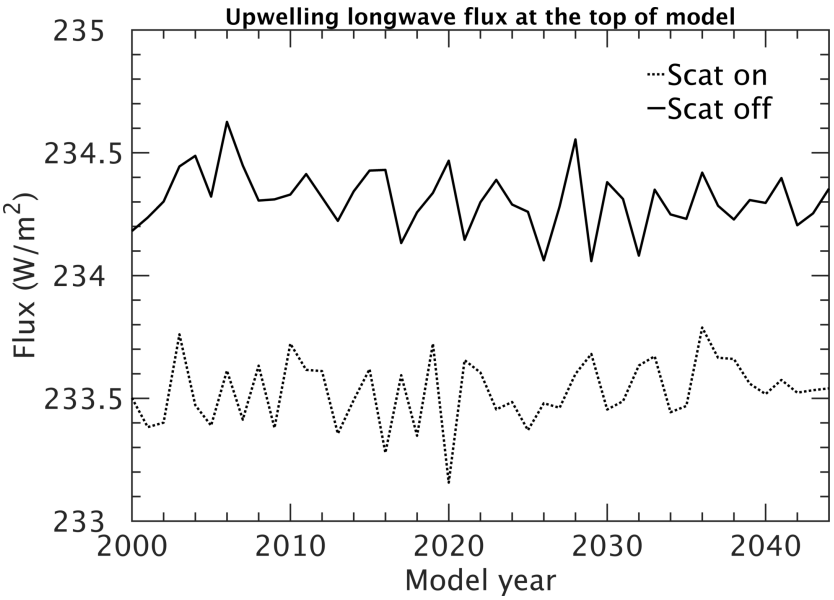

Figure 4.1 Global annual area weighted upward flux at the top of model atmosphere from 2000 to 2044. Solid line indicates neglected longwave scattering by clouds, and dashed line indicates that cloud longwave scattering is included.

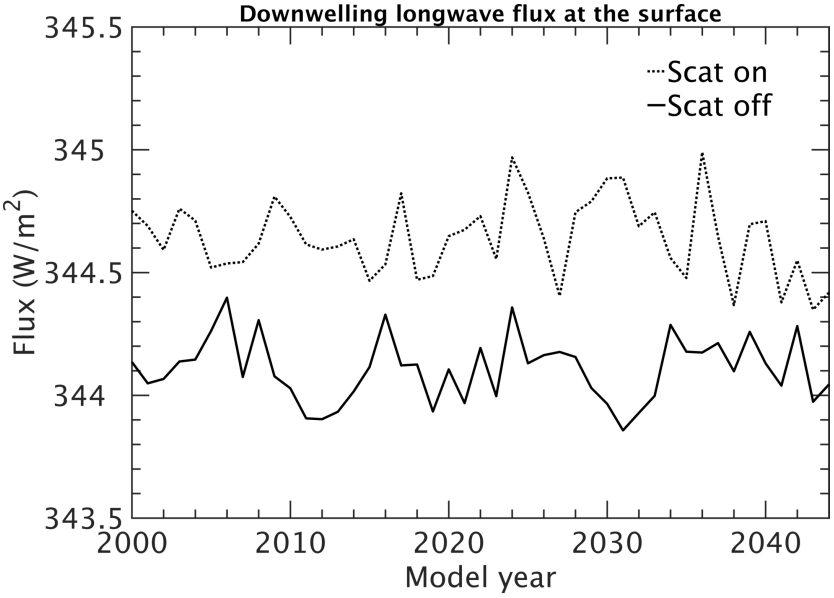

Figure 4.2 Same as Figure 4.1, but for global area weighted downward flux at the surface.

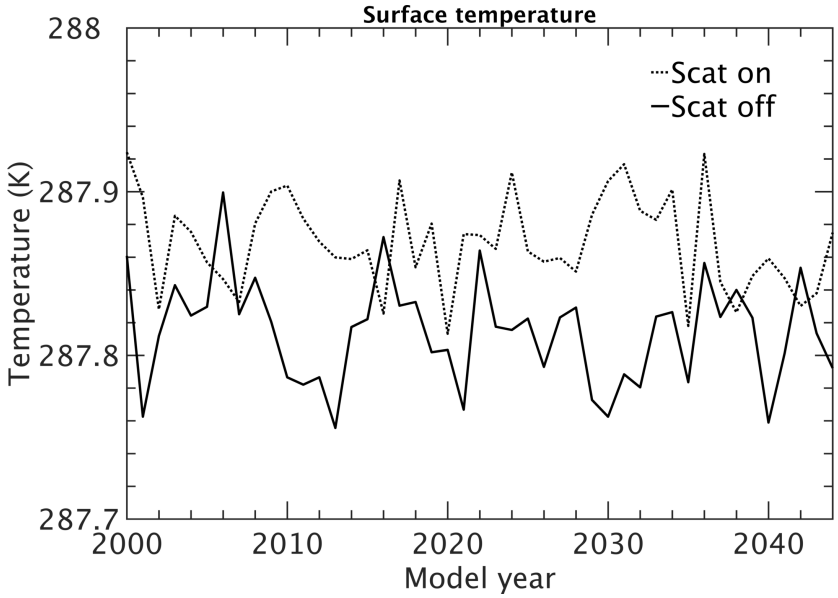

Figure 4.3 As Figure 4.1, but for global area weighted surface temperature.

References

Hurrell, J. W., Hack, J. J., Shea, D., Caron, J. M., & Rosinski, J. (2008). A new sea surface temperature and sea ice boundary dataset for the Community Atmosphere Model. *Journal of Climate*, *21*(19), 5145–5153. https://doi.org/10.1175/2008JCLI2292.1

Hurrell, J. W., Holland, M. M., Gent, P. R., Ghan, S., Kay, J. E., Kushner, P. J., … Marshall, S. (2013). The Community Earth System Model: A framework for collaborative research. *Bulletin of the American Meteorological Society*, *94*(9), 1339–1360. https://doi.org/10.1175/BAMS-D-12-00121.1